A
Dissertation Report
On

CFD based Analysis of discrete W-shaped ribs type Artificially Roughened Solar Air Heater

Submitted in Partial Fulfillment of the Requirements for the Award of Degree of
Master of Technology
In
Thermal Engineering
By
MITESH VARSHNEY
2015PTE5092

Under the supervision of

Dr. G. D. AGRAWAL
Associate Professor
Department of Mechanical Engineering
M.N.I.T. Jaipur, India

DEPARTMENT OF MECHANICAL ENGINEERING
MALAVIYA NATIONAL INSTITUTE OF TECHNOLOGY, JAIPUR
JUNE 2017

DEPARTMENT OF MECHANICAL ENGINEERING
JAIPUR (RAJASTHAN)-302017
MALAVIYA NATIONAL INSTITUTE OF TECHNOLOGY

CERTIFICATE

This is certified that the dissertation report entitled **"CFD based Analysis of discrete W-shaped ribs type Artificially Roughened Solar Air Heater"** prepared by **Mitesh Varshney** (ID-2015PTE5092), in the partial fulfillment of the award of the Degree **Master of Technology** in **Thermal Engineering** of Malaviya National Institute of Technology Jaipur is a record of bonafide research work carried out by him under my supervision and is hereby approved for submission. The contents of this dissertation work, in full or in parts, have not been submitted to any other Institute or University for the award of any degree or diploma.

Date: **Dr. G. D. Agrawal**

Associate Professor

Place: Department of Mechanical Engineering

MNIT, Jaipur, India

DECLARATION

I **Mitesh Varshney** hereby declare that the dissertation entitled **"CFD based Analysis of discrete W-shaped ribs type Artificially Roughened Solar Air Heater"** being submitted by me in partial fulfillment of the degree of **M. Tech (Thermal Engineering)** is a research work carried out by me under the supervision of **Dr. G. D. Agrawal** and the contents of this dissertation work, in full or in parts, have not been submitted to any other Institute or University for the award of any degree or diploma. I also certify that no part of this dissertation work has been copied or borrowed from anyone else. In case any type of plagiarism is found out, I will be solely and completely responsible for it.

Date:

Place:

Mitesh Varshney
M.Tech. (Thermal Engg.)
2015PTE5092

ACKNOWLEDGEMENT

I feel immense pleasure in conveying my heartiest thanks and profound gratitude to my supervisor **Dr. G. D. Agrawal** who provided me with his generous guidance, valuable help and endless encouragement by taking personal interest and attention. No words can fully convey my feelings of respect and regard for him.

I would like to express my sincere and profound gratitude to **Dr. Anuj Mathur** Assistant professor, Mechanical Engineering Department, Global Institute of Technology, Jaipur**, Mr. Sheetal Kumar Jain** and **Mr. Kamal Kumar Agrawal** (Research Scholar) Mechanical Engineering Department, Malaviya National Institute of Technology, Jaipur, who were abundantly helpful and offered invaluable assistance, support and guidance with their experience and knowledge, throughout my dissertation work. I feel greatly indebted for teaching me the concepts of ANSYS and FLUENT, without which it would have been very difficult to move ahead with my work.

I also express my deepest gratitude to my **parents** and my **brother** for their blessings and affection, without which I would not be able to endure hard time and carry on. Lastly, but not least I thank one and all who have helped me directly or indirectly in completion of the report.

(Mitesh Varshney)

ABSTRACT

Aim of the present study is to investigate the heat transfer, friction factor and fluid flow characteristics of a fully developed turbulent flow in rectangular duct of solar air heater provided with discrete W-shaped ribs- as artificial roughness on one broad wall (i.e. absorber plate). The use of artificial roughness in the form of repeated ribs on absorber surface is an effective technique to enhance the rate of heat transfer by creating turbulent flow. The commercial CFD software ANSYS FLUENT (ver. 15.0.7) is used to simulate turbulent air flow through artificially roughened solar air heater. To obtain fully developed turbulent flow at the entry of test section and uniform temperature of air at exit, extra duct length is provided at inlet and outlet sections of rectangular duct. The Reynolds averaged Navier-Stokes equations and the energy equations are solved with Realizable k–ε turbulence model (low Reynold number). The roughened wall is uniformly heated with 1000 W/m^2 constant electrical heat flux while the remaining three walls are insulated. The ranges of parameters considered are: Reynolds number from 3000 to 15000; relative roughness heights from 0.0168 to 0.0338; relative roughness pitch and angles of attack from 30˚, 45˚, 60˚ and 75° while aspect ratios and relative roughness pitch are 8 and 10 respectively. The effects of relative roughness height, angle of attack on Nusselt number and friction factor have been investigated and the results are compared with the square sectioned rib roughened duct and smooth duct under similar flow conditions to investigate the enhancement in Nusselt number and friction factor. It has been found that Nusselt number tends to increase as the relative roughness height increases for range of Reynolds number considered. Maximum enhancement in Nusselt number has been found to be 2.085 times over the smooth duct for $\alpha=60°$, $e/D_h=0.0338$, $p/e=10$ and $W/H=8$. It is also observed that friction factor tends to decrease as the flow Reynolds number increases for range of Reynolds number considered. It is also observed that at higher Reynolds number ($Re>12000$) the value of friction factor becomes almost independent of Reynolds number and its behavior becomes asymptotic for smooth as well as roughened surfaces. The effect of discretization was investigated which showed 1.31 times increment in Nusselt Number corresponding to parameters $\alpha=60°$, $e/D_h=0.0338$, $p/e=10$ and $W/H=8$ for discrete W-shaped ribs as compared to continuous W-shaped ribs, because of increase in the number of heat transfer regions. Five different types of artificial roughnesses (Chamfered type, inclined rib, inclined rib with gap position, continuous W-shaped ribs, discrete W-shaped ribs) are also compared for the standard duct and found that discrete W-shaped ribs gives the best result. Roughness and flow parameters for artificially roughened solar air heater have been optimized by considering the thermo-hydraulic performance parameter based on constant pumping power requirement. For angle of attack of 60°, relative roughness height (e/D_h) of 0.0338, relative roughness pitch (p/e) of 10 and duct aspect ratio (W/H) of 8 respectively, optimum value of thermo-hydraulic performance is obtained. Friction factor and heat transfer coefficient correlations have also been developed. It can be seen that all 40 data points lie within the deviation line ±10% and 10-90% values of Nusselt number and friction factor comes under residual -5 to 5.

Table of Content

List of Figures

List of Tables

Nomenclature

A	Actual heat transfer surface area [m^2]
A_s	Smooth plate heat transfer area [m^2]
C_p	Specific heat [J/kg K]
D	Inside diameter [m]
D_h	Channel hydraulic diameter [m]
e	Rib height [m]
e/D, e/D_h	Relative roughness height
f	Fanning friction factor
h	Heat transfer coefficient [W/m^2 K]
H	Duct depth [m]
k	Thermal conductivity of air [W/m K]
L	Test section length [m]
m	Mass flow rate [kg /s]
Nu	Nusselt number [hD_h/k]
p	Rib pitch [m]
p/e	Relative roughness pitch
Pr	Prandtl number [$\mu C_p/k$]
Q_u	Heat transfer rate [W]
Re	Reynolds number
St	Stanton number, Nu/Re.Pr

T_f	Air temperature [K]
T_{fm}	Bulk mean air temperature $(T_o + T_i)/2$ [K]
T_i	Air inlet temperature [K]
T_o	Air outlet temperature [K]
T_{pm}	Mean plate temperature [K]
w	Rib width [m]
w/e	Rib width to height ratio
W	Duct width [m]
W/H	Channel aspect ratio
X	Length in axial direction [m]

Greek symbols

α	Rib angle of attack [°]
δp	Pressure drop in the duct [Pa]
μ	Dynamic viscosity [Pa.s]
ρ	Density of air [kg/m^3]
ϕ	Chamfer angle [°]

Abbreviations

SAH	Solar Air Heater
CFD	Computational Fluid Dynamics
RNG	Renormalization Group
SST	Shear Stress Transport
RANS	Reynolds Averaged Navier-Stokes
DM	Design Modeler
PDE	Partial Differential Equations
FVM	Finite Volume Method
CAD	Computer Aided Design
DNS	Direct Numerical Simulation
LES	Large Eddy Simulation

Subscripts

i	Inlet
o	Outlet
a	Ambient
h	Hydraulic
s	Smooth
f	Air
fm	Air mean
pm	Plate mean

Chapter 1

Introduction

Solar energy has gained more importance in recent years due to the adverse environmental effects caused by greenhouse gas emissions from fossil fuel combustion and as conventional energy sources are getting rare, the cost of energy production become higher. Nowadays, renewable energy is considered as the key to a sustainable energy future. Solar energy can be used in the industrial, commercial and domestic sectors for meeting the energy demands. The simplest and the most efficient way to utilize solar energy is to convert it into thermal energy for heating applications by using solar collectors. Solar air heaters, because of their inherent simplicity are cheap and most widely used for many applications at low and moderate temperatures.

Solar energy is radiant light and heat from the Sun that is harnessed using a range of ever-evolving technologies such as solar heating, photovoltaic, solar thermal energy, solar architecture and artificial photosynthesis. The large magnitude of solar energy available makes it a highly appealing source of themal energy and then converting into electricity. The United Nations Development Program in its 2000 World Energy Assessment found that the annual potential of solar energy was **1,575–49,837** exajoules (EJ). This is several times larger than the total world energy consumption, which was **559.8 EJ** in 2012. The standard value of the solar constant (solar constant is the energy from the sun, per unit time received by a unit area of surface perpendicular to the radiation, in space at the earth’s mean distance from the sun) is 1353 W/m^2. Table 1.1 shows the amount of this radiation in the ultraviolet, visible and infrared Portions of The Spectrum.

Table 1.1 Range Of Radiation Spectrum

	Ultraviolet	**Visible**	**Infrared**
Wavelength range (μm)	0 – 0.38	0.38 – 0.78	0.78 – infinite
Fraction in range	0.07	0.4729	0.4571
Energy intensity, (W/m^2)	95	640	618

1.1 Solar Air Heating System

Solar air heating is a solar thermal technology in which the energy from the sun is captured by an absorbing medium and used to heat air. Solar air heating technologies use only free, renewable, and clean energy, and can help defray the rising cost of conventional energy. Solar air heating systems absorb thermal energy from direct sunlight to heat air; this heated air can then be circulated through buildings to provide heat.

1.1.1 Passive Solar Air Heating System

A passive solar system does not involve mechanical devices or the use of conventional energy sources beyond that needed to regulate dampers and other controls, if any. Classic examples of basic passive solar structures are greenhouses, sunrooms as the sun's rays pass through the glass windows, the interior absorbs and retains the heat. Modeling this concept in your home can cut heating costs by half compared to heating the same home by traditional means without the use of passive solar. In terms of design, success of the passive solar system depends on orientation and the thermal mass of the structure's exterior walls, which means their ability to store and redistribute heat.

1.1.2 Active Solar Air Heating System

Active solar systems use external sources of energy to power blowers, pumps and other types of equipment to collect, store and convert solar energy. Once energy from the sun is absorbed, it is stored for later use. Small systems are used to furnish electricity for heating and cooling systems in homes and other buildings, while large systems can furnish power for entire communities.

1.1.3 Advantages and Disadvantages of SAH

1.1.3.1 Advantages

I. Very efficient preheating of fresh air for buildings and drying purpose.

II. No problems from leaks, no damage, no environmental or health hazard risk from spilled heat transfer medium.

III. The need to transfer heat from working fluids to another fluid is eliminated as air is being used directly as the working substance. The system is compact and less complicated.

IV. Corrosion is a great problem in solar water heater. And this problem is not experienced in solar air heaters.

V. Leakage of air from the duct does not create any problem.

VI. Freezing of working fluid virtually does not exist.

VII. The pressure inside the collector does not become very high.

VIII. Thus air heater can be designed using cheaper as well as lesser amount of material and it is simpler to use than the solar water heaters.

1.1.3.2 Disadvantages

I. Air heaters have certain disadvantages also the first and foremost is the poor heat transfer properties of air. Special care is required to improve the heat transfer.

II. Another disadvantage is the need for handling large volume of air due to its low density.

III. Air cannot be used as a storage fluid because of its low thermal capacity.

IV. In the absence of proper design the cost of solar air heaters can be very high.

1.2 Types of Solar Air Heater

1.2.1 Non-Porous Type Solar Air Heater

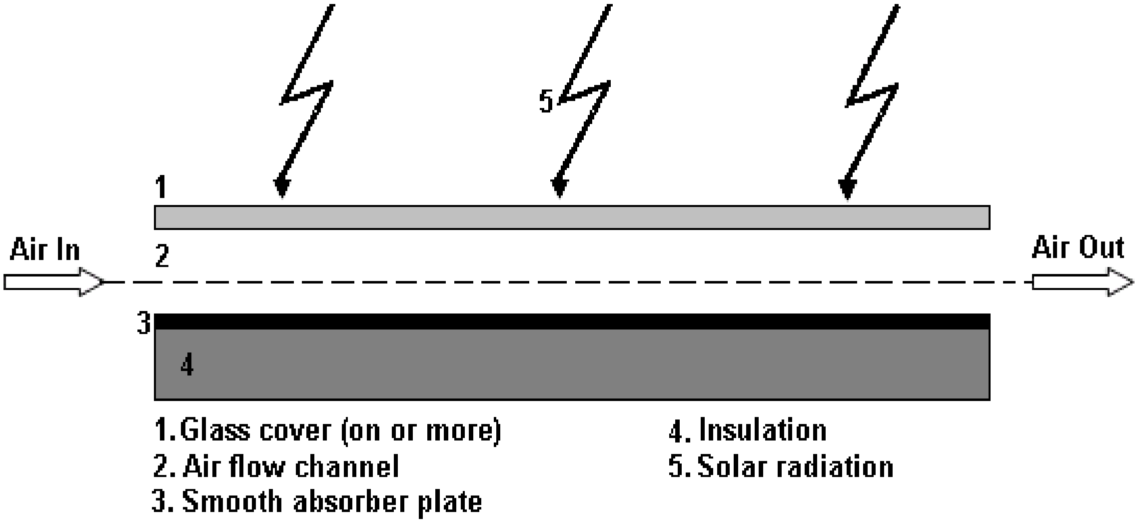

Fig.1.1 Non-Porous Type Solar Air Heater

In non-porous type, air stream does not flow through below the absorber plate but air may flow above and/or behind the plate. No separate passage is required and the air can flow between the transparent cover system and the absorber plate. In this heater as the hot air flows above the absorber, the cover receives much of the heat and in turn, loses it to the ambient. Thus a substantial amount of heat is lost to the ambient and hence this air heater is not recommended. The non-porous type with air passage below the absorber is most commonly used. A plate parallel to the absorber plate is provided in between the absorber and the insulation, thus forming a passage of high aspect ratio. In another variety of non-porous type air heater, the absorber plate is cooled by the air stream flowing on both sides of the plate. In a simple flat plate air collector, commonly known as non-porous absorbers, the air stream flow through the absorber plate without any obstruction. The non-porous types of collectors are common and simple in its design whereas porous types of collectors are complicated in its design in order to ensure a linear flow of air over and under the collector.

1.2.2 Porous Type Solar Air Heater

The second type of air heaters has porous absorber which may include slit and expanded metal, overlapped glass plat absorber and transpired honeycomb.

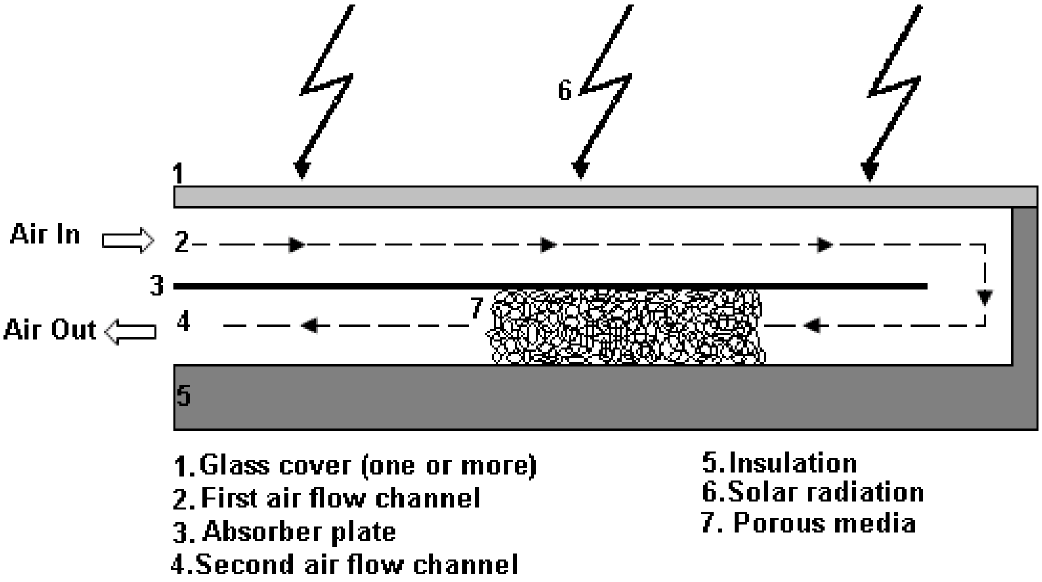

Fig.1.2 Porous Type Solar Air Heater

1.2.3. Advantages of Porous Type over Non-Porous Type

I. Solar radiation penetrates to a great depth and is absorbed along its path. Thus the radiation loss decreases. Air stream heats up as it passes through the matrix.

II. The pressure drop is usually lower than the non-porous type.

1.3 Types of Solar Collector

A solar collector is a special kind of heat exchanger that transforms solar radiation energy into heat. Several designs of the solar collectors have been developed. They can be classified broadly as concentrating collectors and flat-plate collectors.

1.3.1 Flat Plate Collector

These collectors are designed for application requiring energy at low to moderate temperatures (up to about 100° C above the atmospheric temperatures). These devices are mechanically simpler and use both direct and diffuse radiation. A flat-plate collector is installed in a fixed position facing the sun at an optimum inclination to the horizontal depending on the latitude of the location. The major applications are in water heating and air heating.

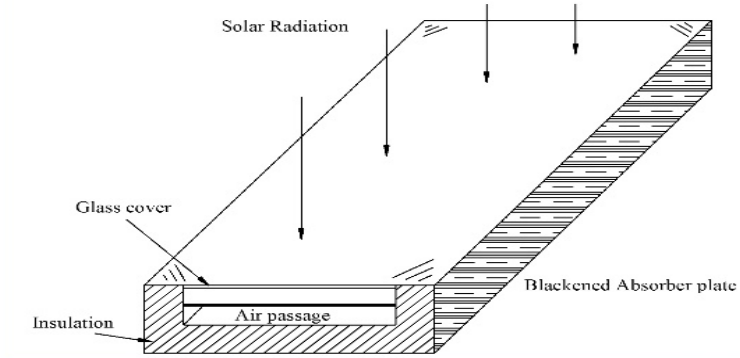

Fig 1.3 Flat Plate Collector

A typical flat-plate collector is a metal box with a glass or plastic cover (called glazing) on top and a dark-colored absorber plate on the bottom. The sides and bottom of the collector are usually insulated to minimize heat loss. In case of conventional solar air heater, the air to be heated is passed through a rectangular duct below a blackened light gauge steel or aluminium absorber plate. The absorber, whose sun facing surface is blackened, absorbs the incident solar radiation and transfers the heat to the air flowing below it.

1.3.2. Concentrating Collectors

These collectors consist of a device to concentrate the solar radiation on to a small absorbing surface and thus are capable of delivering heat energy at temperatures higher than possible with ordinary flat-plate collectors. The losses from the collector are lower due to a small area of the absorbing surface. During diffuse radiation these collectors are not so much effective; they require a tracking mechanism to follow the sun’s movement so that the radiation is directed to the absorbing surface.

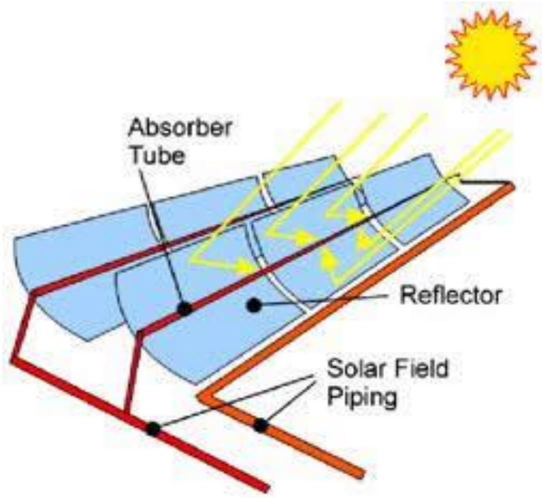

Fig 1.4 Concentrating Collectors

1.4 Recent Development in SAH

The recent development can be explained by the improvement in the collector by creating artificial roughness, use of different selective coatings, SAH with thermal storage etc.

Fig 1.5 Aluminium Beverage CAN Solar Collector

In European countries the collectors are made of waste cans for air heating, which is called DIY technology. The combination of uniform air distribution to the whole collector and a large amount of heat transfer area from the cans to the air makes for an efficient collector.

DIY solar air heating collectors are one of the better solar projects. They are easy to build, cheap to build, and offer a very quick payback on the cost of the materials to build them. They also offer a huge saving over equivalent commercially made collectors.

1.4.1 Double pass SAH

The working fluid passes over the absorber plate twice before reaching the outlet port. Various studies have been carried out on the performance analysis of double pass solar air heaters integrated with some modification.Double pass SAH has an efficiency of 1.56-5.06% higher than that of single pass solar air heater and that the double pass collector with absorber matrix is 25% higher than that collector without matrix. It is seen that the outer glass temperature was lowered by 2 -5 °C over the day and is much nearer to the atmospheric temperatures compared to those when collector is operated in a conventional single pass mode. [20]

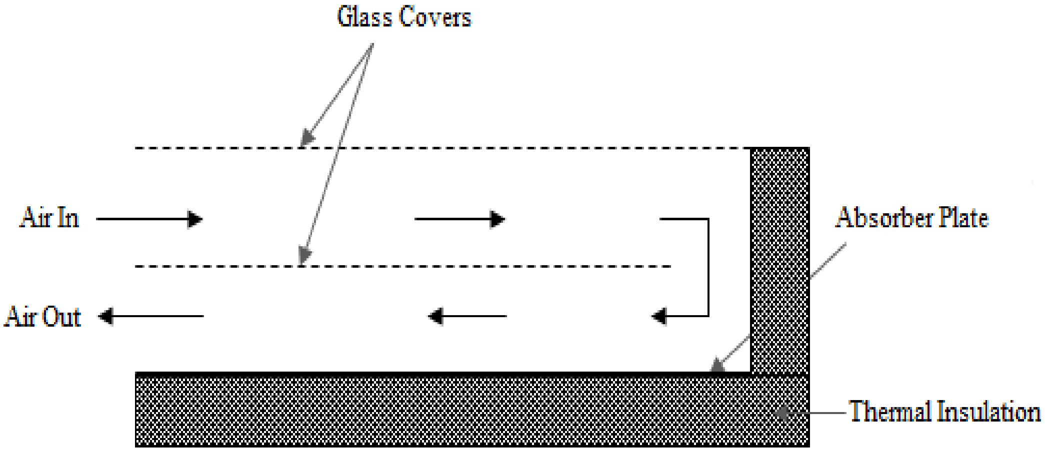

Fig 1.6 Double Pass Solar Air Heater

.

1.5 Applications of SAH

The solar air heaters find application in production plants, factories, workshops, warehouses, exhibition halls, offices, institutional facilities, theaters, gymnasiums, dryers, cleaner etc. In fact, in all places where a heating system, make-up air unit and ventilation system is present SAH can be employed. Moreover a solar heating product performs best if properly integrated within the HVAC and control system of the building for achieving optimal performance.

- **Space Heating Applications**: Solar air heating systems have been used on a wide variety of commercial, residential and industrial applications around the world. Most facilities in industries require a high make-up air volume to satisfy indoor air quality standards. The incoming air can be preheated with a solar air heating system before entering the building, which decreases the load on the traditional heaters. Many industrial facilities have successfully maintained air up to 15-20°C warmer than the surroundings.

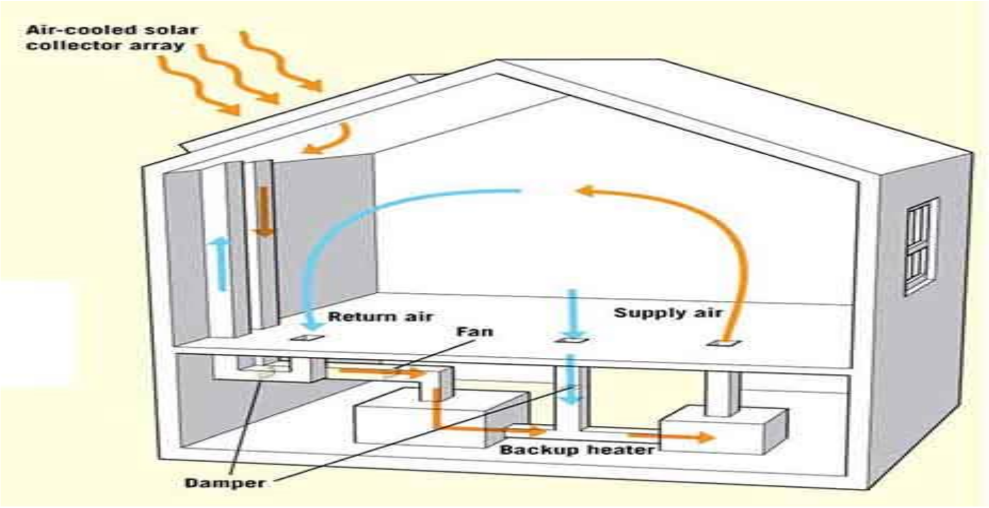

Fig. 1.7 Schematic Diagram of a Residential Space Heating System

In multi-residential buildings heating the large volume of air with conventional means is expensive, which is why many housing authorities and developers are including solar air heating systems in both new and retrofit buildings. These systems can maintain the room temperature 10-15°C above than the ambient.

- **Process Heating Applications:** Process heating applications: Solar air heat can also be used in process applications such as drying laundry, crops (i.e. tea, corn, coffee, tobacco) and other drying applications. Air heated through a solar collector and then passed over a medium to be dried can provide an efficient means by which to reduce the moisture content of the material. The agricultural and agro-food operators consume tremendous quantities of energy which represent a sizable proportion of their total input costs. Most of the world's most important crops need to be dried to remove moisture as part of the production process. The Solar air heaters can heat large volumes of incoming air up to 55°C (100°F) above ambient, making it ideally suited for many crop drying applications. An extremely high percentage of heat demand is found in food, beverages, paper and textiles, plastics and chemical industries. These industries require more than 50% of their total process heat in the temperature range up to 250°C for a variety of applications such as drying, cooking, cleaning, extraction and many others. Table 1 .2 shows typical applications and the most promising sectors of industry suitable for solar thermal systems for industrial applications [18]

Table 1.2 Temperature Range for Various Solar Heating Applications

Industrial sector	Unit Operation	Temperature range(˚C)
FOOD	Drying	30-90
	Washing	60-90
	Pasteurising	60-80
	Boiling	95-105
	Sterilizing	110-120
	Heat Treatment	40-60
Beverages	Washing	60-80
	Sterilizing	60-90
	Pasteurising	60-70
Paper industry	Cooking and Drying	60-80
	Boiler feed water	60-90
	Bleaching	130-150
Metal Surface Treatment	Treatment, electro-plating, etc.	30-80
Bricks and Blocks	Curing	60-140
	Bleaching	60-100

Textile Industry	Dyeing	70-90
	Drying	100-130
	Washing	40-80
	Fixing	160-180
	Pressing	80-100
Chemical industry	Soaps	200-260
	Synthetic Rubber	150-200
	Processing heat	120-180
	Pre-heating water	60-90
Plastic Industry	Preparation	120-140
	Distillation	140-150
	Separation	200-220
	Extension	180-200
	Drying	120-140

- **Night Cooling Applications:** The Solar air heating systems remove heat from the air to cool buildings without the use of compressors. This solar cooling technology is partly based on the scientific principle of nocturnal radiation, which can cool a roof by as much as 10°C (18°F) below ambient temperature on a clear night. As warm night air touches the cooler surface of the air heating system, it transfers its heat to the surface, which cools the air. The chilled air is then drawn in through perforations in the collector and enters the HVAC unit. Also as the largest milk producer in the world, India's dairy sector is also one of the most interesting application areas where up to 13% of process heat could be supplied by solar thermal [19].

- **Ventilation Applications:** The Solar air heating technology creates economic, ecological, and work-place advantages as diminished warming bills, CO2 uprooting, and enhanced indoor air quality. By drawing air through an appropriately composed air heater, sun powered warmed natural air can lessen the warming burden amid sunny operation.

1.6 Need of Present Study

As solar air heaters have low thermal efficiency because of low convective heat transfer coefficient between the air and absorber plate which leads higher temperature of the absorber plate and it causes maximum thermal losses to environment. It is observed that the main thermal resistance to the convective heat transfer is due to the formation of laminar sub-layer on the heat transferring surface. Efforts for enhancing heat transfer have been directed towards artificially destroying or disturbing this laminar sub-layer. Artificial roughness in the form of wires and in various arrangements has been used to create turbulence near the wall or to break the boundary layer. Thus, the artificial roughness can be employed for the enhancement of heat transfer coefficient between the absorber plate and air and thereby improve the thermal performance of solar air heater. The use of ribs/baffles increases not only the heat transfer rate but also the pressure loss. Rib/baffle geometry and arrangement in the channel also alter the flow field resulting in different convective heat transfer distribution. In particular, the angled ribs, the rib cross-section, the rib-to-channel height ratio and the rib pitch-to-height ratio are different parameters that influence both the convective heat transfer coefficient and the overall thermal performance.

1.7 Objective of present study

The objective of the present study is to improve the performance of solar air heater by breaking or destroying the laminar sub layer in the vicinity of the absorber plate. This can be done by using artificial roughness on the absorber plate, which will create turbulence and intermixing of the layers. In the present study the use of artificial roughness on absorber plate is studied for determining the heat transfer enhancement and pressure drop variation by varying different geometric and operating parameters.

The following are the objectives in the study-

- To investigate the heat transfer and friction factor characteristics of a discrete W shaped SAH duct using CFD analysis and compare its results with smooth duct under similar flow conditions.
- Validation of simulated results of discrete W-shaped duct with experimental (secondary) data.
- Performance comparison among five different artificially roughened ducts and development of their performance correlations.

1.8 Outlines of the Thesis

Chapter 1: Introduction

In this chapter background, applications, types, advantages and disadvantages of SAH has been discussed. The possible techniques to enhance the performance of SAH are also included. The objective of the study has also been stated**.**

Chapter 2: Literature Review

Various studies done in the field of SAH has been discussed. The important results from experimental, theoretical and CFD investigations were used to reach important conclusions. Different geometries used in artificially roughened SAH for the further study.

Chapter 3: CFD Analysis

It includes methodology, governing equations, the component of CFD tool and problem-solving steps in CFD analysis using ANSYS Fluent. CFD analysis procedure has also been discussed.

Chapter 4: CFD Modelling and Simulation

After the selection of SAH, modeling and meshing are done using ANSYS Fluent. Numerical solution and setup which includes boundary conditions, input parameters, numerical solver used a mentioned for better understanding. It also includes validation of CFD model and comparison of different turbulence models for artificially roughened SAH.

Chapter 5: Results and Discussion

This chapter contains performance study and the effect of roughness parameters and the effect of different types of artificial roughnesses on the performance of SAH. Based on the results obtained from the CFD analysis optimization has been done.

Chapter 6: Conclusion

The conclusions based on the study have been mentioned in this chapter. The future scope is also recommended.

Chapter 2

Literature Review

Enough literature is available on solar air heater and effect of artificial roughness on performance of SAH duct. A lot of experimental work is carried out by different researchers on heat transfer and frictional characteristics of roughened SAH duct. A review of different experimental, CFD and theoretical studies is presented in this chapter.

2.1 Experimental Work on SAH

Karwa et al. (2013) investigated thermo-hydraulic performance of rectangular ducts roughened with a new configuration of ‘V-down rib having gap’ on one wide wall was determined. Small symmetrical gap equal to rib height was created at the center of both legs of V of continuous V-down rib. The duct had aspect ratio (AR) of 12 and the Reynolds number (Re) ranged from 3000 to 15,000. For indoor testing of solar air heater, the roughened side of rectangular duct was heated with constant heat flux using electric heater while the other sides were insulated. The roughness had relative roughness height of 0.043 and relative roughness pitch of 8. Five roughened plates having flow attack angle (α) from 30° to 75° had been tested. It was found that friction factor and Nusselt number were strong function of flow attack angle and had maximum value at 60° and decrease on both sides of this angle. The highest 14hermos-hydraulic performance parameter was 2.06 which was also corresponding to $\alpha = 60°$.[1]

Saini et al. (2010) experimentally investigated the heat transfer and fluid flow characteristics of a rectangular duct roughened with multiple v-ribs. The experiment encompassed Reynolds number ranging from 2000 to 20000, relative roughness height (e/D_h) values of 0.019–0.043, relative roughness pitch (p/e) range of 6–12, angle of attack (α) range of 30–75° and relative roughness width (W/w) range of 1–10. It was found that Nusselt number and friction factor had been enhanced 6 and 5 times that of the smooth duct respectively, and maximum heat transfer enhancement had been found to occur for a relative roughness width (W/w) value of 6 while friction factor attains maximum value for relative roughness width (W/w) value of 10. It was also found that Nusselt number and friction factor attain maximum value corresponding to angle of attack (α) value of 60°.[2]

Varun et al. (2009) experimentally investigated the effective efficiency of a solar air heater duct provided with transverse and inclined ribs as artificial roughness elements on the absorber plate. The experiment encompassed Reynolds number (Re) 2000–14000, relative roughness pitch (p/e) 3–8 and a fixed value of relative roughness height (e/D_h) of 0.030. The maximum value of effective efficiency had been found for relative roughness pitch (p/e) of 8 under the range of parameters investigated.[3]

Bopche et al. (2009) experimentally investigated the heat transfer coefficient and friction factor by using artificial roughness in the form of specially prepared inverted U-shaped turbulators on the absorber surface of an air heater duct. The roughened wall was uniformly heated while the remaining three walls were insulated. These boundary conditions correspond closely to those found in solar air heaters. The experiments encompassed the Reynolds number range from 3800 to 18000; ratio of turbulator height to duct hydraulic mean diameter was varied from, $e/D_h = 0.0186$ to 0.03986 ($D_h = 37.63$ mm and e = 0.7 to 1.5 mm) and turbulator pitch to height ratio was varied from, p/e = 6.67 to 57.14 (p = 10 to 40 mm). The angle of attack of flow on turbulators, α = 90° kept constant during the whole experimentation. The heat transfer and friction factor data obtained was compared with the data obtained from smooth duct under similar geometrical and flow conditions. As compared to the smooth duct, the turbulator roughened duct enhances the heat transfer and friction factor by 2.82 and 3.72 times.[4]

Aharwal et al. (2009) experimentally investigated heat transfer and friction characteristics of solar air heater ducts with integral repeated discrete square ribs on the absorber plate. The effect of geometrical parameters, especially, the gap width and gap position had been investigated. The roughened duct had a width to height ratio (W/H) of 5.83. The relative gap position (d/W) and relative gap width (g/e) has been varied from 0.16 to 0.5 and 0.5–2.0, respectively. Experiments had been carried out for the range of Reynolds number from 3000 to 18000 with the relative roughness pitch (p/e) range of 4–10; relative roughness height (e/D) range of 0.018–0.037; and angle of attack (α) range of 30–90°. It was found that for Nusselt number, the maximum enhancement of the order of 2.83 times of the corresponding value of the smooth duct had been obtained; however, the friction factor had also been seen to increase by 3.60 times of that of the smooth duct. The maximum enhancement was observed at a relative gap position of 0.25 for relative gap width of 1.0, relative roughness pitch of 8.0, angle of attack of 60° and relative roughness height of 0.037.[5]

Saini et al. (2008) experimentally investigated the effect of roughness and operating parameters on heat transfer and friction factor in a roughened duct provided with dimple-shape roughness geometry. The investigation had covered the range of Reynolds number (Re) from 2000 to 12000, relative roughness height (e/D_h) from 0.018 to 0.037 and relative pitch (p/e) from 8 to 12. Based on the experimental data, values of Nusselt number (Nu) and friction factor (f) had been determined for different values of roughness and operating parameters. The maximum value of Nusselt number had been found corresponds to relative roughness height (e/D_h) of 0.0379 and relative pitch (p/e) of 10. While minimum value of friction factor had been found correspond to relative roughness height (e/D_h) of 0.0289 and relative pitch (p/e) of 10. [6]

Aharwal et al. (2008) had experimentally investigated heat transfer and friction factor characteristics for a rectangular duct roughened with repeated square cross-section split-rib with a gap, on one broad wall arranged at an inclination with respect to the flow direction. The duct had a width to height ratio (W/H) of 5.84, relative roughness pitch (P/e) of 10, relative roughness height (e/D_h) of 0.0377, and angle of attack (α) of 60°. The gap width (g/e) and gap position (d/W) were varied in the range of 0.5–2 and 0.1667–0.667, respectively. It was found that the maximum enhancement in Nusselt number and friction factor is 2.59 and 2.87 times that of the smooth duct, respectively, and the maximum value of thermo-hydraulic performance was found for g/e of 1.0 and d/W of 0.25.[7]

Bhagoria et al. (2005) experimentally investigated the heat transfer coefficient by using 90° broken transverse ribs on absorber plate of a solar air heater; the roughened wall being heated while the remaining three walls were insulated. The roughened wall had roughness with pitch (p), ranging from 10 to 30 mm, height of the rib of 1.5 mm, duct aspect ratio of 8 and Reynolds number between 3000–12000. It was found that the Roughened absorber plates increase the heat transfer coefficient 1.25–1.4 times as compared to smooth rectangular duct at higher Reynolds number. It was also found that Nusselt number attains maximum value for roughness pitch of 20 mm and decreases with an increase of roughness pitch and highest efficiency of 83.5% was achieved for roughness pitch 20 mm.[8]

Saini et al. (2009) experimentally investigated heat transfer and flow characteristics for the flow of air in rectangular ducts with repeated chamfered rib- roughness on one broad wall. The experiment encompassed Reynolds numbers 3000 to 20000, relative roughness heights 0.0141 to 0.0328, the relative roughness pitch 4.5, 5.8, 7.0 and 8.5, aspect ratios 4.8, 6.1, 7.8, 9.66 and 12.0, and rib chamfer angles -15°, 5°, 10°, 15° and 18°. It was found that for 15° chamfered rib had maximum heat transfer and further increment in chamfer angle did not affect heat transfer. It was also found that Friction factor and Nusselt number increases with increase in e/D_h and decreases with increase in p/e.[9]

Kumar et al. (2009) experimentally investigated heat transfer and flow characteristics for the flow of air in rectangular ducts with discrete W-shaped roughness on one broad wall. The experiment encompassed Reynolds numbers 3000 to 15000, relative roughness heights 0.0168 to 0.0338, and angle of attack 30°, 45°, 60°and 75° while the relative roughness pitch and aspect ratios remain constant. It was found that for 60° angled rib had maximum heat transfer and further increment in angle did not affect heat transfer. It was also found that Friction factor and Nusselt number increases with increase in e/D_h. [10]

2.2 CFD Based Studies on SAH

Yadav et al. (2014) investigated heat transfer and fluid flow characteristics of fully developed turbulent flow in a rectangular duct having repeated transverse square sectioned rib roughness on the absorber plate. A 2D model was made & simulated by ANSYS FLUENT (ver. 12.1). They used low Reynolds number RNG k–ε turbulence model for solving Navier-Stokes equations and the energy equation. Twelve different configurations of square sectioned rib ($p/e = 7.14 – 35.71$ and $e/D_h = 0.021 – 0.042$) had been considered. The flow Reynolds number of the duct varied in the range of 3800-18,000. The effects of p/e and e/D_h on Nusselt number and friction factor and the results were also compared with the square sectioned rib roughened duct and smooth duct under similar flow conditions to find out the enhancement in Nusselt number and friction factor. It has been found that the square sectioned transverse rib roughened duct with p/e =10.71 and e/D_h=0.042 gives the best thermo-hydraulic performance parameter for the investigated range of parameters.[11]

Kumar et al. (2014) investigated CFD based performance of a SAH duct by using thin circular wire in V-shaped, multi V-shaped ribs and multi V-shaped ribs with gap geometries as artificial roughness. Renormalization (RNG) k–ε turbulence model was used for simulation. The effect of these geometries on heat transfer and friction factor and performance enhancement was investigated and it was found that the maximum enhancement in heat transfer and friction factor was observed in the multi V-shaped ribs with gap as compare other shapes. Enhancement in heat transfer over smooth surface for v-shaped, multi V-shaped and multi V-shaped with gap ribs was 1.7, 4.7, 5.6 times respectively.[12]

Benzaoui et al. (2014) carried out CFD simulations to analyze the flow and heat transfer in the air duct of SAH provided with transverse rectangular ribs. A two-dimensional non-uniform grid was generated with local refining near the wall for critically examine the flow and heat transfer in the inter-rib region. Different turbulence models are examined and found that SST k-ω gives the best results. It was also found that the average temperature at exit decreases when speed of fluid increases.[13]

Karupaaraj et al. (2014) conducted numerical study using computational fluid dynamics (CFD) on a rectangular metal duct having transverse square wire rib roughness of small diameter created artificially on the absorber surface. The design parameters of the analysis were the flow Reynolds number, hydraulic diameter roughness pitch and height. The 3-dimensional analysis was performed using ANSYS FLUENT 12.1 code with Renormalization-group (RNG) k-ε model having the mesh model under five lakh nodes to investigate the heat transfer and fluid flow characteristics. It was found that maximum value of energy gain ratio is about 1.31 times more compared to the smooth duct for the range of operating parameters investigated.[14]

Mathur et al. (2012) worked on single pass fin type solar air heater for optimised to get better thermal performance using computational fluids dynamics (CFD) techniques (Fluent 6.3). In this optimisation work, four parameters mass flow rate, fin height, fin length, no.

of fins considered, and CFD results are validated with experimental data. CFD had given the best result on the fin length 40 cm to 50 cm and 4 to 6 cm at the no. of fins four. The improvement in the efficiency and heat gain after optimisation was 8.34% and 8.24% respectively. [15]

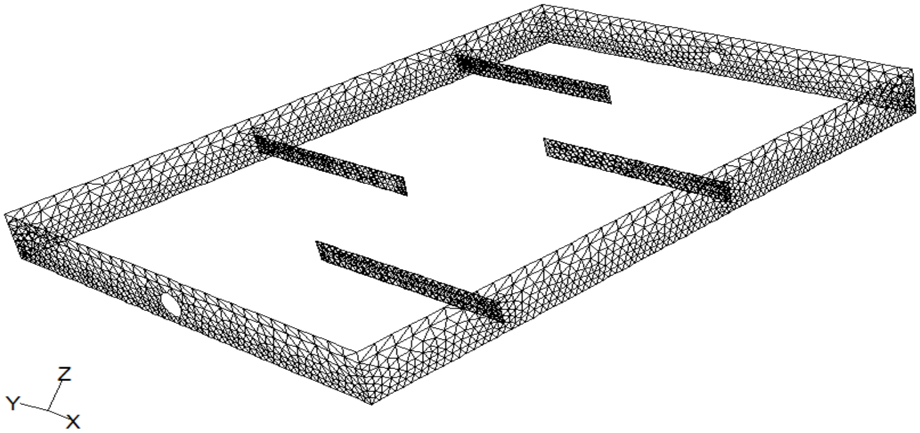

Fig. 2.1 CFD model of fins used in SAH

Chaube et al. (2006) have done a computational analysis of heat transfer and flow characteristics due to artificial roughness in the form of ribs on a broad, heated wall of a rectangular duct for turbulent flow had been carried out. Shear stress transport k-ω turbulence model was selected for simulation. The analysis shows that peak in local heat transfer coefficient occurs at the point of reattachment of the separated flow. They examined nine different shapes of rib using SST k-ω model. It was found that the turbulence intensity was maximum at peak of the local heat transfer coefficient in the inter-rib regions. The highest heat transfer was achieved with chamfered ribs but the best performance index is found with rectangular rib of size 3 x 5 mm.[16]

2.2 Other Studies

2.3.1 Study on Theoretical Analysis

Experimental studies provide the real and actual results but however it has some limitation too. It may be costlier and not possible to get results with changing all operational parameters. It may also include human error and instruments errors. So, theoretical models are developed to overcome these limitations of experimental studies.

Ong (1995) presented a mathematical model and solution procedure to calculate the thermal performance of single pass solar air heater. He considered the steady state heat transfer by using the thermal network, and set equations for a mean temperature of the walls and air was obtained by the solution of theses equations. The heat transfer coefficient is temperature depended so that firstly temperature was initially guessed. An iterative method is considered to find out the mean temperature and compared with initially guess temperature and iterative process was repeated until consecutive mean temperature value differs by less than 0.01˚C. This paper presents mathematical solution procedure involved matrix inversion of the mean temperature vector derived from the energy equations.[17]

Garg et al. (1983) used a simple mathematical model to analyze the performance of collector and power required to pumping air to maintain the flow assessed. The effective energy collected has been determined for different case studies, and the duct depth has been optimized on this effective energy. That is an optimum duct is determined for different flow rates for collecting maximum energy at minimum pumping cost. The energy balance equations were solved for different configurations using the values of ambient temperature and solar insolation for Indian condition. So that the conclusion of the study was that if a balance is to be achieved between efficiency and fluid outlet temperature on one hand and pumping power on the other, then the depth of collector should be optimized w.r.t the effective energy because this factor will give the net energy which we are gaining.[18]

Tchinda (2009) gave the review of various mathematical equations used in different type's solar air heater. It was observed that major governing equations used in solar air heater are based on the first law of thermodynamics. The purpose was this paper to review the mathematical equations used in different models of solar air heater. These equations are simply based on the steady state where the units of h_w and V are W/m^2C and m/s, respectively.

2.3.2 Use of Thermal Energy Storage Material

Saxena et al. (2013), the solar collector works as absorbing the direct solar radiation and converting it into thermal energy which can store in the form of sensible heat or latent heat or combination of both. A lot of theoretical studies have been done on thermal storage materials which are used in solar air heater. In that investigation, they found that rock bed has lower storage than to Phase Change materials. The most common materials used in thermal storage of air heater are the rock beds, pebbles beds, all composites, water and paraffin wax. Now a day's granular carbon suitable for a solar thermal application like solar air heater and solar cooker, it maintains the temperature above the ambient temperature.[19]

2.4 Learnings from Literature Review

- Turbulence in air movement provides better heat transfer than laminar sub- layer of air
- Artificial roughness, fins or baffles are necessary to break the laminar sub-layer to create air turbulence
- Fins are used to enhance the heat transfer area and create air turbulence.
- Angled fins, such as V-shaped, W-shaped, create more turbulence because of the development of secondary turbulence zone.
- Discretization further creates more turbulence because of increasing the number of heat transfer regions.
- Fins parameters (no. of fins, fins height, fins length) also affect the performance of the solar air heater.

The literature survey acknowledges that different types of roughness geometries have been used to enhance heat transfer rate in solar air heaters. In previous studies it is found that V-shaped ribs perform better than angled ribs, further discrete ribs perform better as compared to continuous ribs. The use of V-shaped ribs for the enhancement of the wall heat transfer is based on the observation of the creation of secondary heat transfer zone in the angled rib. It is found that the creation of two secondary flows cells in place straight transverse rib that shows higher overall heat transfer in the case of angled shaped ribs and further discretization increases the number of heat transfer regions. After studying these experimental investigation it is planned to investigate the heat transfer and friction characteristics of artificially roughened ducts with discrete W-shaped ribs.

Chapter 3

CFD-Based Analysis

3.1 CFD Background

Computational Fluid Dynamics (CFD) is the science of predicting fluid flow, heat transfer, mass transfer, chemical reactions and related phenomena by solving mathematical equations that represent physical laws, using a numerical process [1]. Numerous models and solution techniques have been developed over the years to help describe a wide variety of fluid motion. CFD employs the principle of resolving the entire system in small cells or grids and applying governing equations on these discrete elements to find numerical solutions regarding pressure distribution, temperature gradients, flow parameters etc. in a shorter time at a lower cost because of reduced required experimental work.

Computational Fluid Dynamics (CFD) technique solves mass, momentum, and energy conservation equations on every grid of a discretized simulation domain. The solution includes detailed information on the flow variables at the each grid. With the recent development in capabilities of computers, CFD is becoming a more convenient way to study various types of problems involving fluid flow, especially, convective heat transfer related problems as compared to the traditional experimental methods due to the flexibility of setting up complex boundary conditions, capability of analyzing transient effects of heat and fluid flow and visualization of results. In a typical CFD tool, with the help of the geometric model, a numerical model is constructed using a set of mathematical equations that describe the flow. These equations are then solved using a computer program in order to obtain the flow variables throughout the flow domain.

Since the advent of the computer, CFD has received extensive attention and has been widely used to study various aspects of fluid dynamics. The development and application of CFD have undergone considerable growth, and as a result, it has become a powerful tool in the design and analysis of engineering and other processes.

3.2 CFD Methodology

Fluid (gas and liquid) flows are governed by partial differential equations (PDE) which represent conservation laws for the mass, momentum, and energy. Computational fluid dynamics uses numerical methods to solve and analyze problems that involve fluid flows. CFD is an art of replacing such PDE systems by a set of algebraic equations which can be solved using digital computers. The governing equations are solved with respect to the specified boundary conditions using the finite volume method as implemented in the commercial CFD code FLUENT. There are three components in CFD analysis; the pre-processor, the solver, and the post-processor. Pre-processor is defined as a program that processes input data to produce output that is used as an input to the processor. In the present study, the pre-processor being used is ANSYS 15.0.7 (2014). Design Modular is used to create the geometry of the system being considered and subdivide the domain into elements which as a whole constitute the mesh or grid. The solution of the flow is later solved at the center of each of these volumes by the solver. The pre-processor also defines general surface types (for example - inlet/outlet areas) to regions of the domain. The solver discretizes the differential equations converting them to algebraic equations that can be solved numerically using the finite volume method. The finite volume method is discussed subsequently in this chapter in further detail. Finally, the post-processor is a tool that allows the interpretation of the solution in the form of graphs, plots, and charts. FLUENT 15.0 are used for both the solver and the post-processor in the present work. Microsoft Excel is also used as a post-processor for making graphs and charts to be presented in this report.

In the last thirty years the development of the Computational Fluid Dynamics (CFD) tool has made it possible to get a better understanding, analysis and solution of fluid flow and heat transfer problems in many applications. Analysis and simulation of ventilated rooms and building can also be performed quite accurately with the help of CFD. Further, increasing computational power and the theory of turbulence has enabled the researchers to create three-dimensional geometrical models using a fine grid for obtaining more accurate results.

3.3 Advantages and Limitations of CFD

CFD enjoys a number of advantages which contribute to the growing application of general-purpose CFD codes, including the following:

(i) Ability to study systems where controlled experiments are not feasible.

(ii) While the range of data that experiments can provide may sometimes be limited due to equipment or technique limitations, CFD can provide a wide range of comprehensive data as no such limitations are usually present.

(iii) The complex physical interactions which occur in a flow situation can be modeled simultaneously since no limiting assumptions are usually needed.

(iv) CFD can provide comprehensive flow visualization. In fact, in many industrial applications, CFD is more commonly applied as a flow visualization tool than a source of absolute quantitative data.

Following are the some limitations of the CFD analysis:

- **Physical phenomenon**: Even if lots of physical cases have been specified in particularly, there is still various phenomenons are waiting to create an approach. Therefore, the most convenient case has to be obtained.
- **Analytic approach (Verification):** For conducting CFD studies for a long time, one should aware of limitations to modelling turbulence. As turbulence, there are still lots of phenomenon to discover them to generate analytic approach.
- **Numerical method**: “What is your problem and how do you solve it” is one of the most important part of CFD analysis. Thus, a proper method should determine to solve the problem.
- **Computational grid (Meshing):** It is also one of the most important sections. Having a cheap or wrong generated mesh structure tends to obtain results through the solution process that leads to the farther step.
- **Hardware:** For complex projects quantum computers are required. For instance, to decrease total duration of solution process, decreasing total number of cells

through less important sections of part, through quantum computers complex projects can be solved in less duration of time.

- **Results (Validation):** Results obtained through the simulation should be validate through the proper channel. For it different types of regression analysis methods can be used.

3.4 CFD Technique for the Steady State Analysis of SAH Duct

The phenomenon of air flow through ducts, pipes, and rooms is an important issue of mass and energy transfer. Many CFD based studies have been conducted to analyze fluid flow and heat transfer in solar air heater (SAH) rectangular duct. In most of the earlier studies, a different type of roughness elements below heating plate was used to increase heat transfer to air flowing inside the duct. Nevertheless, the roughness element inside the duct plays a significant role on the heat transfer coefficient and friction factor which directly affect the thermo-hydraulic performance of SAH systems. Many researchers evaluated/predicted the heat transfer and flow along duct of SAH system by using roughness elements like (circular wire, discrete ribs, multiple V-shaped, dimple shaped, wedge shaped, arc-shaped, inclined ribs etc.) they developed the two-dimensional model.

In this chapter a three-dimensional, steady-state model has been developed by employing the Realizable k-ε turbulence model and pressure based solver has been used for analyzing the effect of rectangular chamfered ribs on heat transfer, air flow and to predict the optimum value of ribs parameter which provides batter thermo-hydraulic performance for the duct.

3.5 CFD Analysis Procedure

Fluent help file defines the step-by-step modeling procedure. A successful CFD analysis requires the following information:

(i) *A grid of points* at which to store the variables calculated by CFD.

(ii) *Boundary conditions* required for defining the conditions at the boundaries of the flow domain and which enable the boundary values of all variables to be calculated.

(iii) *Fluid properties* such as viscosity and thermal conductivity.

(iv) *Flow models* which define the various aspects of the flow, such as turbulence, mass and heat transfer, and multiphase models.

(v) *Initial conditions* used to provide an initial guess of the solution variables in a steady state simulation or the initial state of the flow for a transient simulation.

(vi) *Solver control parameters* required to control the behaviour of the numerical solution process.

The complete CFD analysis procedure can be divided into the following six stages.

3.5.1 Initial Thinking

It is very important to understand as much as possible about the problem being simulated in order to accurately define it. This stage involves collecting all the necessary data required for the simulation including geometry details, fluid properties, flow specifications, and boundary and initial conditions.

3.5.2 Geometry Creation

The geometry of the flow domain is created using a specialized drawing software. Usually, 2-D sketches are first drawn and 3-D tools are then used to generate the full geometry.

3.5.3 Mesh Generation

In this stage, the continuous space of the flow domain is divided into sufficiently small discrete cells, the distribution of which determines the positions where the flow variables are to be calculated and stored. Variable gradients are generally more accurately calculated on a fine mesh than on a coarse one. A fine mesh is, therefore, particularly important in regions where large variations in the flow variables are expected. A fine mesh, however, requires more computational power and time. The mesh size is optimized by conducting a mesh-independence test whereby, starting with a coarse mesh, the mesh size is refined until the simulation results are no longer affected by any further refinement.

3.5.4 Flow Specification

Flow specification involves defining the fluid physical properties, flow models, boundary conditions, and initial flow conditions, as determined in the initial thinking stage.

3.5.5 Calculation of the Numerical Solution

When all the information required for the simulation has been specified, the CFD software performs iterative calculations to arrive at a solution to the numerical equations representing the flow. The user needs also to provide the information that will control the numerical solution process such as the advection scheme and convergence criteria.

3.5.6 Results Analysis

Having obtained the solution, the user can then analyze the results in order to check that the solution is satisfactory and to determine the required flow data. If the results obtained are unsatisfactory, the possible source of error needs to be identified, which can be an incorrect flow specification, a poor mesh quality, or a conceptual mistake in the formulation of the problem.

3.6 Components of a Typical CFD Tool

CFD tools are structured around the numerical algorithms that can tackle fluid flow problems. In order to provide easy access to their solving power all commercial CFD packages include sophisticated user interfaces to input problem parameters and to examine the results. Hence the codes contain three main elements: (i) a pre-processor, (ii) a solver and (iii) a post-processor. The function of each of these elements within the context of a CFD code is explained in the following paragraphs.

3.6.1 Pre-Processor

Pre-processing consists of the input of a flow problem to a CFD program by means of an operator-friendly interface and the subsequent transformation of this input into a form suitable for use by the solver. The user activities at the pre-processing stage involve:

- Definition of the geometry of the region of interest: the computational domain.

- Grid generation-the sub-division of the domain into a number of smaller, non-overlapping sub-domains: a grid or mesh of cells that act as control volumes or elements.
- Selection of the physical and chemical phenomena that need to be modeled.
- Definition of thermo-physical properties of fluids involved.
- Providing specifications of appropriate boundary conditions at cells which coincide with or touch the boundaries of the domain being analyzed.

The solution to a flow problem (velocity, pressure, temperature etc.) is defined at nodes inside each cell. The accuracy of a CFD solution depends on the number, shape and size of cells in the grid, turbulence modeling, wall treatment approach, order of the discretization scheme, the level of iterative convergence, etc. In general, larger the number of cells better is the solution accuracy. Both, the accuracy of a solution and its cost in terms of necessary computer hardware and calculation time, are dependent on the fineness of the grid. Optimal meshes are often non-uniform: finer in areas where large variations occur from point to point and coarser in regions with relatively little change. A CAD system is required for geometric modeling and grid generation.

3.6.2 Solver

Numerical algorithms are used for solving the different equation of fluid flow and heat transfer. Finite volume method is most commonly used in CFD analysis. The numerical methods that form the basis of the solver perform the following major steps:

- Approximation of the unknown flow variables by means of simple functions.
- Discretization by substitution of the approximations into the governing flow equations and subsequent mathematical manipulations.
- Solution of the algebraic equations.

The numerical algorithm consists of the following steps:

- Formal integration of the governing equations of fluid flow over all the (finite) control volumes of the solution domain.
- Discretization involves the substitution of a variety of finite-difference-type approximations for the terms in the integrated equation representing flow processes such

as convection, diffusion and sources. This converts the integral equations into a system of algebraic equations.

- Solution of the algebraic equations by an iterative method.

3.6.3 Post-Processor

Post processor includes:

- Domain geometry and grid display
- Vector plots
- Line and shaded contour plots
- 2D and 3D surface plots
- Particle tracking
- View manipulation (translation, rotation, scaling etc.)
- Colour postscript output

Commercially available codes can only produce an alphanumeric output when detailed code and solution verification and validation are done. They have data export facilities for further manipulation external to the code.

3.7 Problem Solving Steps in CFD Using Design Modular and FLUENT

Having determined the important features of the problem to be solved, the following procedural steps should be followed.

- Create the model geometry and grid in the DM and mesher.
- Start the FLUENT by selecting the appropriate solver for 2D or 3D modeling.
- Import the grid from mesher to FLUENT.
- Check the grid.
- Select the solver formulation.
- Specify material properties.
- Specify the boundary conditions.
- Adjust the solution control parameters, initialize the flow field and calculate a solution by iteration.

- Examine and write the results.
- Perform grid independence test.
- Validate CFD results with experimental or any other results such as mathematical modeling results or results published by other researchers.
- If necessary, refine the grid or consider revisions to the numerical or physical model.

FLUENT uses unstructured meshes in order to reduce the amount of time required in mesh generation, to simplify the geometry modeling and mesh generation process, to allow modeling of more complex geometries that can be handled with conventional, multi-block structured meshes. FLUENT is capable of handling triangular and quadrilateral elements (or a combination of the two) in 2D, and tetrahedral, hexahedral, pyramid, wedge and polyhedral elements (or a combination of these) in 3D. Therefore, the geometry modeling and meshing can be done for any geometry using DM and mesher in ANSYS Workbench or any other CAD system.

The geometric model created in ANSYS is imported in FLUENT and grid is checked for consistency. A numerical solver (e.g. density based, pressure based, unsteady etc.) is selected based upon the type of fluid flow and heat transfer mechanism. Appropriate physical models (turbulence, combustion, multiphase etc.) are selected depending upon the type of application.

Properties of the material to be used in CFD analysis are defined and then operating and boundary conditions are specified at all boundary zones. Solution control parameters like discretization scheme, method of pressure-velocity coupling, setting up convergence criteria etc. are defined.

After initializing the flow field, the calculation for the solution is started using iteration interface provided in FLUENT. The solution which is obtained by CFD simulation must be independent of the number, size and type of the grid used in the CFD simulation; therefore, grid independence test is performed. In grid independence test, CFD simulation for the same problem is carried out using both fine and coarse size grid and then results of CFD simulations are examined for both the cases. If results show good agreement with each other, results of CFD simulations are proven to be independent of number, size and type of grid.

Results of CFD simulation should be validated with experimental results or results of mathematical modeling or previously published results of a similar problem before using the results of CFD simulation.

Chapter 4

CFD Modeling and Simulation

The CFD model was prepared in ANSYS Fluent 15.0.7 using dimensions of the SAH system experimentally investigated by researchers, Kumar et. al[10]. They designed and fabricated experimental test facility to study the effect of a discrete W-shaped rib on the heat transfer and friction characteristics of a rib-roughened rectangular duct. The cross-sectional view of the experimental set up is shown in fig. 4.1(a).

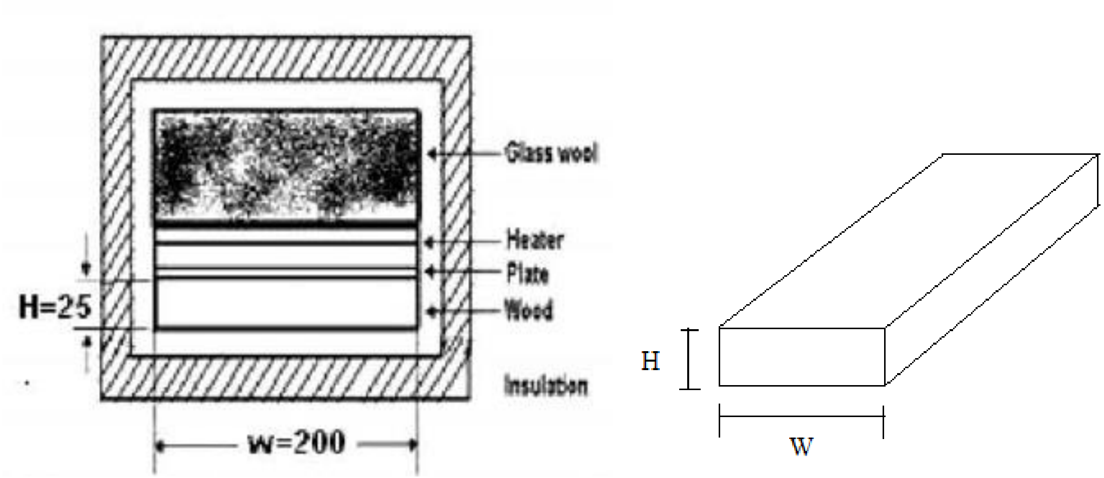

Fig. 4.1(a) Cross-Sectional View of SAH Duct

The wooden rectangular duct has an internal size of 2030 mm x 200 mm x 25 mm which consists of entrance section, test section and exit section of lengths of 177 mm, 1500 mm and 377 mm, respectively. A 6 mm thick aluminum plate, roughened artificially at the underneath side, is used as the heated wall of the test section whereas the upper walls of entry and exit sections of the duct were made of 12 mm thick plywood. The absorber plate is heated from the top by supplying a constant heat flux through an electrical heater, which was insulated by 50 mm thick glass wool and 12 mm thick plywood. A Betz micro-manometer is used to measure the pressure drop across the test section. Calibrated thermocouples have been used for monitoring the temperature variations. The airflow rate has been varied with the help of a control valve to conduct the test in the flow Reynolds number range of 3000–15,000. Fig. 4.1(b) shows the roughness geometry employed. The absorber plates were machined to develop integral ribs on the surface of an Aluminum plate.

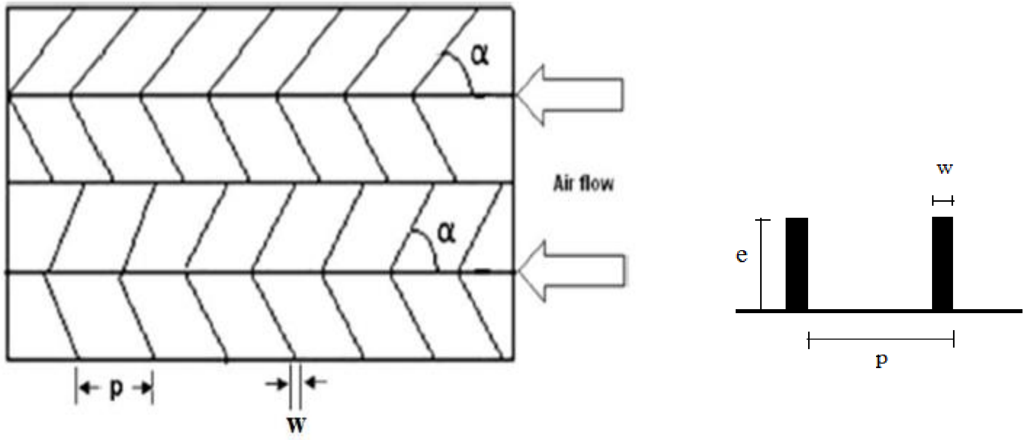

Fig. 4.1(b) Roughness Geometry of Discrete W-shaped ribs

The relative roughness height (e/D_h) is defined as the ratio of rib height to hydraulic diameter of the duct, is varied from 0.0168 to 0.0338. Different angle of attacks (α) have also been employed ranging from 30° - 75°.

4.1 Geometric Modelling

The geometric model of simple SAH system was made using ANSYS version 15.0.7. The meshing of the generated model is carried out using ANSYS ICEM CFD. The geometrical model has been created for SAH having smooth and artificial roughened duct. The complete set-up is divided into three sections. An unheated entrance duct (inlet section) of 177 mm is provided. The entrance length was chosen because at the entrance of test section the flow must be thermally fully developed. A 353 mm long exit section is also installed to reduce any downstream effect on the test section. In between these sections a test section of length 1500 mm carrying heating plate (as absorber) of aluminium at the top wall was provided. Except top wall of test section all walls were completely insulated. Fig. 4.2(a) shows that the model is symmetrical about the y-z plane. Therefore geometry of the SAH duct has been constructed by creating symmetry plane so that computational domain will be reduced, which will reduce computational effort. The first model is prepared for smooth test duct to validate the model with Dittus–Boelter empirical correlation- for Nusselt number, Nu = $0.024 \, Re^{0.8} \, Pr^{0.4}$, and Blassius empirical correlation- for Friction factor, f = $0.085 \, Re^{-0.25}$. After the validation of smooth duct CFD model boundary conditions and solver can be used for the artificially roughened SAH modeling and simulation. For artificially roughened SAH different cases were taken in each of which one parameter is varied while others are kept constant. The value of Nusselt number and friction factor is calculated for five different Reynolds number for each value of the parameter. So the total number of steady state simulations becomes forty as can be seen in Table 4.1.

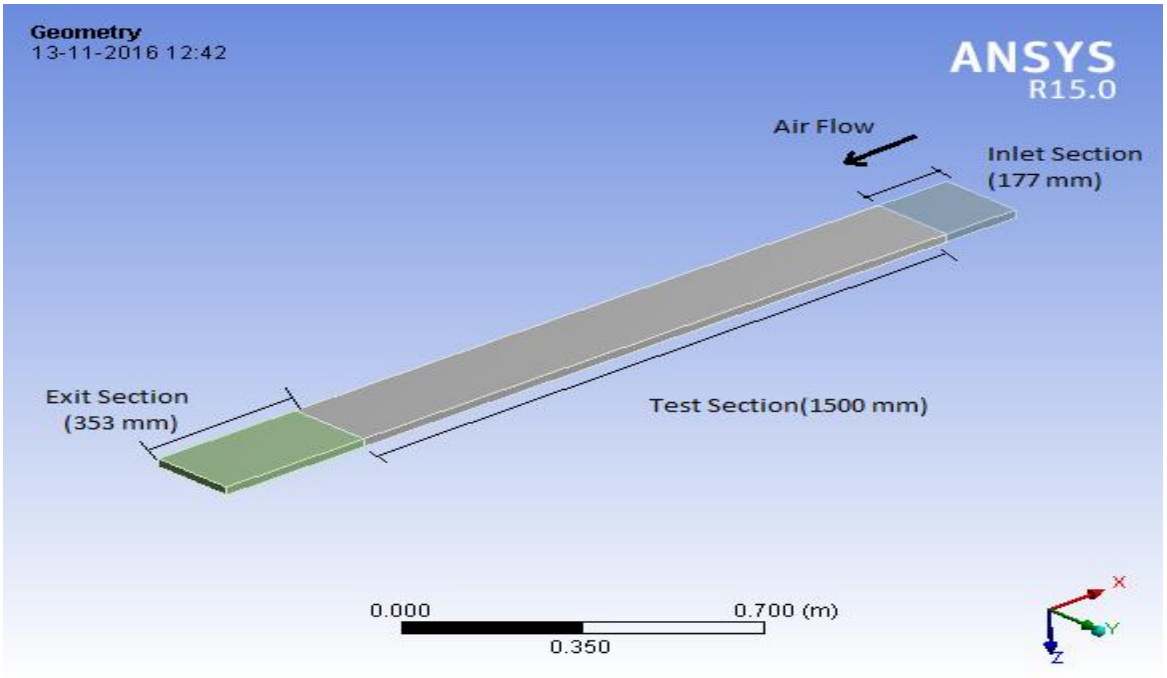

Fig. 4.2(a) Geometric Model for SAH System

Table 4.1 Variation of Parameters

S no.	Re	α(°)	e/D_h	p/e
1	3000	60	0.0168	10
2	6000	60	0.0168	10
3	9000	60	0.0168	10

4	12000	60	0.0168	10
5	15000	60	0.0168	10
6	3000	60	0.0225	10
7	6000	60	0.0225	10
8	9000	60	0.0225	10
9	12000	60	0.0225	10
10	15000	60	0.0225	10
11	3000	60	0.0258	10
12	6000	60	0.0258	10
13	9000	60	0.0258	10
14	12000	60	0.0258	10
15	15000	60	0.0258	10
16	3000	60	0.0281	10
17	6000	60	0.0281	10
18	9000	60	0.0281	10
19	12000	60	0.0281	10
20	15000	60	0.0281	10
21	3000	60	0.0338	10
22	6000	60	0.0338	10
23	9000	60	0.0338	10
24	12000	60	0.0338	10
25	15000	60	0.0338	10
26	3000	30	0.0338	10
27	6000	30	0.0338	10
28	9000	30	0.0338	10
29	12000	30	0.0338	10

30	15000	30	0.0338	10
31	3000	45	0.0338	10
32	6000	45	0.0338	10
33	9000	45	0.0338	10
34	12000	45	0.0338	10
35	15000	45	0.0338	10
36	3000	75	0.0338	10
37	6000	75	0.0338	10
38	9000	75	0.0338	10
39	12000	75	0.0338	10
40	15000	75	0.0338	10

4.2 Meshing

The partial differential equations that govern fluid flow and heat transfer are not usually amenable to analytical solutions, except for very simple cases. Therefore, in order to analyze fluid flows, flow domains are split into smaller sub-domains (made up of geometric primitives like hexahedron and tetrahedron in 3D and quadrilaterals and triangles in 2D). The governing equations are then discretized and solved inside each of these sub-domains. Typically, one of three methods is used to solve the approximate version of the system of equations: finite volumes, finite elements, or finite differences. Care must be taken to ensure proper continuity of solution across the common interfaces between two sub-domains so that the approximate solutions inside various portions can be put together to give a complete picture of fluid flow in the entire domain. The sub-domains are often called elements or cells, and the collection of all elements or cells is called a mesh or grid. In this CFD analysis, FLUENT version 15.0.7 [ANSYS] has been used and the FLUENT computation adopts a finite-volume approach to solve the conservation form of the governing flow equations.

The geometry is shown in fig. 4.2(a-c) has been generated for the analysis of smooth duct SAH. While fig. 4.3 and 4.4 shows the modeling and meshing of artificially roughened SAH with discrete W-shaped ribs. Similar procedures have been used to generate model and meshing for different cases. Air is made to flow at different velocities varying from 0.98 to 4.93 m/s in the duct.

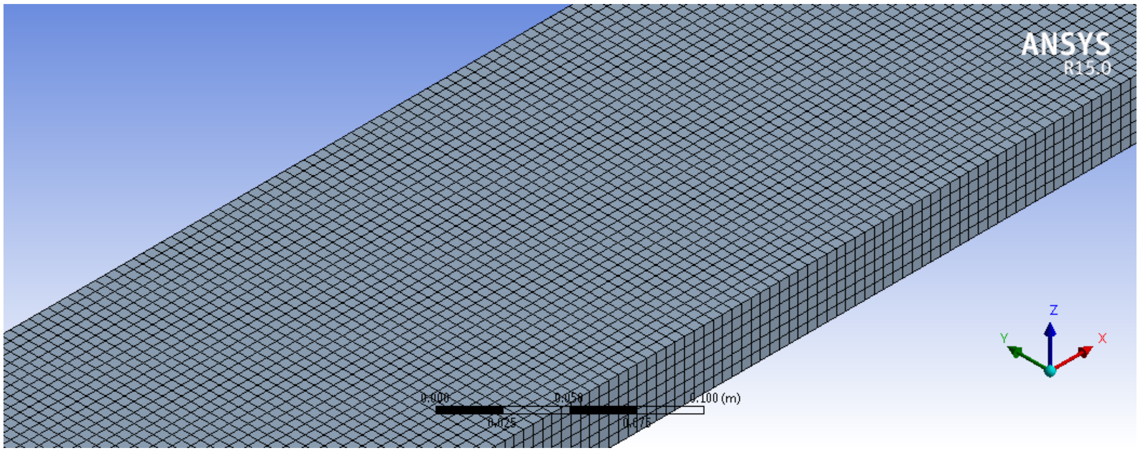

(b)Meshing (Isometric view)

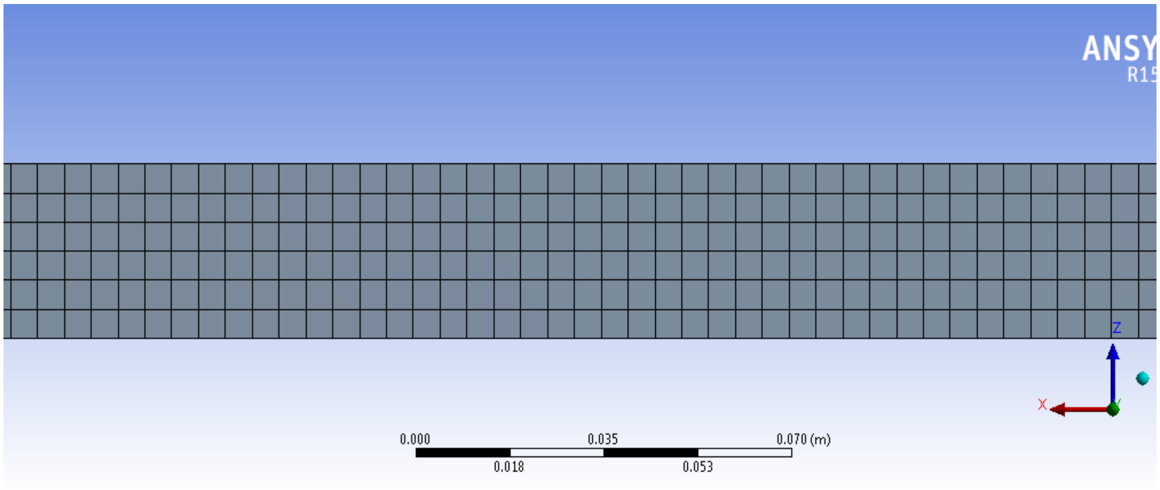

(c)Meshing (Side view)

Fig. 4.2 (b-c) Meshing of Smooth Duct SAH

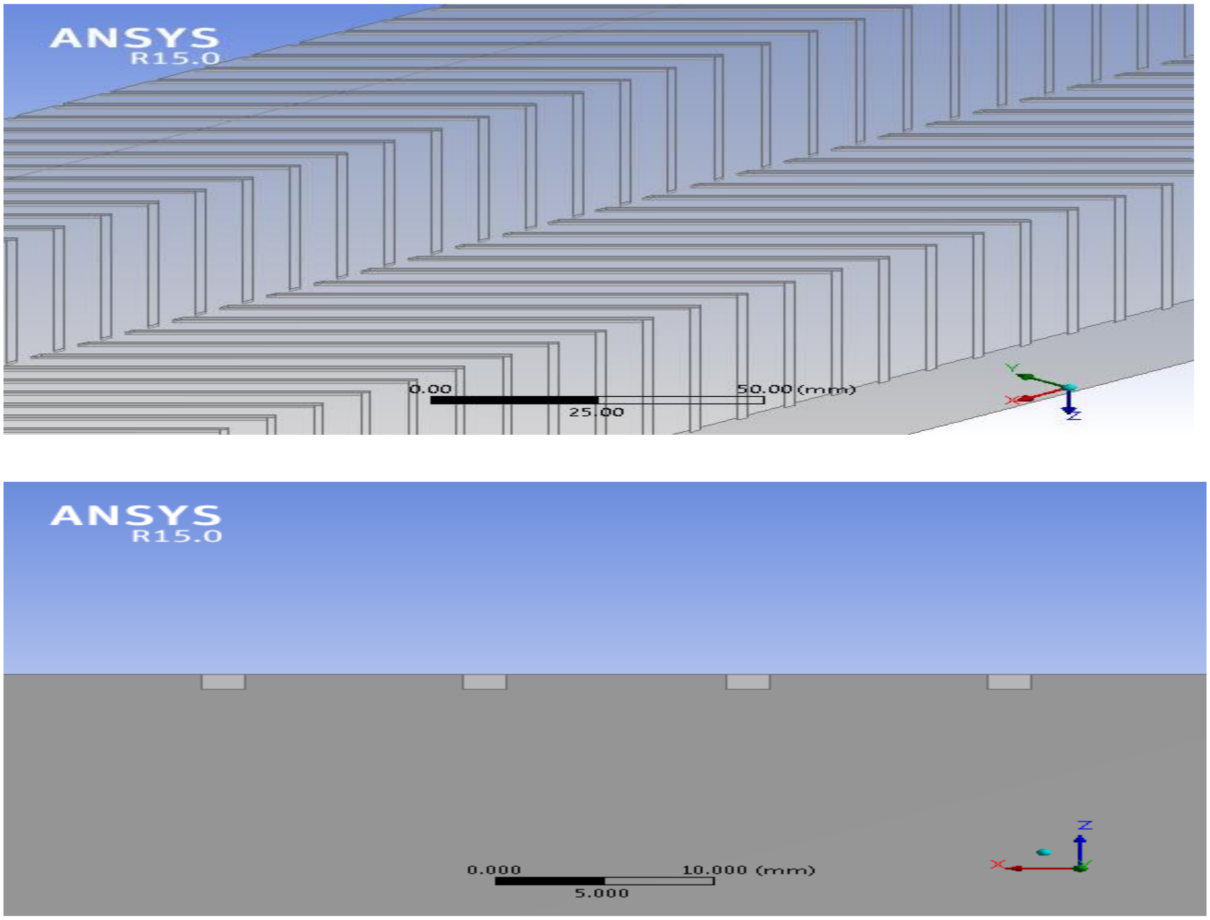

(a)Modelling of SAH with Discrete W-shaped Ribs

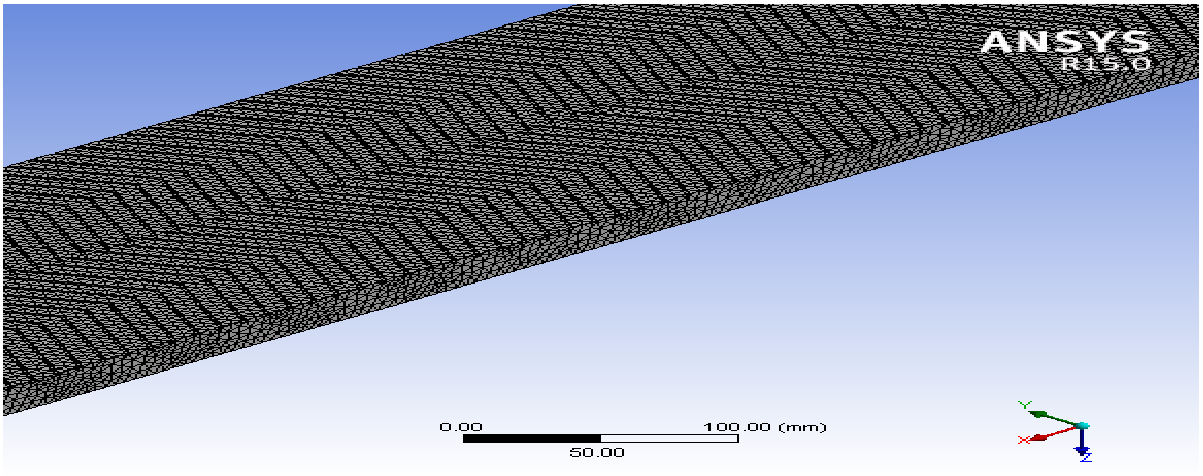

(b)Meshing of Discrete W-shaped Ribs SAH

Fig. 4.3 Modelling and Meshing of SAH with Discrete W-shaped Ribs

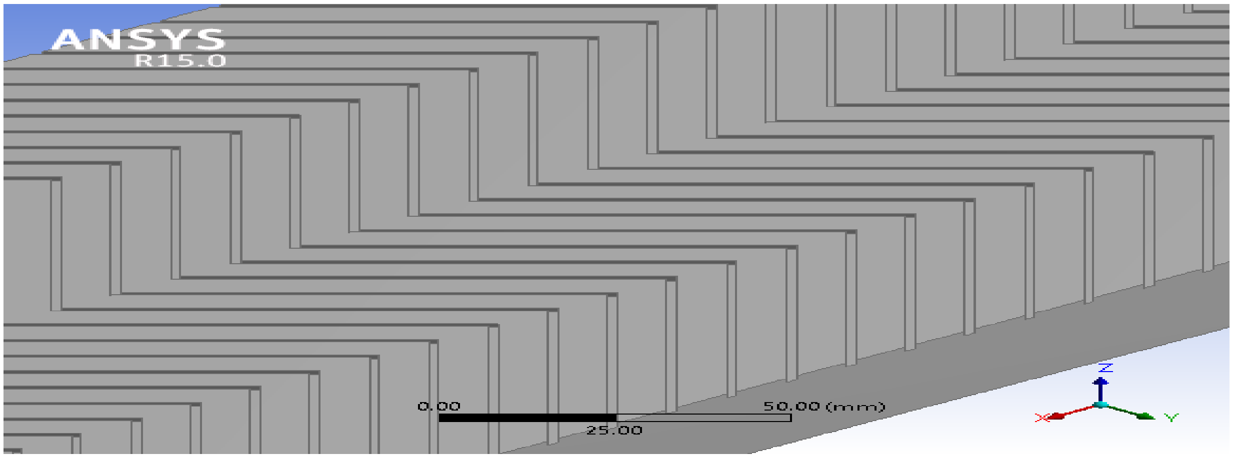

(a)Modeling of SAH with Continuous W-shaped Ribs

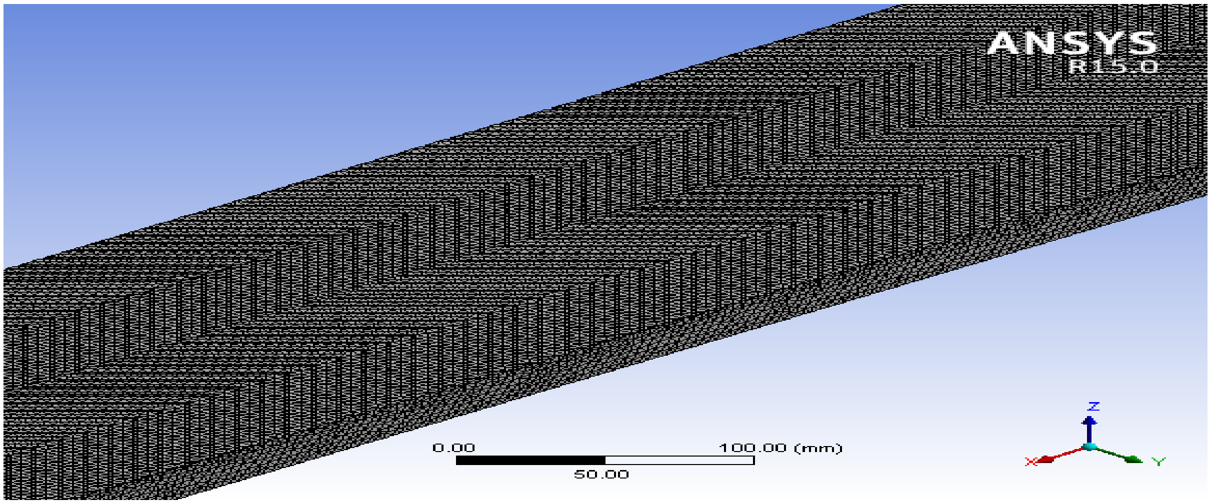

(b)Meshing of Continuous W-shaped Ribs SAH

Fig. 4.4 Modelling and Meshing of SAH with Continuous W-shaped ribs

4.3 Numerical Solution and Setup

4.3.1 Assumptions in CFD

Assumptions considered in CFD simulation are as follows:

i. Temperature of incoming air is constant at 300 K.

ii. All walls are completely insulated except heating plate which receives intensity of 1000 W/m^2.

iii. Material of the heating plate is aluminium; it is assumed that the plate is fully conductive without any plate thickness.

iv. Air flow through the test section is fully developed.

v. No slip condition for velocity is applied to the duct surface.

vi. The air properties are constant, except for the density change with temperature, which has been treated using the Boussinesq approximation.

4.3.2 Numerical Solver Used

FLUENT has two major numerical solvers; namely, segregated solver and coupled solver (implicit and explicit type). In either of these methods, FLUENT solves the governing integral equations for the conservation of mass, momentum and energy (when appropriate). Apart from these equations, other equations involving scalar quantities such as, turbulence and chemical species can also be solved in FLUENT and in all the cases a control volume based technique is used. In the present study of CFD analysis segregated solver was used. In the segregated algorithm, the individual governing equations for the solution variables (velocity, temperature, pressure, turbulent kinetic energy, etc.) are solved one after another. Each governing equation, while being solved, is "decoupled" or "segregated" from other equations. The segregated algorithm is memory-efficient, since the discretized equations need only be stored in the memory one at a time. Due to memory efficiency of the solver, it has been considered in the present case.

In this approach, the governing equations are solved sequentially (i.e., segregated from one another), because the governing equations are non-linear and coupled, therefore, several iterations of the solution loop are required to be performed before getting a converged solution.In this CFD analysis, air flows through the rectangular duct. There is heat transfer between the heating plate and the air flowing through the duct. By defining appropriate operating conditions, boundary conditions, solution parameters and convergence criteria, a converged numerical solution is obtained for each step. Different solution variables such as velocity, temperature, pressure, the turbulent kinetic energy of the flow were analyzed in each step using the sequential results of the CFD simulation.

4.3.3 Solution Technique

Solution of the equations governing scalars (e.g. temperature, pressure, species concentrations) requires a discretization scheme (Versteeg, 1995). The two schemes relevant for this work are:

- First Order Upwind, in which cell face values are set equal to the cell center value in the cell up-stream, and
- Second Order Upwind, in which the cell face values are calculated using a Taylor Series expansion to give an increased range of influence of the surrounding cells.

The Fluent User Guide (Fluent Incorporated) advises that the First Order scheme gives a stable solution with a good rate of residual convergence, with the limitation that the accuracy of the solution may not be satisfactory while the second order upwind scheme will result into more accurate solution. Therefore, second order upwind scheme has been adopted to get more accurate results.

4.3.4 Turbulence Model

Turbulence models are needed to solve unknown variables. No single turbulence model can be universally applied to all situations. Some consideration must be taken when choosing a turbulence model including; physics encompassed in the flow; level of accuracy; and computation resources available. Several turbulence transport models will be examined and discussed in this section. Both the Realizable and RNG (Renormalization Group) k-ε models along with the standard k-ε turbulence models were tested.

The largest challenge of CFD modeling lies on correct analysis of turbulent flow. Turbulence can be characterized as a chaotic state of fluid motion. It is characterized in terms of irregularity, diffusivity, large Reynolds numbers, three-dimensional vorticity fluctuations, dissipation and continuum. Because all airflows through a duct in which Reynolds number is larger than 4000 can be defined as turbulent ones, the CFD program used for airflow analysis and prediction requires appropriate models for turbulence. Generally, turbulent flows are analyzed by three approaches:

a) Direct Numerical Simulation (DNS),

b) Large Eddy Simulation (LES), and

c) Turbulence Transport Models.

The DNS method requires very fine space discretization with cell size of the order of 10^{-3}m.looking to the computation power of today's computers, simulations of such a finely meshed airflows are not realistic with this method. The LES method was developed by Deardorff (1970) who hypothesized that the turbulent motion could be separated into large and small eddies and that the separation between these two does not have a significant effect on the evolution of large eddies. Because this method assumes that small eddies are independent of the flow geometry, the need for a very fine grid is eliminated. The main contribution to turbulent transport comes from the large-eddy motion and, therefore, this method provides better results than methods which are based on empirical turbulent transport models. However, this method requires large computer power and memory. Therefore, LES is still rarely applied for the simulation of airflows. Therefore, like DNS, LES requires computers that are more powerful than those typically available today to be effectively applicable to airflow simulation.

Because of the difficulties involved in deterministic turbulence models i.e. DNS, LES, turbulence transport models are widely used in engineering applications. All the turbulence transport models solve the Reynolds statistically averaged Navier-Stokes (RANS) equations. These models can be generally divided into two categories:

- Reynolds stress models, and
- Eddy-viscosity models.

Reynolds stress models use transport equations for the individual Reynolds stress, while the eddy-viscosity models use Boussinesq approximation that relates Reynolds stress to the mean rates of deformation through an "eddy" viscosity. Reynolds stress models are applied to predict room airflow patterns in a room with jets. The results indicate that the Reynolds stress model is superior to the standard k-ε model, which is eddy viscosity model, because anisotropic effects of turbulence are taken into account. However, Chen (1996) compared three Reynolds-stress models with the standard k-ε model for natural convection, forced convection, mixed convection, and impinging jet in a room. He concluded that the Reynolds stress models are only slightly better than the k-ε model. Nevertheless, the Reynolds stress models require three to ten times more computing time than the eddy-viscosity models because of the greater algebraic complexity. Thus, with the increase of computing time and relatively small improvement in indoor airflow prediction, Reynolds stress models are still very rarely applied in building simulations.

Classic eddy-viscosity models include mixing-length models such as the zero equation, one equation, and two equations eddy-viscosity model (Rodi1993). The two equation model, often referred to as the “standard” k-ε model, is the most widely-used turbulence model in engineering practice. Here, k represents the turbulence kinetic energy, while ε represents the dissipation rate of turbulence energy. There are several variations of k-ε model. Chen (1995) tested five different k-ε models for natural convection, forced convection, mixed convection, and impinging jet in a room. Chen found that it is very difficult to identify any other model superior to the standard k-ε model. Many studies confirmed applicability of the k-ε model for thermal comfort and indoor air quality. However, there are many factors that influence the results such as mesh generation, convergence procedure, and boundary condition implementation. Therefore, a more powerful computer and a skillful user are necessary for an effective and accurate simulation.

Realizable k-ε model [Shih, 1995] was applied with the second order upwind discretization scheme in combination with the standard wall function. The Realizable k-ε model is a fairly recent addition to the group of two-equation models. It differs from the standard k-ε model in two ways. First is the turbulent viscosity is computed in a different manner using a variable for the quantity Cμ. This is motivated by the fact that in the limit of highly strained flow, some of the normal Reynolds stresses can become negative in the k-ε formulation, which is unphysical, or un-realizable. The variable form of the constant Cμ is a a function of rotation of the fluid and local strain rate, and is designed to prevent unphysical values of the normal stresses from developing. Secondly, the Realizable k-ε model uses different sink and source terms in the transport equation for eddy dissipation. The resulting equation is significantly different from the one used for standard and RNG k-ε models (RNG-based k-ε turbulence model is derived from the uses mathematical technique called "renormalization group" and is derived from navier strokes equation). The modified prediction of ε, along with the modified calculation for μt, makes this turbulence model superior to the other k-ε models for a number of applications.

In the present simulation Reynolds number varies from 3000 to 15000. The flow problem in the present case was not subjected to severe pressure gradients and non-equilibrium; therefore use of standard wall function gives accurate results.

Based upon the above fact that k-ε model is most suitable for thermal comfort and indoor air quality analyses, in this CFD analysis Realizable k-ε model has been used for analyzing the air flow inside the duct of SAH system.

Fluctuations in the velocity field mix transported quantities such as momentum and energy and cause the transported quantities to fluctuate as well. These fluctuations can be of a very small scale and therefore can create extremely large computational expenses for practical engineering calculations. A modified set of equations that require much less computational expense are used. This is done by time-averaging the instantaneous governing equations which then contain additional unknown variables.

4.3.5 4.3.5 Convergence Criteria

To reach convergence, residuals were monitored for the X, Y and Z velocity; continuity; energy; turbulent kinetic energy (k); kinetic energy dissipation rate. The convergence criterion for all the variables is 10^{-3}, except energy whose convergence criterion is 10^{-6}. The solution got converged at the maximum of 400 iterations for steady state operating conditions.

4.3.6 4.3.6 Input Parameters

- **Materials**

  All the materials were selected from a database stored within Fluent. Aluminium is used as material for absorber plate and it is assumed that plate is fully conductive without any thickness. Thermo-physical properties including density, thermal conductivity and specific heat capacity of the materials, used for CFD simulation of SAH are shown in table 4. Flow operating parameters used in the present CFD simulation are velocity and temperature of air at inlet, inlet turbulence intensity and hydraulic diameter.

Table 4.2 Physical and Thermal Properties of Materials Used in Simulation

Material	Density (kg/m^3)	Specific heat (J/kg-K)	Thermal conductivity (W/m-K)	Viscosity (kg/m-s)
Air	1.225	1006.43	0.0242	1.7894×10^{-5}
Aluminium	2719	871	202.4	-
Wood	700	2310	0.173	-

- **Boundary Conditions**

  In this section, the type of boundary condition for each of the physical boundaries of the SAH domain is explained.

a. Inlet Conditions

Velocity inlet has been specified at the inlet of SAH system. 300 K temperature of ambient air was taken as constant temperature of air at the inlet of SAH system. Inlet velocity is calculated on basis of range of Reynolds number 3000 to 15000. At the inlet of SAH uniform velocity is used and the direction is normal to the opening at inlet, velocity along the z-axis was varied from 0.98 m/s to 4.93 m/s gravity effect is also considered by providing -9.81 m/s in y-axis. Absorber plate receives intensity of radiation is 1000 W/m^2.

b. Exit Section of Duct

The outlet type “Pressure outlet” was specified on all models and turbulent intensity and hydraulic diameter are same as of inlet section.

c. Walls

Heating plate (absorber) is given uniform heat flux of 1000 W/m^2 and it is assumed that other side walls of inlet section, test section, and outlet section are completely insulated.

d. Other Walls

Walls of the entrance section, exit section and walls of test section other than absorber plate are assumed to be perfectly insulated (wood) and are given 0 W/m^2 radiation intensity.

4.3.7 Grid Independence Test

As per the practice, grid independence tests are to be conducted to assess the quality of developed CFD model. If the mesh is refined (i.e. the cells are made smaller in size hence larger in number), then the behaviour observed by the post processing should remain unchanged if the solution is grid-independent. In the present analysis, CFD simulations have been performed using a structured grid. Sizing of every edge is done independently.

Refinement of mesh is done by dividing edge in smaller parts and also by course and fine meshing method in global mesh settings. A grid-independency test was carried out to check the effect of mesh size on the accuracy of the solution.

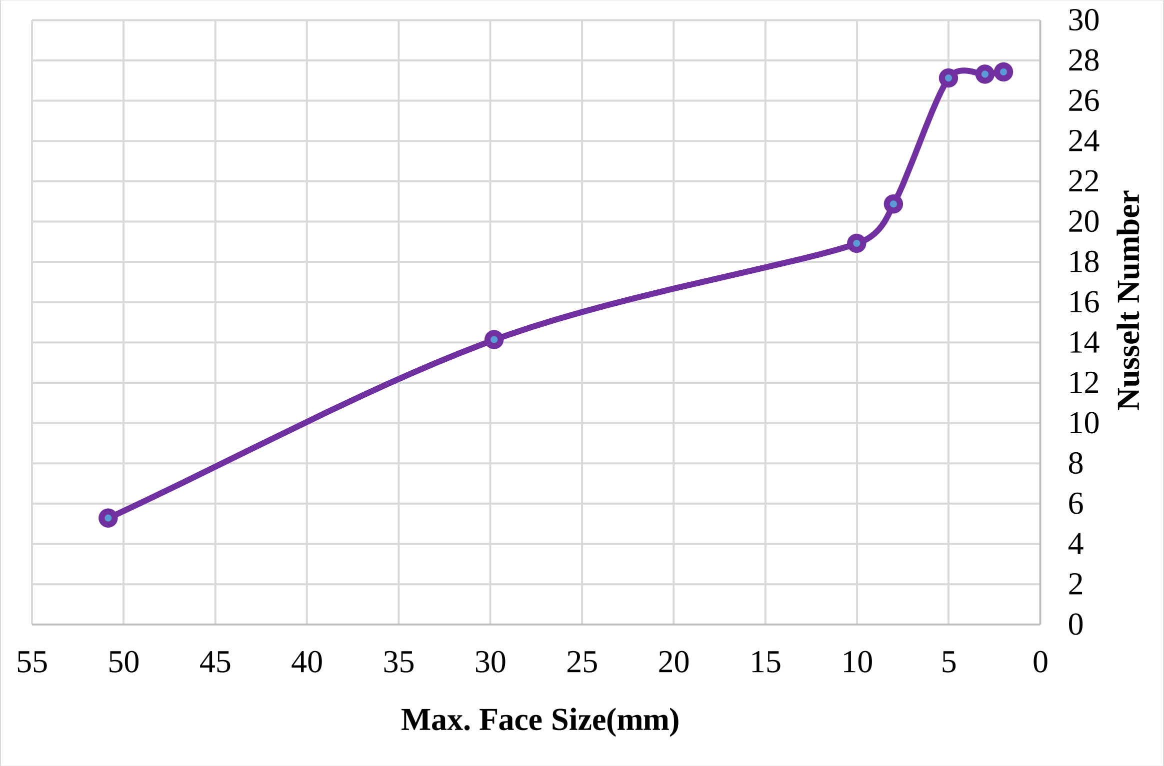

Fig. 4.5 Simulated Nusselt Number as a Result of Grid Independence Test

The independent grid size was determined by successive refinements, first grid independent test is carried out for smooth duct by increasing the number of elements by decreasing grid size. Fig. 4.5 shows the simulated value of Nusselt number for different grid size. Simulated value of Nusselt number for maximum face size 5mm, 3mm and 2mm are 27.12, 27.31 and 27.43 respectively. It is found that after 5mm grid size Nusselt number increases very less but computational time increases very swiftly so all the simulations are done for grid size 5mm. For grid size 5mm no. of nodes and no. of elements are obtained 421056 and 367160 respectively.

4.4 Validation of the Model

For selecting most appropriate turbulence model for the simulation of artificially roughened solar air heater, the Nusselt number predicted by five different turbulence models namely, Standard k–ε model, Renormalization-group k–ε model, Realizable k–ε model, Standard k-ω model and Shear stress transport k-ω model are compared with the empirical correlation available for smooth rectangular duct of a solar air heater i.e. Dittus-Boetler equation Eq. (4.1) for Nusselt number.

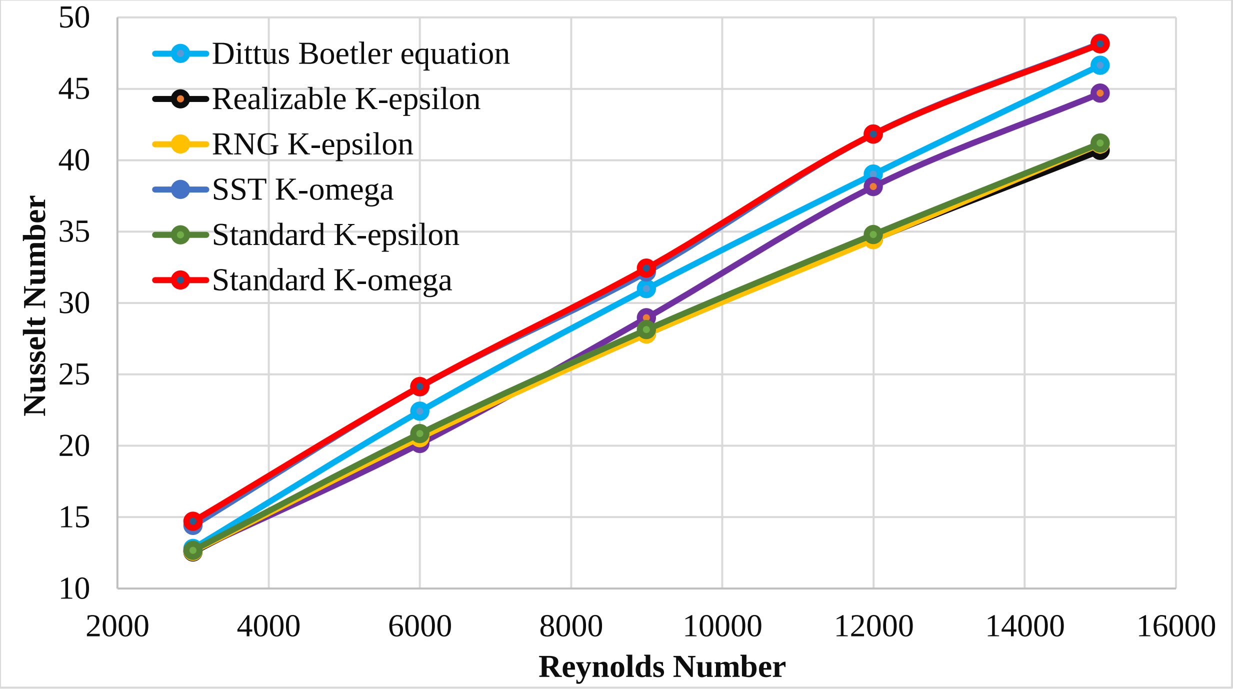

Fig. 4.6 Comparison of Different Turbulence Models with Dittus-Boelter Eqn.

Fig. 4.6 compares the variation of Nusselt number with Reynolds number using different turbulence models and results obtained from Eq. (4.1) for a smooth duct of a solar air heater. Therefore for simulation of heat transfer and fluid flow characteristics for roughened ducts, Realizable k–ε model has been chosen because its results are in closest agreement with results from empirical correlations.

$$\mathbf{Nu = 0.024\ Re^{0.8}\ Pr^{0.4}}\textbf{(Dittus Boetler Equation)} \qquad \textbf{4.1}$$

It has been observed that the results obtained by Realizable k-epsilon model are in closest agreement with Dittus-Boelter. Therefore, in the present numerical study, Realizable k-epsilon model has been employed to simulate the flow and heat transfer. Fig. 4.7 show the deviation of Nusselt number obtained for Realizable k-epsilon model and the Dittus-Boelter empirical relationship (for Nu Number) for a smooth duct.The absolute percentage deviation of the Nusselt number data by Realizable k–ε model is 5.48% from the values predicted by and Eq. 4.1.

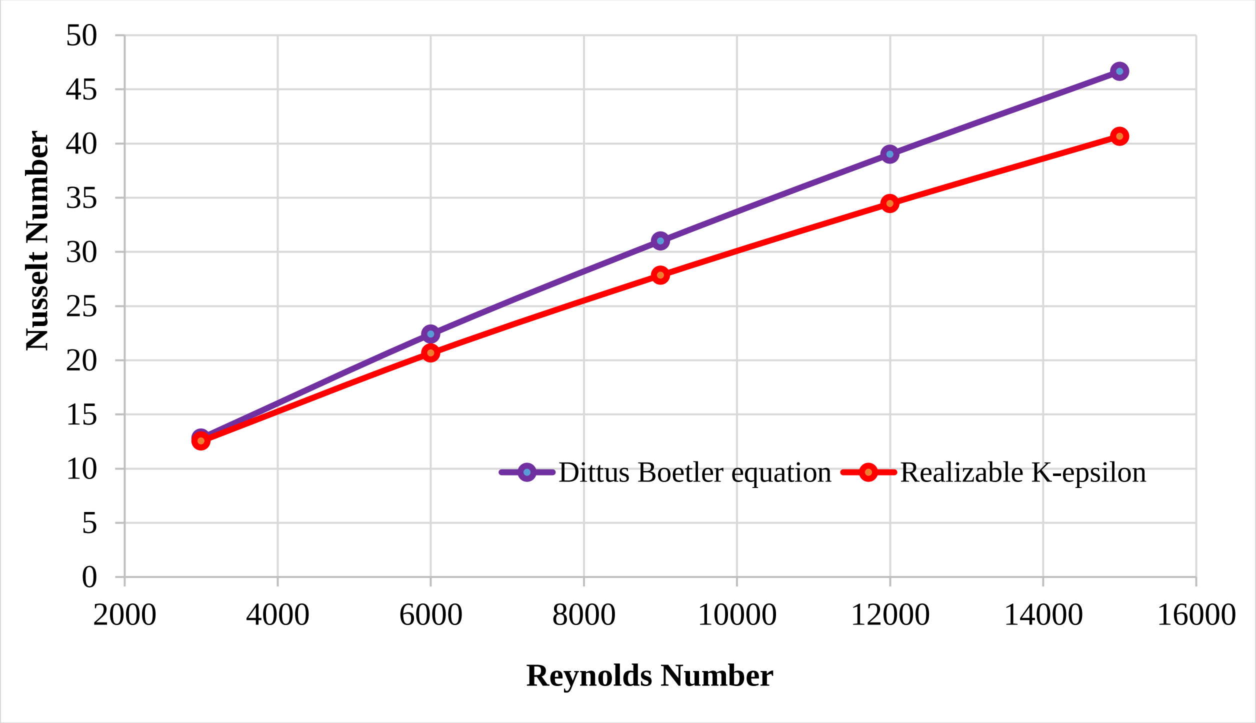

Fig. 4.7 Comparison of Realizable K-ε Nusselt Number with Dittus-Boelter Value

4.4.1 Heat Transfer Equations and Empirical Relations

As already discussed the empirical relations used are Dittus –Boelter equation and Blasius equation as given by equation 4.1 and 4.2. But the calculation of Nusselt number and friction factor uses equations of heat transfer and head loss in fluid flow. The heat transfer coefficient for the heated section is calculated from the equation 4.3.

$$\mathbf{h = Q_u / [A (T_p - T_o)]} \quad \mathbf{4.2}$$

where h (W/m2-K)is heat transfer coefficient in, Q_u is the useful heat gain in (W), A (m^2)is the area of the absorber plate, T_p is the absorber plate temperature (K) and T_o is the outlet air temperature (K).

The rate of heat gain by the air is given by equation 4.4.

$$\mathbf{Q_u = \dot{m} C_p (T_o - T_i)} \quad \mathbf{4.3}$$

where, ṁ (kg/sec.) is the mass flow rate of the air, C_p (J/kgK) is the specific heat capacity of air at constant pressure and T_i(K) is the inlet air temperature.

Heat transfer coefficient is used to determine the Nusselt number using the equation 4.5.

$$\mathbf{N_u = h D_h / k} \quad \mathbf{4.4}$$

where Nu is the Nusselt number, D_h (m) is the hydraulic diameter of the of the air duct and k (W/m-K)is the thermal conductivity of the air.

The friction factor (f) is determined from the flow velocity V (m/sec.) and the pressure drop ΔP (pascal) measured along the test section and applying Darcy–Weisbach equation as,

$$\mathbf{f = \Delta P D_h / (2 \rho L V^2)} \quad \mathbf{4.5}$$

where f is the friction factor, ρ (kg/m^3) is the density of the air and L (m) is the length of the duct.

Chapter 5

Results and discussion

The heat transfer coefficient between the absorber plate and working fluid of solar air heater is observed to be low which provides scope for the heat transfer improvement in solar air heater. The lower values of heat transfer coefficient can be ascribed to the formation of a very thin laminar sub-layer at the interface of absorber plate surface and the working fluid. The introduction of artificial roughness on the absorber surface breaks the viscous laminar sub-layer, which promotes turbulence and the heat transfer coefficient increased. Thus a significant rise in heat transfer is observed. Artificial roughness is basically a passive heat transfer enhancement technique for improving the thermo-hydraulic performance of solar air heater. The artificial roughness has been widely used for the augmentation of forced convective heat transfer, which further requires flow at the heat transferring surface to be turbulent. Although there is a considerable amount of heat transfer enhancement in solar air heater but this enhancement is, however, accompanied by a substantial increase in friction factor. This results in excessive power requirement to flow air through the duct since the energy for creating turbulence has to come from an external source like a fan or a blower. Therefore, turbulence must be created only in the vicinity of the heat transferring surface, so that the power requirement may be lessened.

5.1 Effect of Discrete W-Shaped ribs

Artificial roughness used on the absorber plate is the most efficient method for heat transfer augmentation in solar air heaters. The performance of solar air heater with artificial roughness on the airflow side of the absorber plates shows substantial enhancement in thermal efficiency as compared to solar air heaters with smooth absorber plates.

Experimental investigations appropriate to distinct roughness geometries reveal that the enhancement in heat transfer is accompanied by a significant rise in friction losses. Artificial roughness is basically a heat transfer enhancement technique by which thermo-hydraulic performance of a solar air heater can be improved. Artificial roughness, provided on the underside of the absorber plate, creates local wall turbulence. Secondary recirculation flows further enhance the convective heat transfer.

Flows from the core to the surface reduce the thickness of boundary layer and secondary flows from the surface to the core flow promote mixing. Energy for creating turbulence has to come from a blower and excessive turbulence results in greater power Therefore, it is desired that turbulence be created in the region very close to the heat transferring surface, so that the power requirement may be reduced. This can be achieved by keeping the roughness height small in comparison with the duct dimension. Although, there are other parameters also that characterize the arrangement and shape of the roughness are:

1. Relative roughness pitch (p/ e): Relative roughness pitch (p/ e) is the ratio of the distance between two consecutive ribs and height of the rib.

2. Angle of attack (α): Angle of attack is the inclination of rib with the direction of air flow in the duct.

3. Relative roughness height (e/D): Relative roughness height (e/D) is defined as the ratio of the height of the rib to equivalent hydraulic diameter of SAH duct.

4. Shape of roughness element: The roughness elements can be two-dimensional or three-dimensional discrete elements, transverse, inclined, V-shaped continuous or broken ribs with or without a gap. The roughness elements can also be arc-shaped wire or dimple or cavity or compound rib-grooved. The commonly used shape of ribs is square but other different shapes like chamfered, circular or semi-circular have also been considered to investigate thermo-hydraulic performance.

The temperature contours for smooth duct absorber plate obtained through CFD analysis is shown Fig. 5.1. While Fig. 5.2 represents fluid temperature contours for roughened duct absorber plate. It is observed that temperature of the absorber plate for the artificially roughened absorber plate would be less than that for the smooth duct absorber plate at the same mass flow rate and same duct dimensions. A maximum decrease of 8.8% was observed. This is because there is more heat transfer in case of artificially roughened duct. Due to increased useful heat transfer coefficient absorber plate temperature decreases and average temperature of the fluid increases

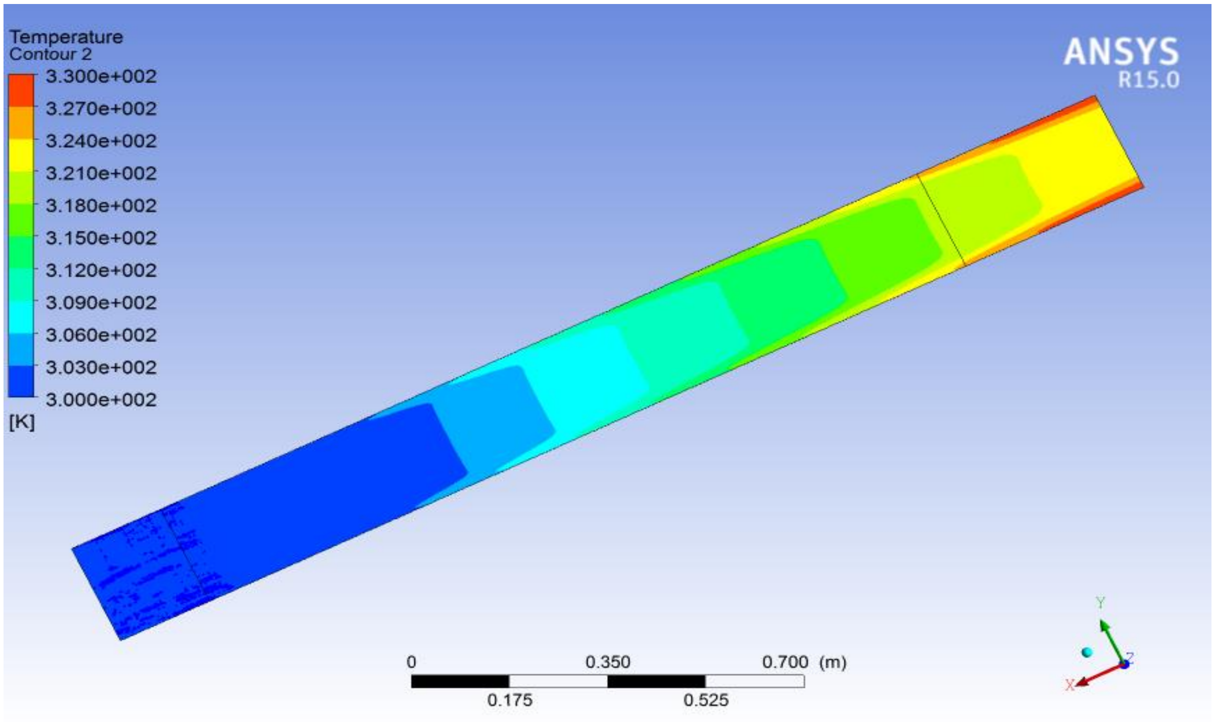

Fig. 5.1 Temperature Contours for Smooth Absorber Plate (Re=9000)

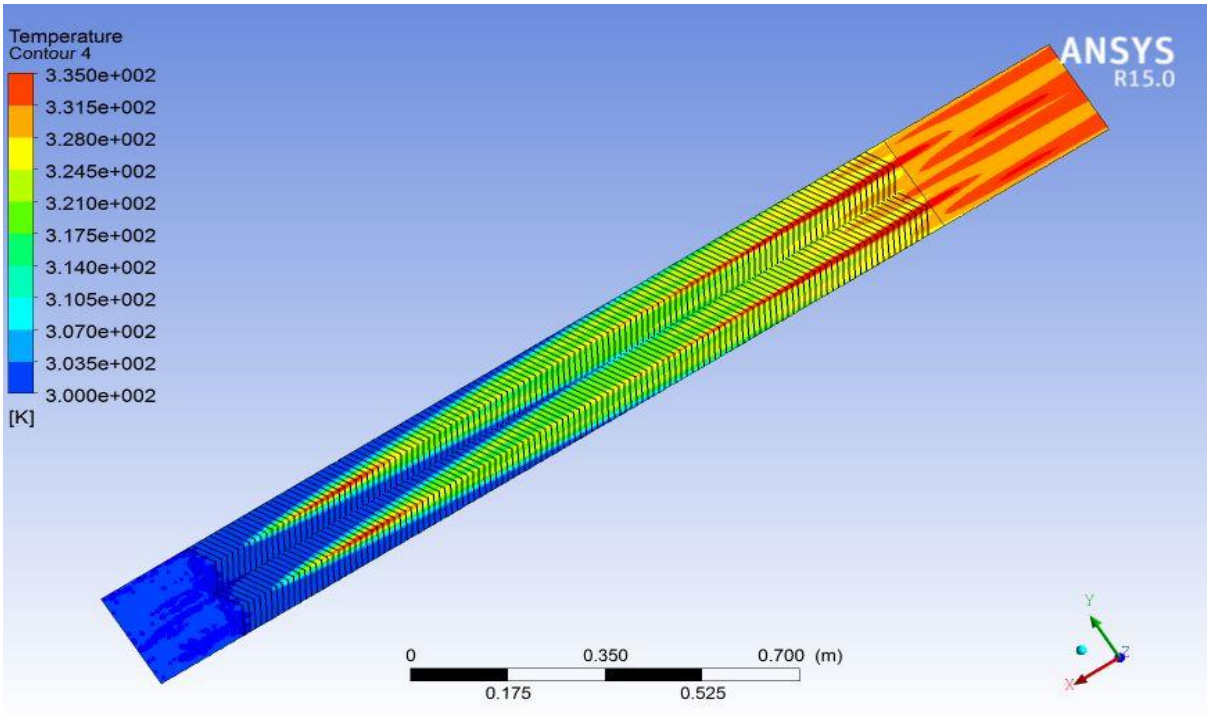

Fig. 5.2 Temp Contours For Absorber Plate with Discrete W-Shaped Ribs(Re=6000)

The enhancement of the wall heat transfer by the use of V-shaped ribs is based on the observation of the creation of secondary flow cell due to angling of the rib resulting in a region of higher heat transfer near the leading end. By splitting the long angled rib into a V-shape to form two leading ends and a single trailing end, a much larger (about double) region of high heat transfer is produced. It is, in fact, the formation of two secondary flows cells instead of one as in the case of transverse rib that results in higher overall heat transfer in the case of V-shaped ribs. Discretization further increases the number of heat transfer regions.The increment in heat transfer using discrete W-shaped ribs on the absorber plate as compared to smooth duct can be depicted from the Fig. 5.3. Fig. 5.4 reveals that the increment in Nusselt number is accompanied by an increase in friction factor also.

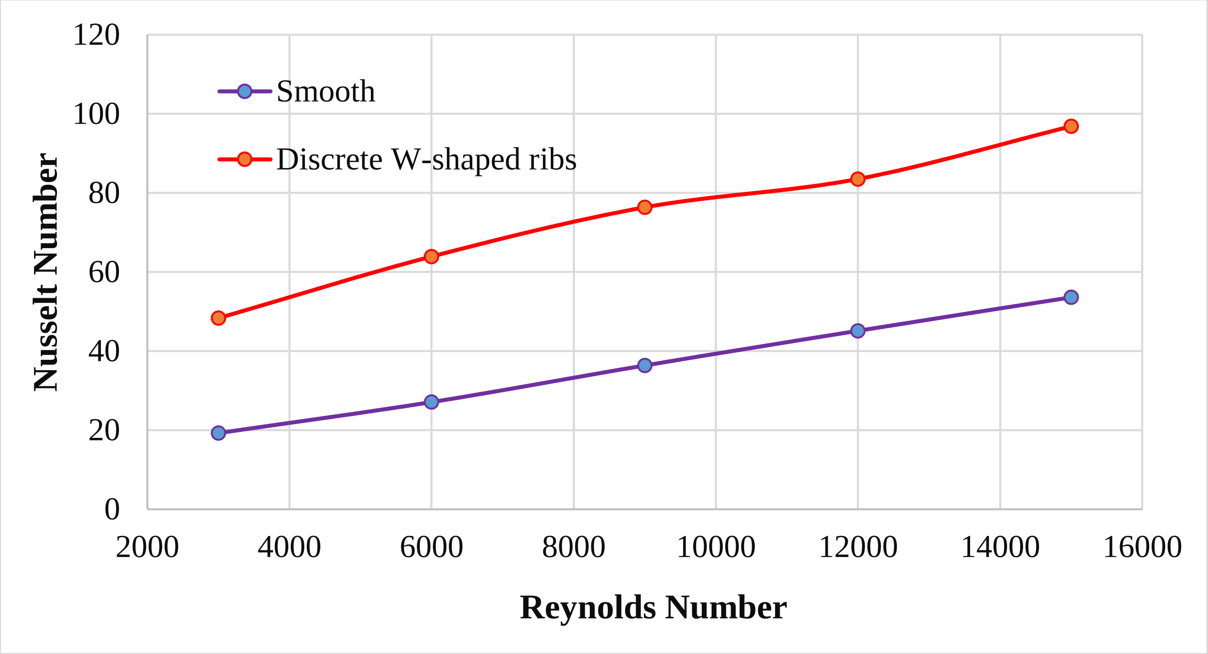

Fig. 5.3 Nusselt Number Vs Reynolds Number for Discrete W-Shaped Ribs

The graph has been plotted for Nusselt number at different Reynolds number. As the value of Reynolds number increases heat gain by the air increases due to increment in heat transfer coefficient which results in enhancement of Nusselt number too. But the value of Nusselt number at each Reynolds number is higher for absorber plate with discrete W-shaped ribs as compared to the smooth duct.

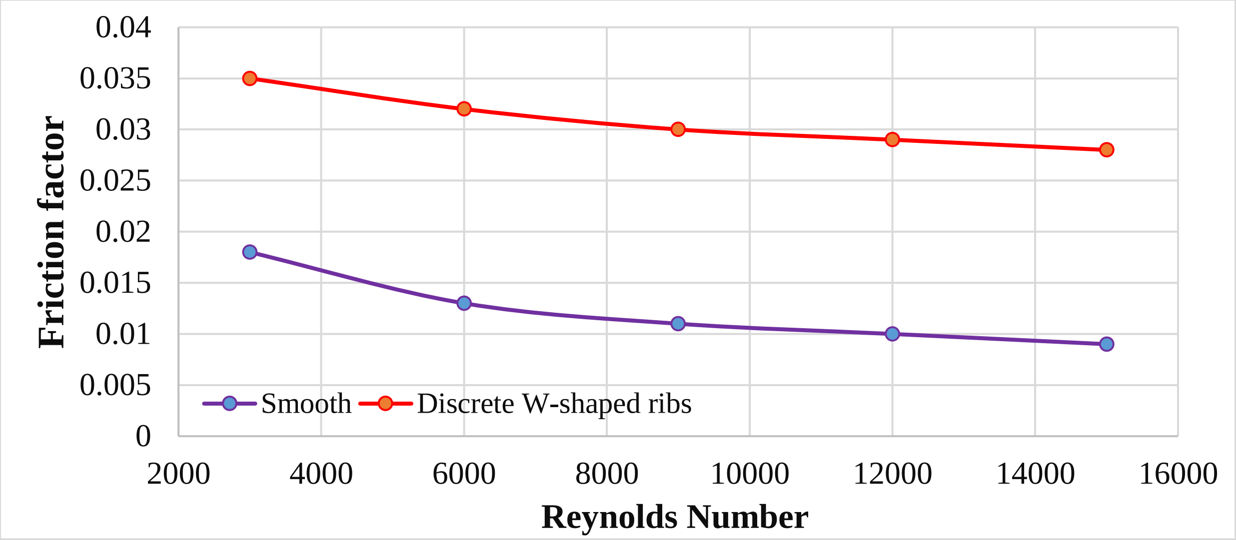

Fig. 5.4 Friction Factor Vs Reynolds Number for Discrete W-Shaped Ribs

Table 5.1 Comparison of Results Obtained for Reynolds Number 9000

Obtained parameters	**Smooth**	**Continuous W-shaped (α= 60˚e/D=1.5mm)**	**Discrete W-shaped (α= 60˚e/D=1.5mm)**
T_o(K)	316.78	321.16	322.32
ΔT(K)	16.78	21.16	22.32
Nu	36.36	62.78	76.36
ΔP(Pascal)	8.019	16.358	21.687
f	0.011	0.023	0.030
Q_u(W)	203.73	256.91	269.62

5.2 Effect of Relative Roughness Height

It has been found that the artificial roughness on the absorber plate of the roughened duct results in considerable enhancement of heat transfer. This enhancement is, however, accompanied by a substantial increase in friction factor. It is, therefore, desirable that to select the roughness geometry such that the heat transfer is maximized while keeping the friction losses at the minimum possible value.

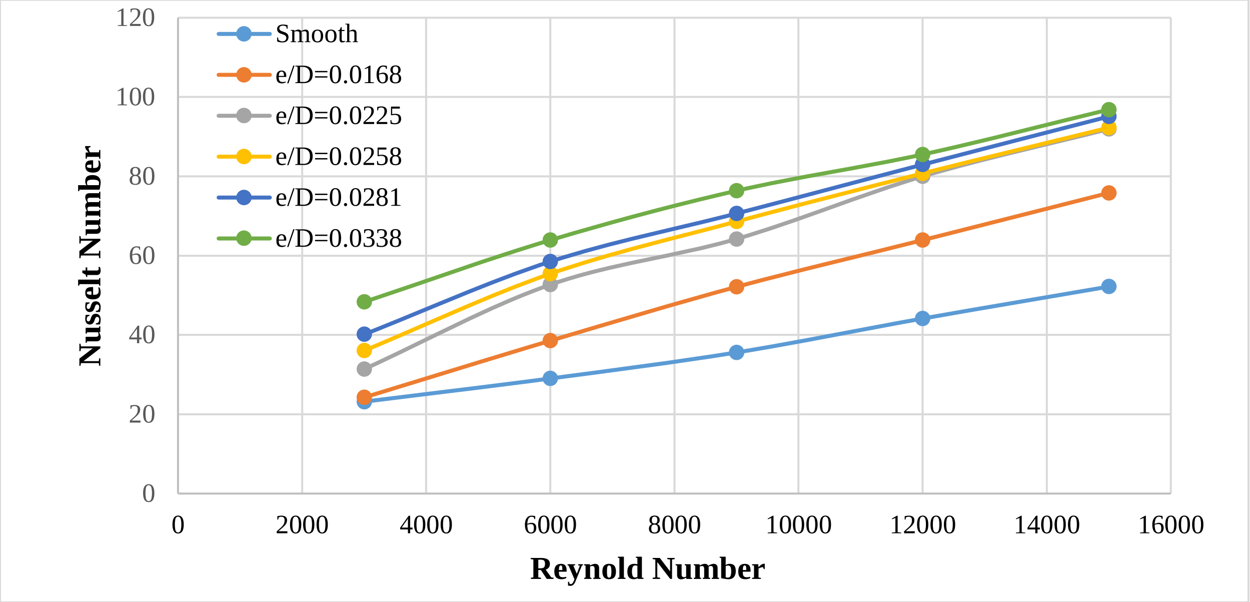

Fig. 5.5 Variation of Nusselt number with Relative roughness height

This requirement of the collector can be fulfilled by considering the heat transfer and friction characteristics simultaneously. A parameter that facilitates the simultaneous consideration of thermal and hydraulic performance is given by as $(Nu/Nu_s)/(f/f_s)^{1/3}$. Fig. 5.5 and 5.6 shows the variation of Nusselt number and Friction factor with relative roughness height.

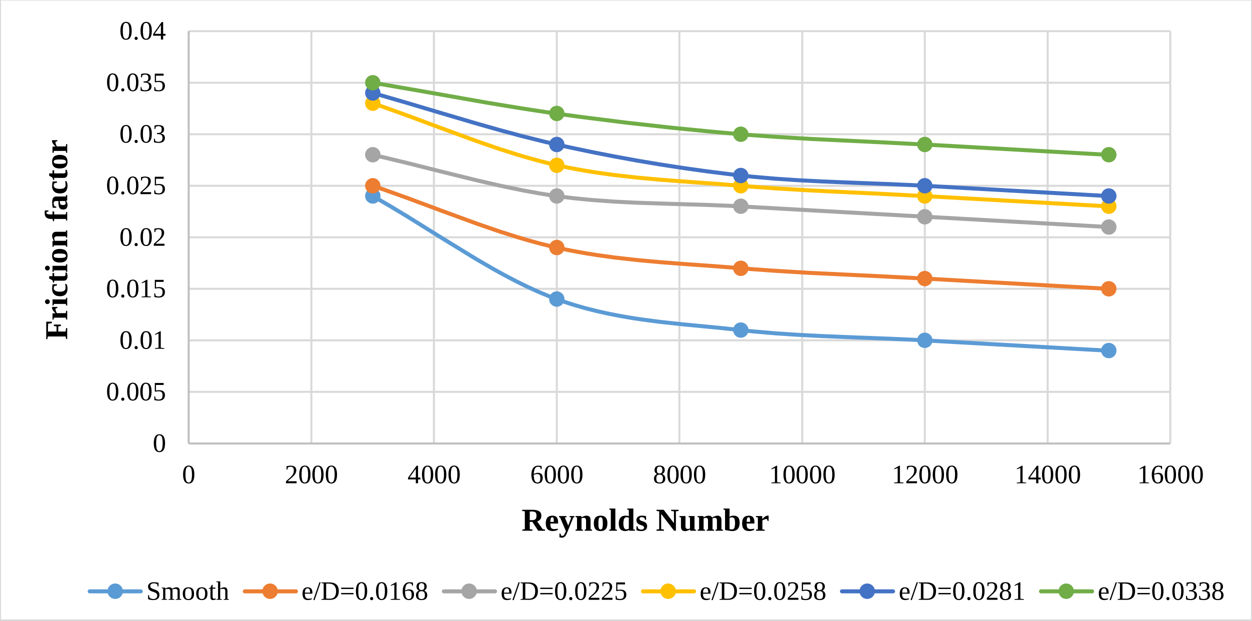

Fig. 5.6 Variation of Friction Factor With Relative Roughness Height

From the above observations, it is concluded that the increase in relative roughness height results in an increase in Nusselt number as well as friction factor at a given value of Reynolds number. It is also observed that the rate of increase of friction factor is higher than that of the Nusselt number. It can be seen that ribs of smaller height remain submerged in the laminar sub-layer, so the flow is likely to be similar both for smooth and roughened duct. This corresponds to a hydraulically smooth flow regime. For relative roughness height (e/D) 0.0168 to 0.0338 Nusselt number improves noticeable as compare to friction factor. Nusselt number increases 2.085 times for discrete W-shaped ribs roughened duct for e/D=0.0338 as compare to smooth duct.

Table 5.2 Comparison of Results for Different Relative Roughness Height (Re= 9000)

Obtained Parameters	**Smooth**	**e/D$_h$**				
		0.0168	**0.0225**	**0.0258**	**0.0281**	**0.0338**
T$_o$(K)	316.78	318.92	319.51	320.01	320.35	321.16
ΔT(K)	16.78	18.92	19.51	20.01	20.35	21.16
Nu	36.36	52.12	60.20	68.59	70.62	76.36
ΔP(Pascal)	8.019	12.608	16.348	17.947	19.147	21.687
f	0.011	0.017	0.023	0.025	0.026	0.030
Q$_u$(W)	203.7	229.67	236.84	242.9	247.03	256.86

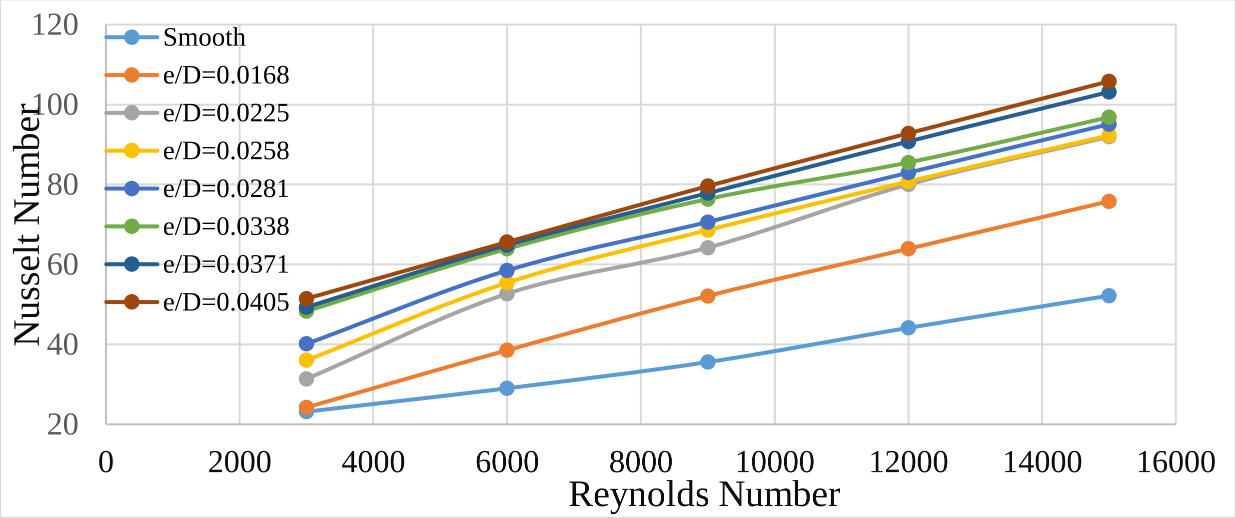

Fig. 5.7 Variation of Nusselt Number with Relative Roughness Height

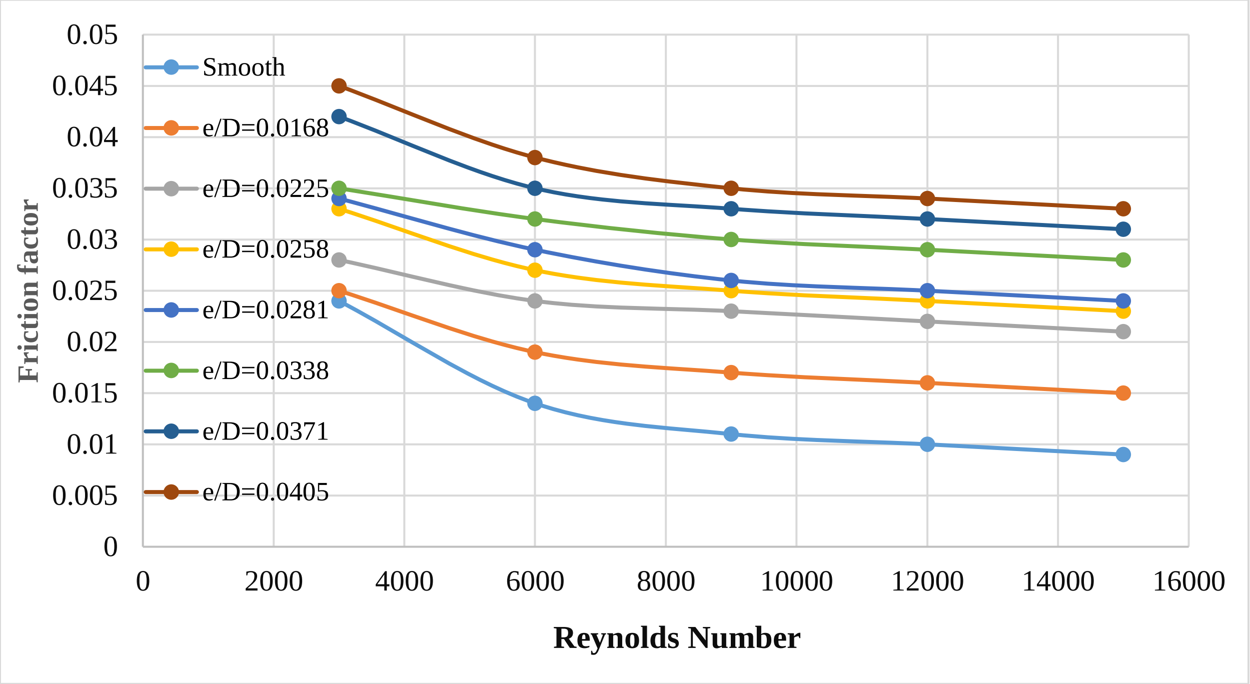

Fig. 5.8 Variation of Friction Factor With Relative Roughness Height

Fig. 5.7 and 5.8 show that for relative roughness height 0.0371 and 0.0405 Nusselt number increases very less as compare to friction factor because of the re-attachment point is disturbed. Nusselt number improves 1.92% for e/D= 0.0371 and 4.22% for e/D= 0.0405 as compare to Nusselt number for e/D= 0.0338, but friction factor increases rapidly such as 10% for e/D= 0.0371 and 16.66% for e/D= 0.0405 as compare to friction factor for e/D= 0.0338.

5.3 Effect of Angle of Attack

Angle of attack (α) is the inclination of rib with direction of air flow in duct. It has been observed during experiments and CFD analysis that changing the value of angle of attack has a considerable effect on heat transfer and the friction factor as well. It appears that the flow separation in the secondary flow resulting from the presence of discrete W-shaped ribs and the movement of resulting vortices combines to yield an optimum value of the angle of attack. Fig. 5.9(a)-(d) shows the modeling of SAH with inclined ribs having different angle of attacks.

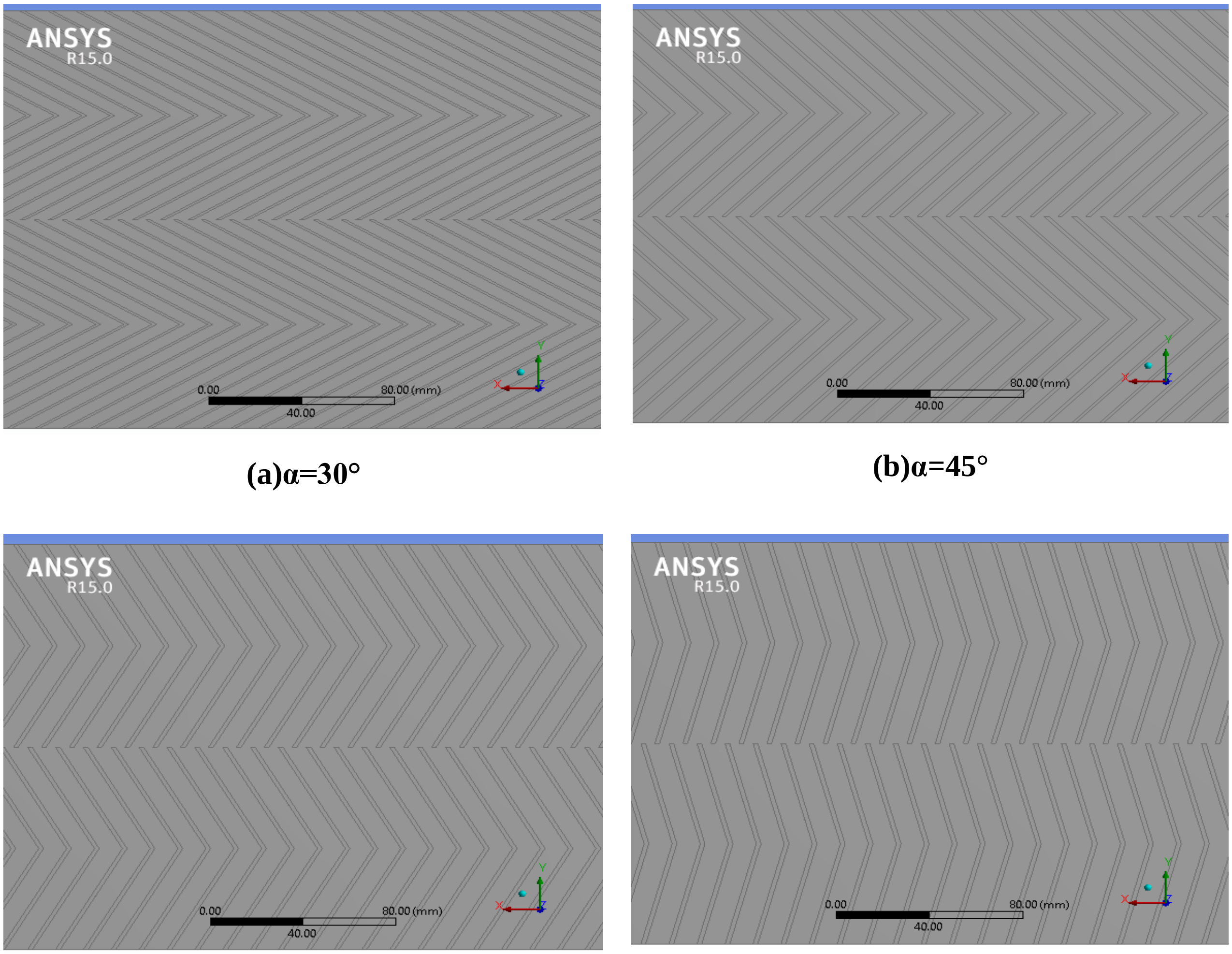

(a)α=30° **(b)α=45°**

(c)α=60° **(d)α=75°**

Fig. 5.9 Modelling of SAH for different angle of attack

An increase in the angle of attack has been found to generally increase the Nusselt number till an angle of attack of about 60° is attained while a further increase in the angle tends to decrease the Nusselt number.The maximum enhancement of Nusselt number and friction factor as a result of providing artificial roughness has been found to be 1.99 and 2.32 times that of smooth duct for an angle of attack of 60°. It is seen that there exists an angle of attack that corresponds to the maximum values of both Nusselt number and the friction factor. This trend has been illustrated in fig. 5.10 where a clear maximum in the value of Nusselt number can be observed at an angle of attack of approximately 60° although the value of corresponding maximum Nusselt number increases with increasing Reynolds number.

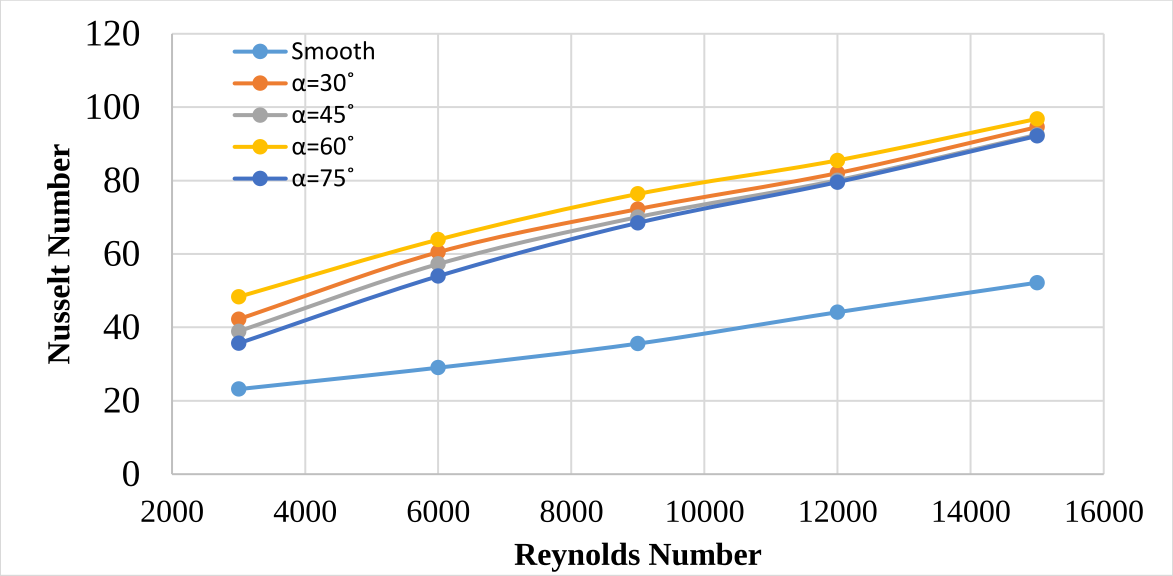

Fig. 5.10 Nusselt Number Vs Angle of attack

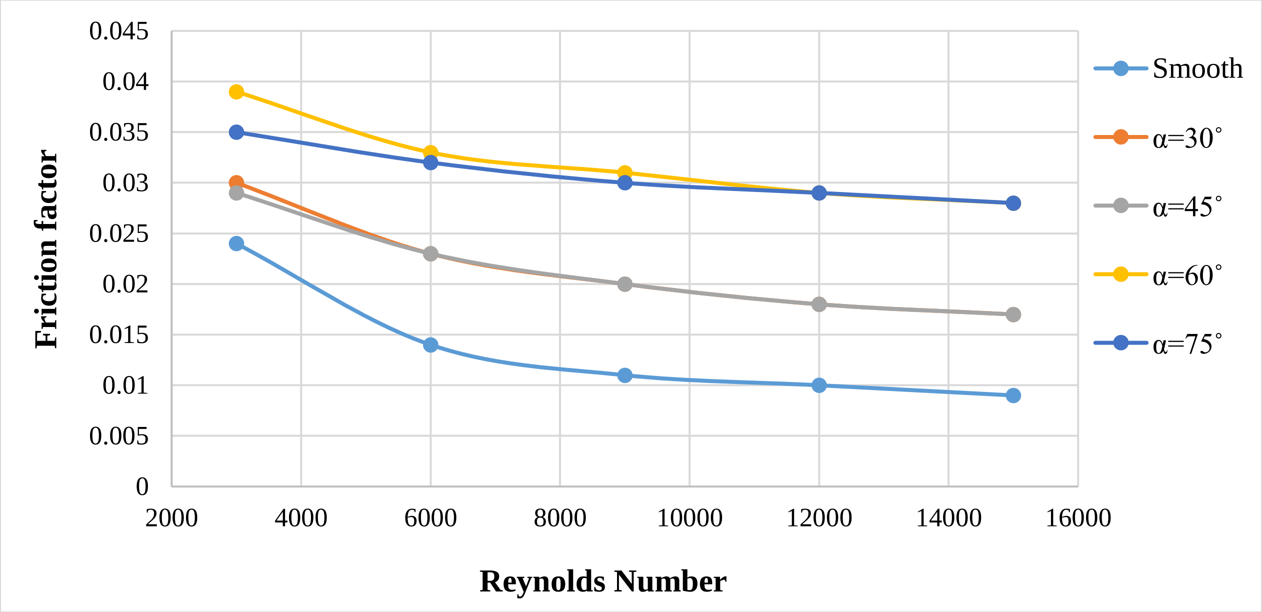

Fig. 5.11 Friction Factor vs Angle of Attack

The variation of friction factor with angle of attack is shown in Fig. 5.11. Thus, the roughness elements must be oriented in such a way as to result in an angle of attack of about 60° to avail maximum enhancement from the use of roughness elements.

5.4 Effect of Discretization

It has been found that the surface with compound roughness (discrete rib) can perform better than the surface with single roughness (continuous rib). It is well known that ribs break the viscous sub-layer and create local wall turbulence, resulting in enhanced heat transfer. The discretization may induce vortices in and around the grooves, which may further enhance the heat transfer and increases the number of heat transfer regions.

Introduction of discretization in the rib allows release of fluid belonging to secondary flow and main flow through the gap. The main flow passing through the gap is the developed flow with thicker boundary layer consisting of viscous sub-layer. As a result discretization, the secondary flow along the rib joins the main flow to accelerate it which energizes the retarded boundary layer flow along the surface.

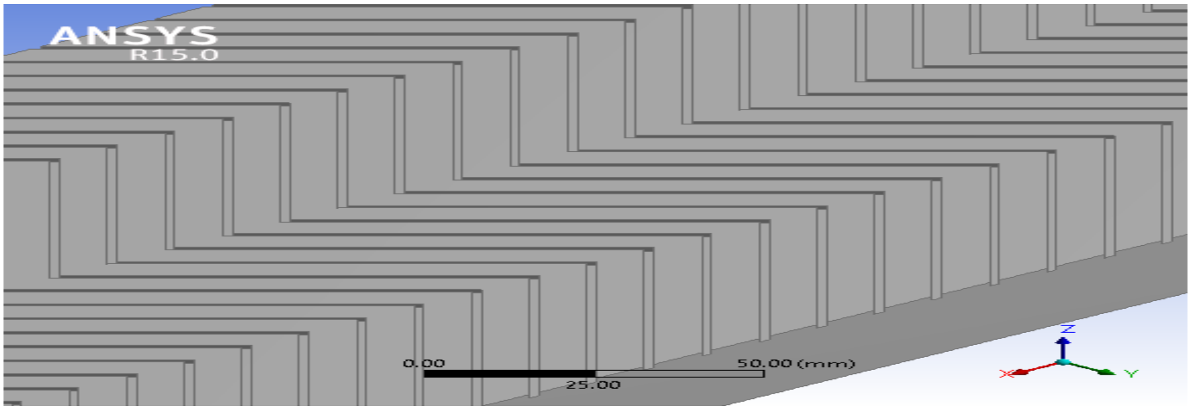

(a) Continuous W-shaped ribs

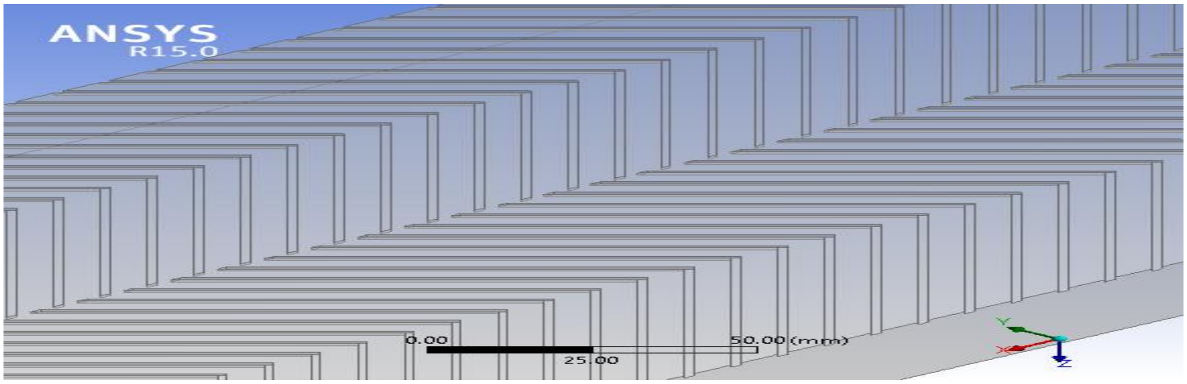

(b) Discrete W-Shaped Ribs

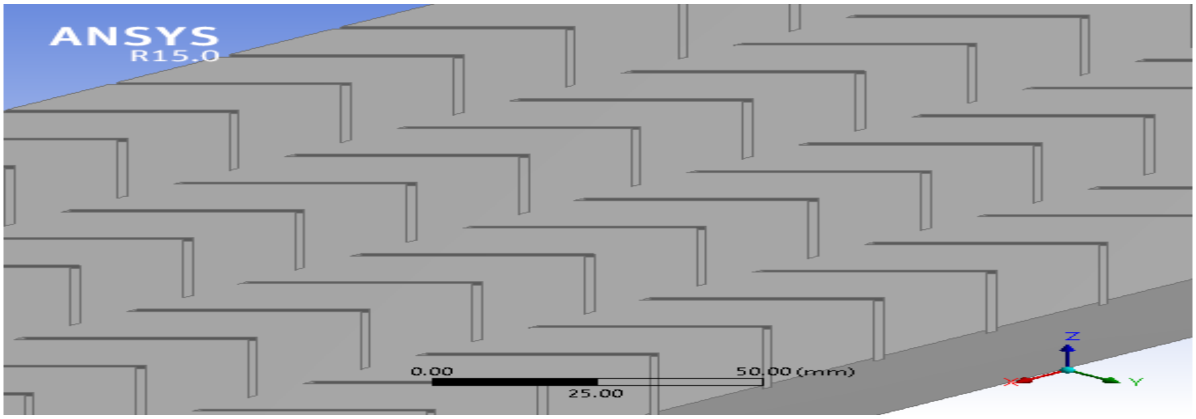

(c) Multiple Discrete W-shaped ribs

Fig. 5.12 Modelling of SAH for Variation in Discretization

Discretization further increases the number of heat transfer regions. Thus, the heat transfer through the gap width area increases behind the rib and higher outlet temperature is obtained as compared to continuous W-shaped ribs. Fig. 5.12(a-c) shows the model of solar air heater with different W-shaped ribs.

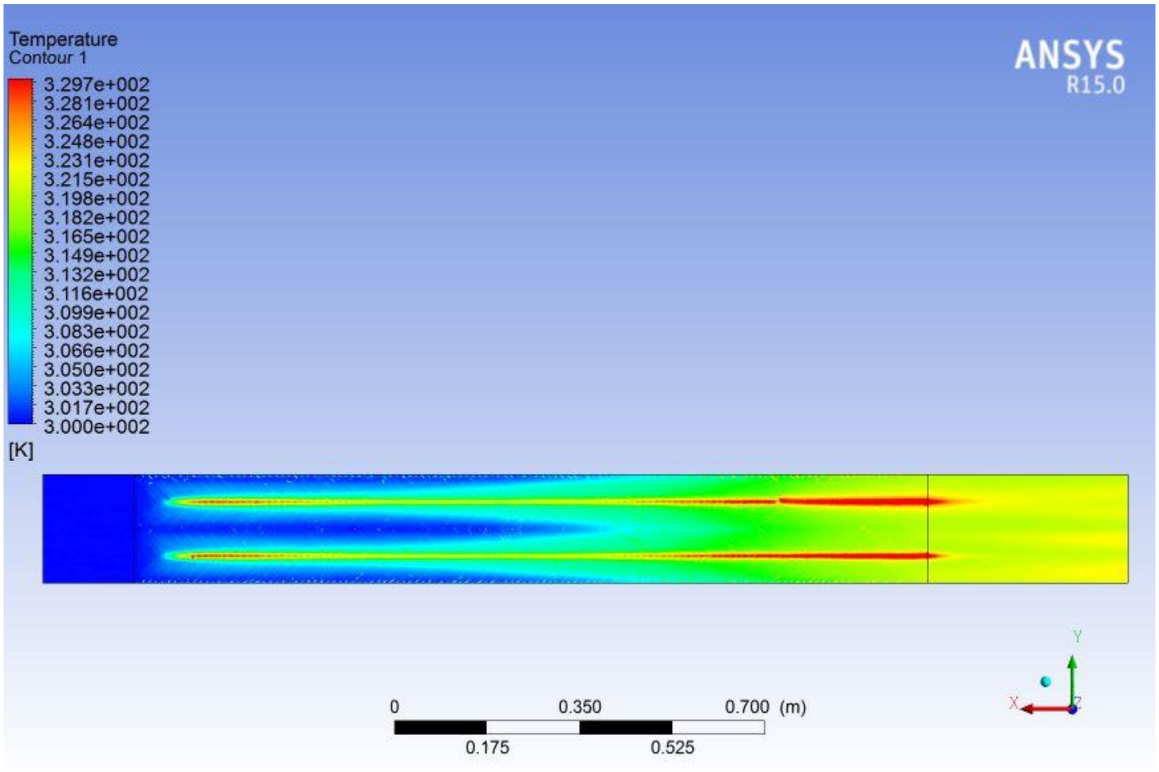

(a) Temperature Contour of Mid Plane of SAH with Continuous W-shaped ribs

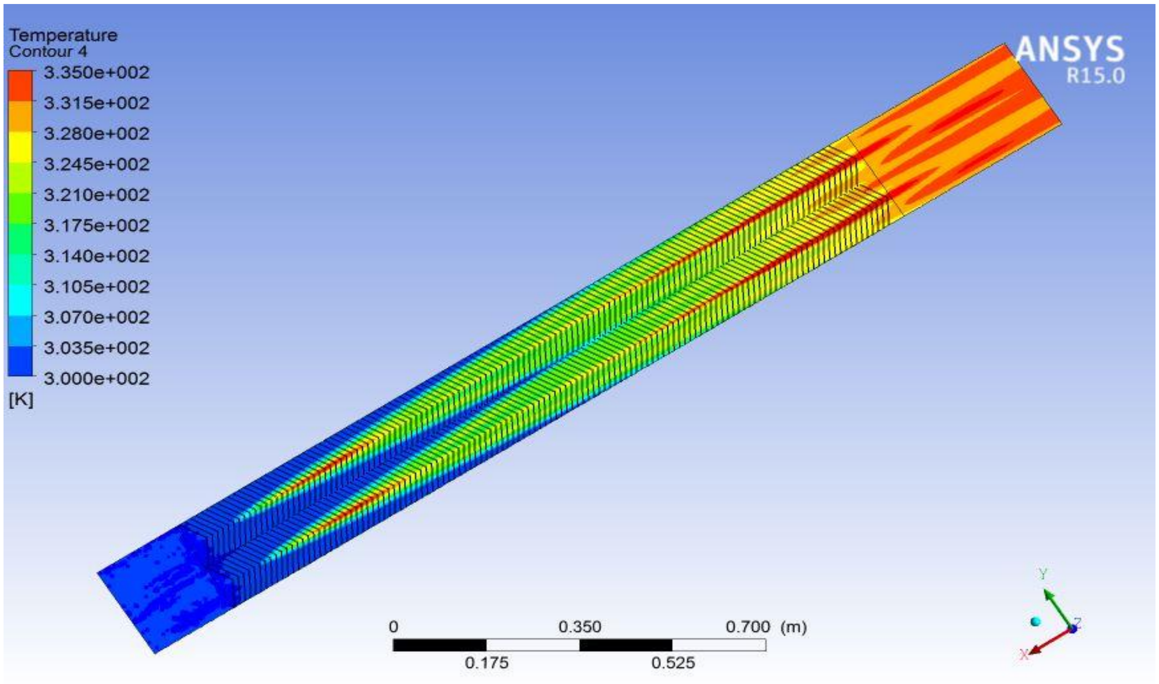

(b) Temperature Contour of Mid Plane of SAH with Discrete W-shaped ribs

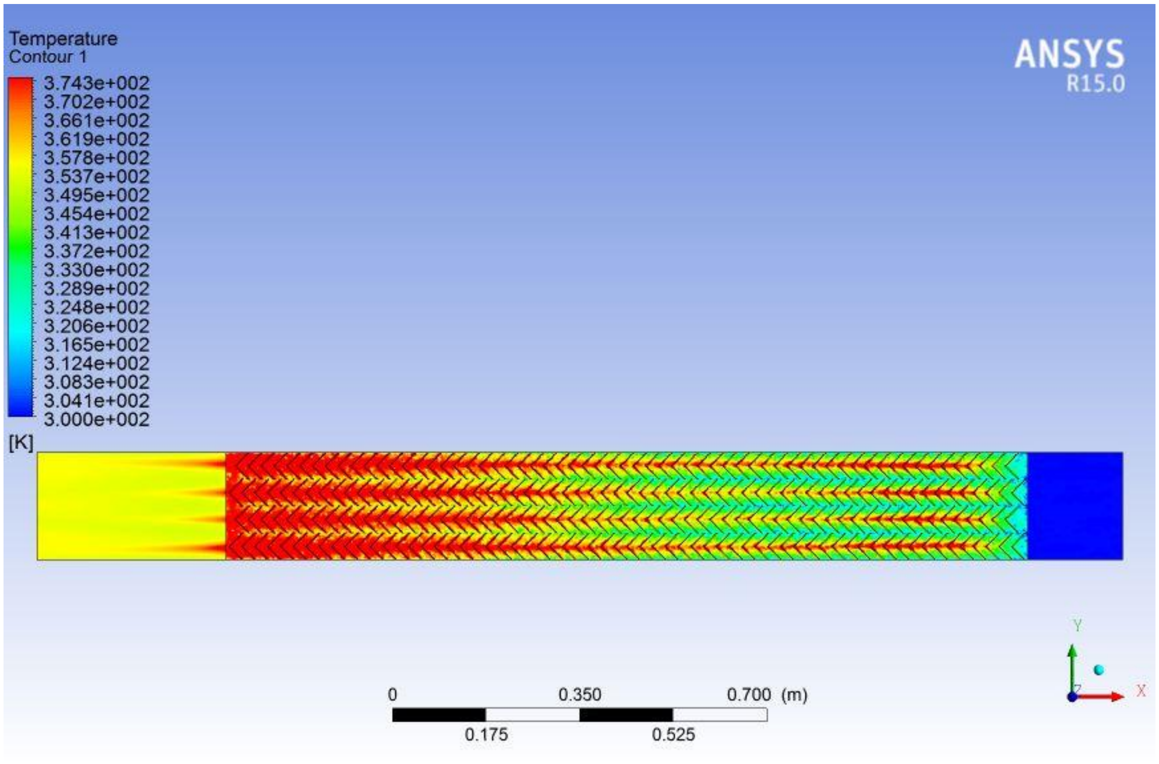

(c) Temperature Contour of Mid Plane of SAH with Multiple Discrete W-shaped rib

Fig. 5.13 Temperature Contour of Mid Plane of SAH with Discretization

Fig. 5.13(a-c) show the temperature contours of mid plane of the solar air heater with continuous W-shaped ribs and multiple discrete W-shaped ribs respectively. There is a large increment in heat transfer regions in multiple discrete W-shaped ribs roughened solar air heater as compare to continuous and discrete W-shaped ribs roughened solar air heater

An increase in discretization has been found to generally increase the Nusselt number. The maximum enhancement of Nusselt number and friction factor as a result of providing multiple discrete W-shaped roughness has been found to be 2.25 and 3.27 times that of smooth duct for Reynolds number 9000. This trend has been illustrated in fig. 5.14 where a clear maxima in the value of Nusselt number can be observed for multiple discrete W-shaped ribs although the value of corresponding maximum Nusselt number increases with increasing Reynolds number.

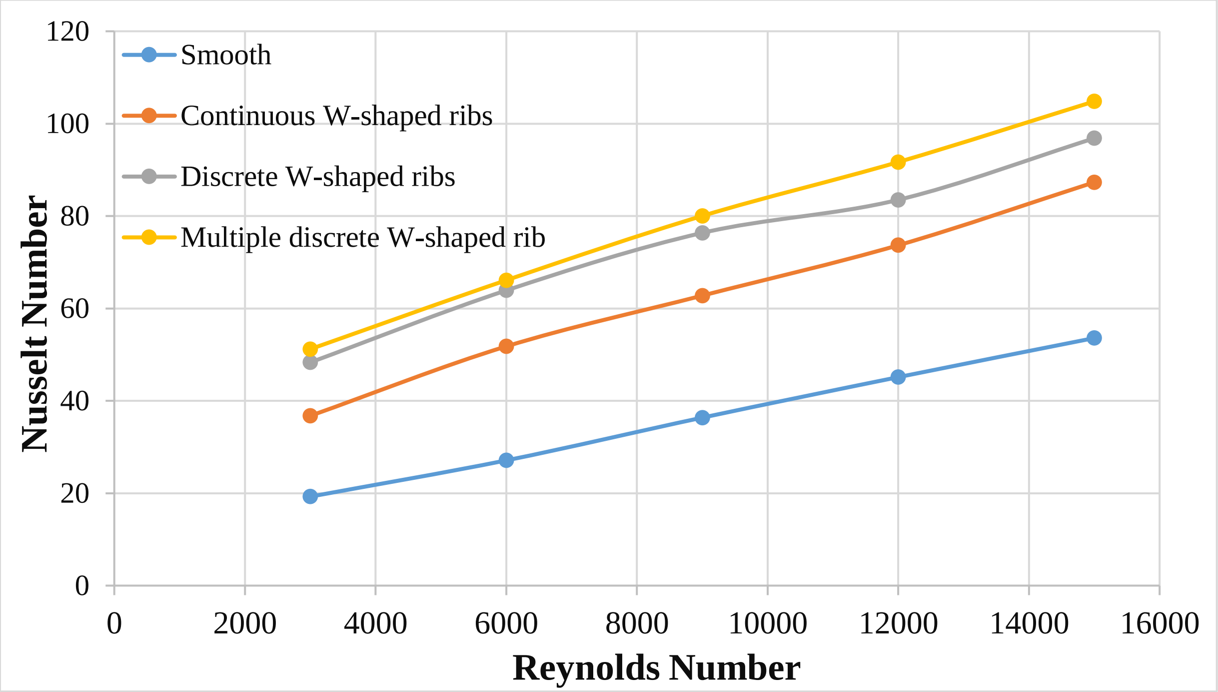

Fig. 5.14 Variation in Nusselt Number With Discretization

It is seen that for higher values of Reynolds number increment in friction factor is less as compare to Nusselt number. This trend has been shown in fig. 5.15 where a clear maxima in the value of friction factor can be observed for multiple discrete W-shaped ribs although the value of corresponding friction factor decreases with increasing Reynolds number.

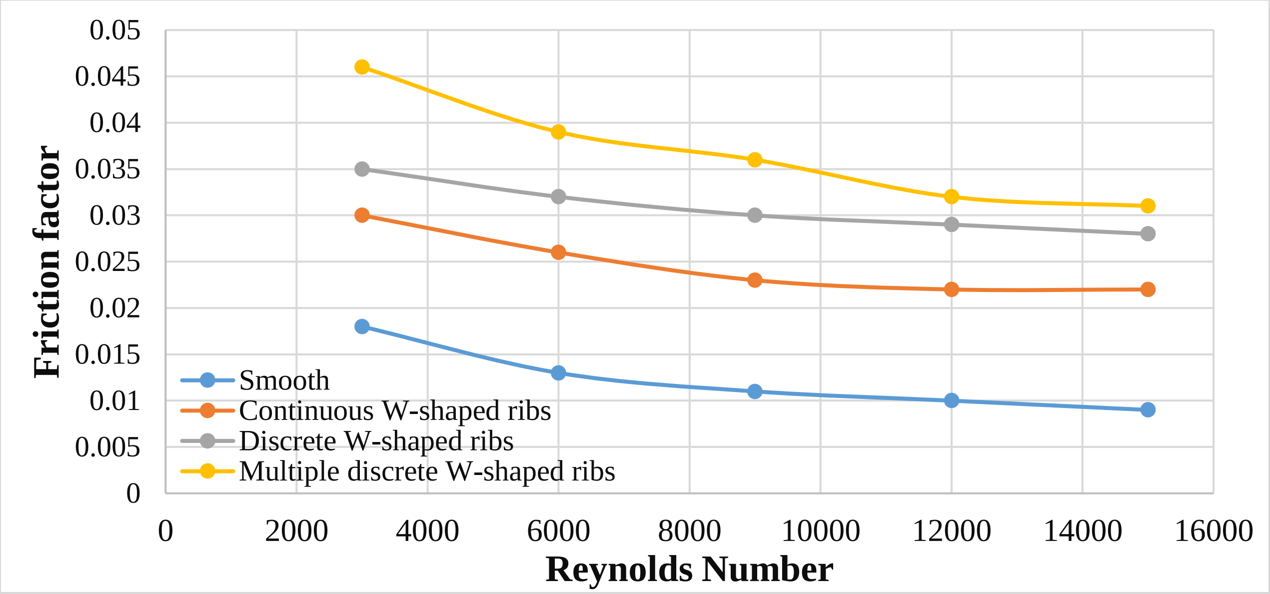

Fig. 5.15 Variation in Friction Factor With Discretization

Table 5.3 Comparison of Results for Different Discretize Geometry of SAH (Re 9000)

Obtained Parameters	**Smooth**	**Continuous W-shaped** **(α= 60˚e/D=1.5mm)**	**Discrete W-shaped ribs** **(α= 60˚e/D=1.5mm)**	**Multiple discrete W-shaped** **(α= 60˚e/D=1.5mm)**
T_o(K)	316.78	321.16	322.32	324.05
ΔT(K)	16.78	21.16	22.32	24.05
Nu	36.36	62.78	76.36	80.03
ΔP(Pascal)	8.019	16.358	21.687	26.73
f	0.011	0.023	0.030	0.036
Q_u(W)	203.7	256.86	270.95	291.95

5.5 Comparison among Different Artificial Roughnesses

To study the comparison among five different artificial roughnesses geometry on the heat transfer and friction of airflow, rectangular duct has been designed. According to ASHARE standard 93–97 the flow system consists of an entry section, a test section, an exit section, and a centrifugal blower. The entry and exit lengths were 177 mm (2.5√WH) and 353 mm

(5√WH) respectively and the test section of the duct is of length 1500 mm (33.75 Dh). The width and height of the duct is 200mm and 25mm respectively. Fig. 5.9(a)-(e) shows the modeling of SAH with different types of roughnesses.

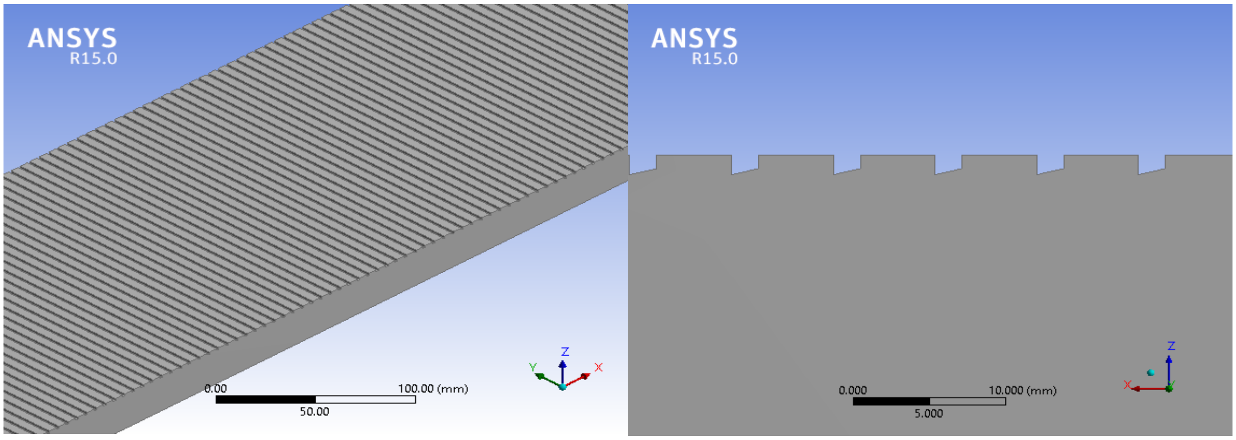

(a) Chamfered shaped ribs

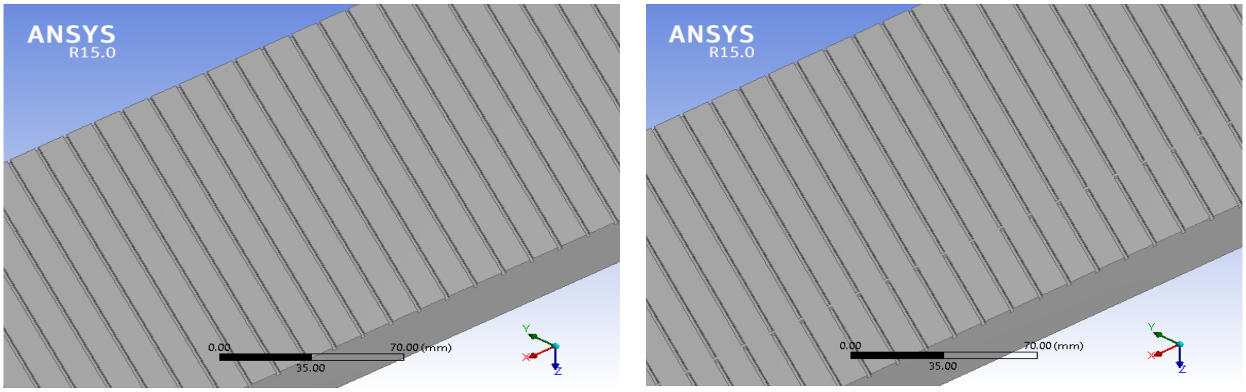

(b)Inclined Ribs

(c)Inclined ribs with gap position

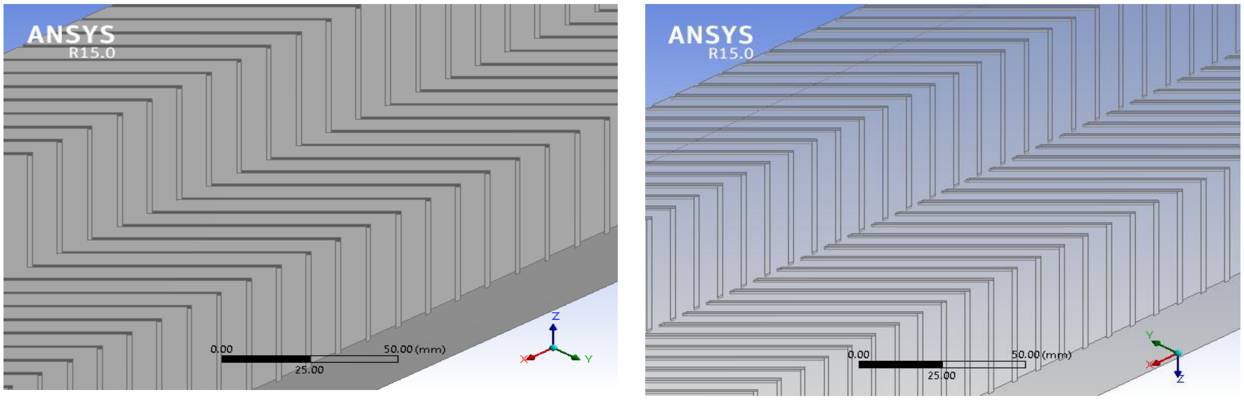

(d)Continuous W-shaped ribs

(e)Discrete W-shaped ribs

Fig. 5.16 Modelling of SAH with Different Artificial Roughnesses

It has been found that the Nusselt number increases as the Reynolds number increases and friction factor decreases as the Reynolds number increases with all types of roughnesses. This trend has been illustrated in fig. 5.18 and fig. 5.19 respectively. It is seen that V-shaped ribs perform better than inclined ribs further discrete ribs perform better as compared to continuous ribs. The enhancement of the wall heat transfer by the use of V-shaped ribs is based on the observation of the creation of secondary flow cell due to angling of the rib resulting in a region of higher heat transfer near the leading end.

By splitting the long inclined rib into a V-shape to form two leading ends and a single trailing end, a much larger region of high heat transfer is produced. The formation of two secondary flows cells instead of one as in the case of inclined rib or chamfered shaped rib that results in higher overall heat transfer in the case of V-shaped ribs. Discretization further increases the number of heat transfer regions. So discrete W-shaped type roughened solar air heater gave more enhancement in heat transfer as compare to inclined rib roughened solar air heater.

The maximum enhancement of Nusselt number was found to be 2.085, 1.04, 1.36 and 1.20 times that for smooth duct for discrete W-shaped ribs, inclined ribs, inclined ribs with gap position and chamfered shaped ribs respectively for Reynolds number 3000. Fig. 5.17(a-d) shows the temperature contours of mid plane of solar air heater with different roughnesses.

Table 5.4 Comparison of Results for Five Different Geometries of SAH (Re 9000)

Obtained parameters	**Smooth**	**Continuous W-shaped**	**Discrete W-shaped**	**Inclined Ribs**	**Inclined Ribs with gap position**	**Chamfered ribs**
T_o(K)	316.78	321.16	322.32	321.72	322.01	323.19
ΔT(K)	16.78	21.16	22.32	21.72	22.01	23.19
Nu	36.36	62.78	76.36	43.02	59.03	52.10
ΔP(Pascal)	8.019	16.358	21.687	13.54	15.18	15.42
f	0.011	0.023	0.030	0.019	0.021	0.022
Q_u(W)	203.7	256.86	270.95	263.66	267.19	281.51

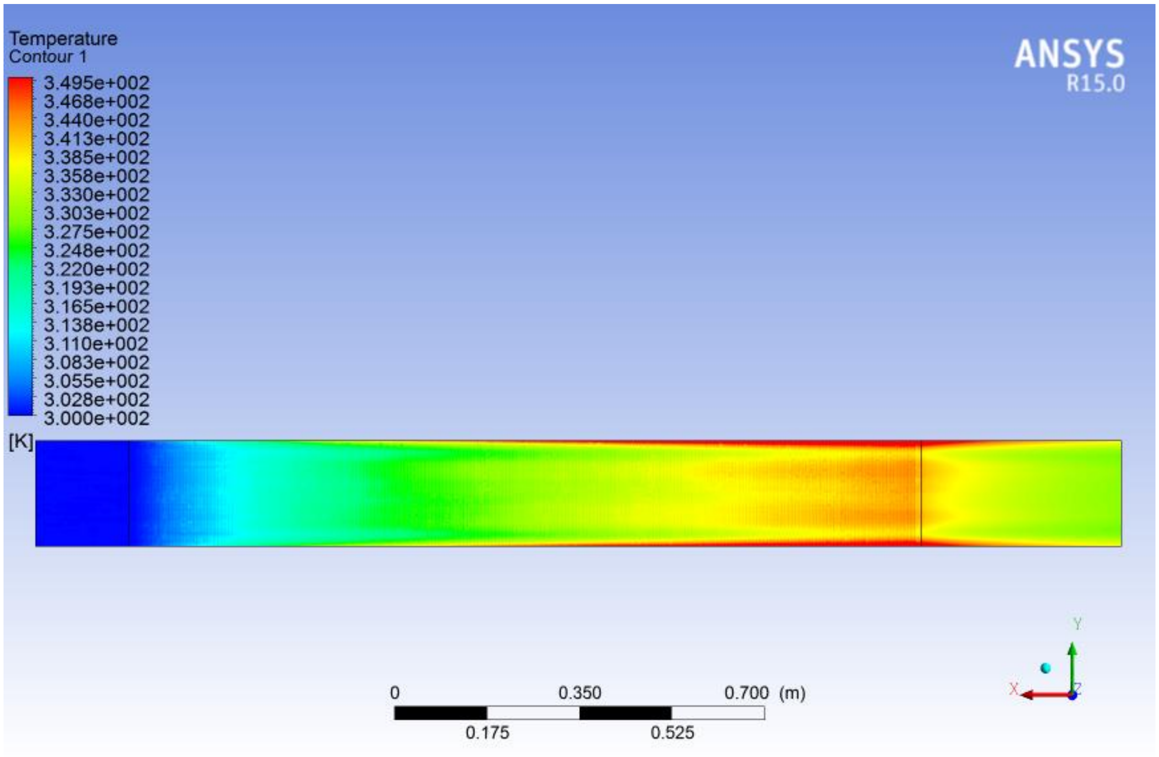

(a) Temperature Contour of Mid Plane of SAH with Chamfered Shaped Ribs

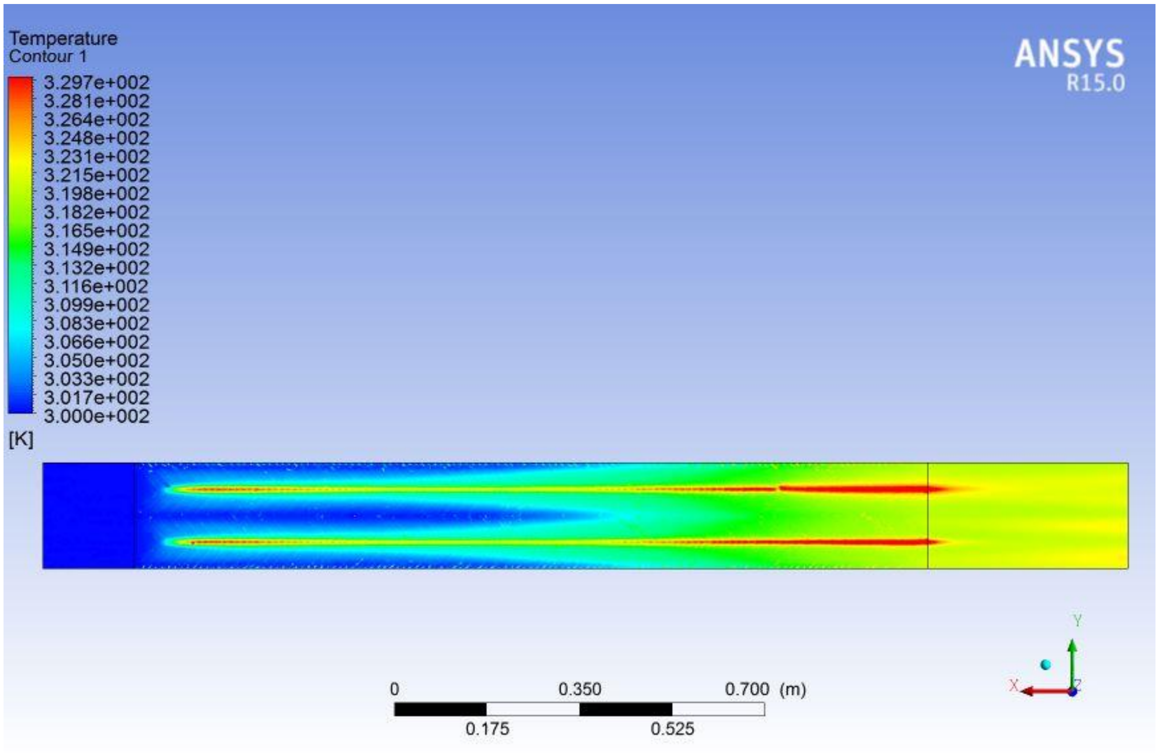

(b) Temperature Contour of Mid Plane of SAH with Continuous W-Shaped Ribs

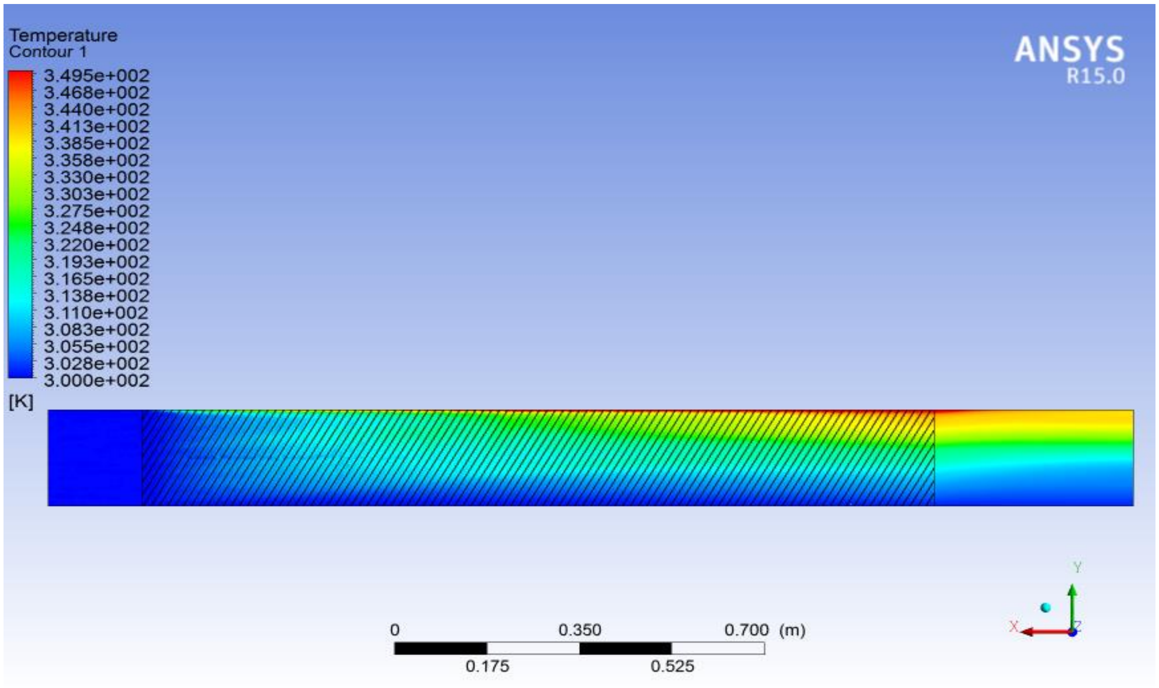

(c) Temperature Contour of Mid Plane of SAH With Inclined Ribs

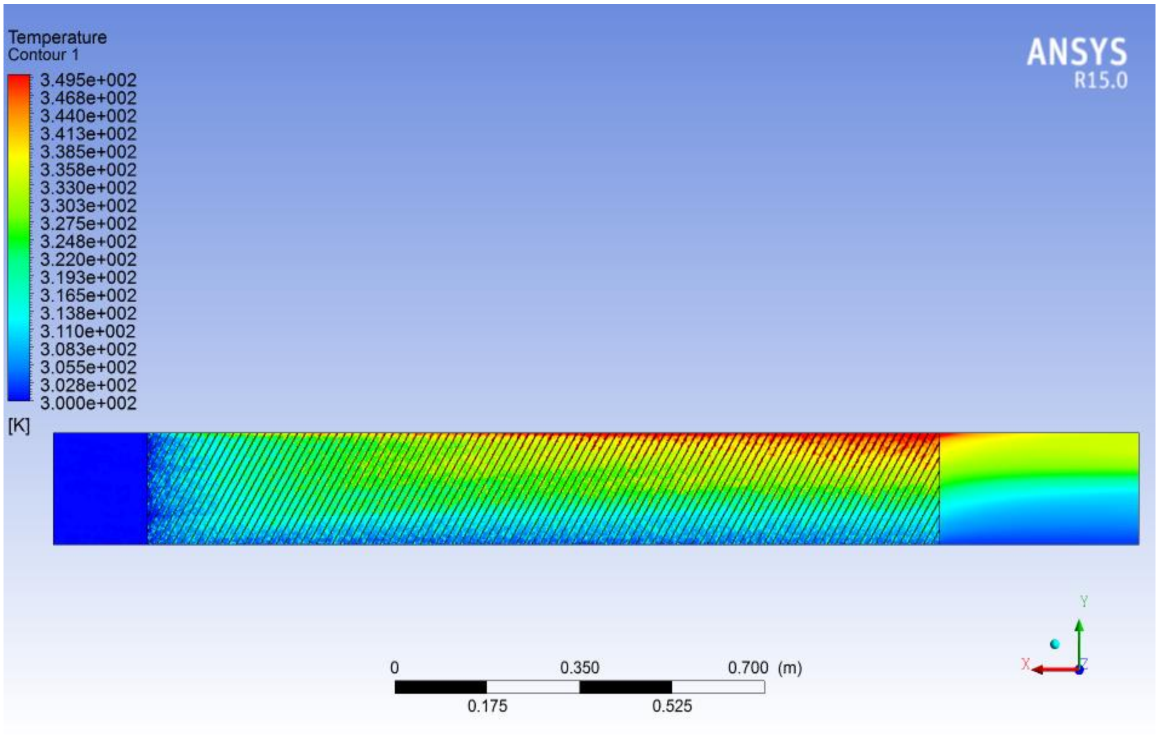

(d) Temperature Contour of Mid Plane of SAH with Inclined Ribs with Gap Position

Fig. 5.17 Temperature Contour Of Mid Plane of SAH with Different Roughnesses

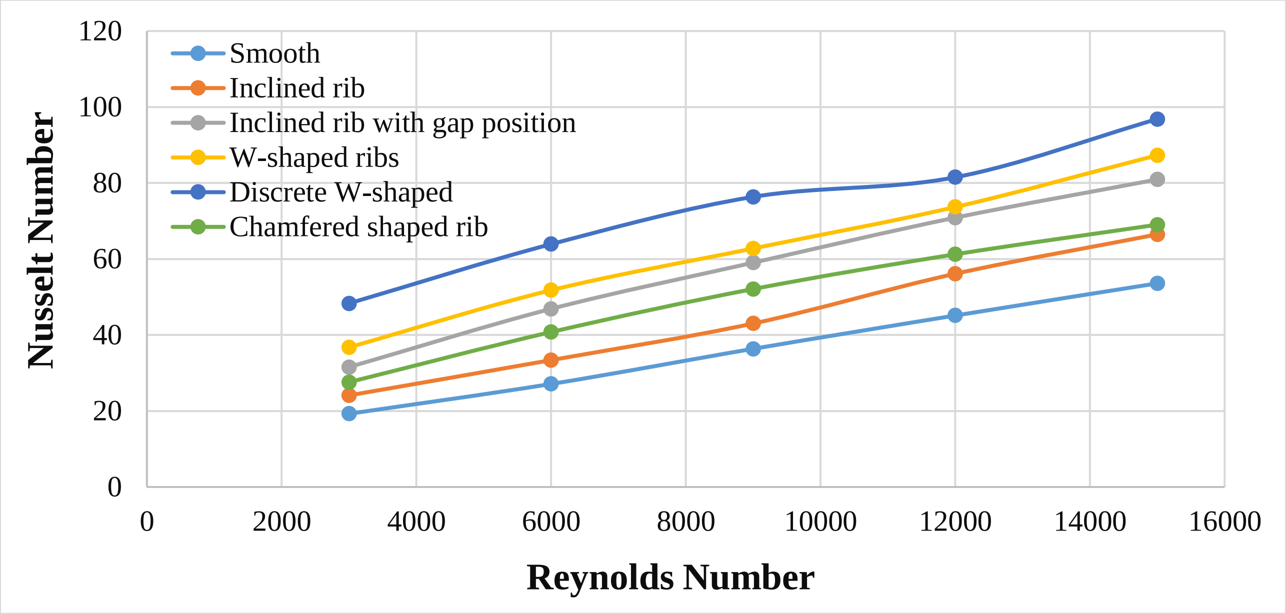

Fig. 5.18 Variation in Nusselt Number for Different Types of Roughnesses

The maximum enhancement of friction factor was found to be 1.65, 1.083, 1.25 and 1.33 times that for smooth duct for discrete W-shaped ribs, inclined ribs, inclined ribs with gap position and chamfered shaped ribs respectively for Reynolds number 3000.

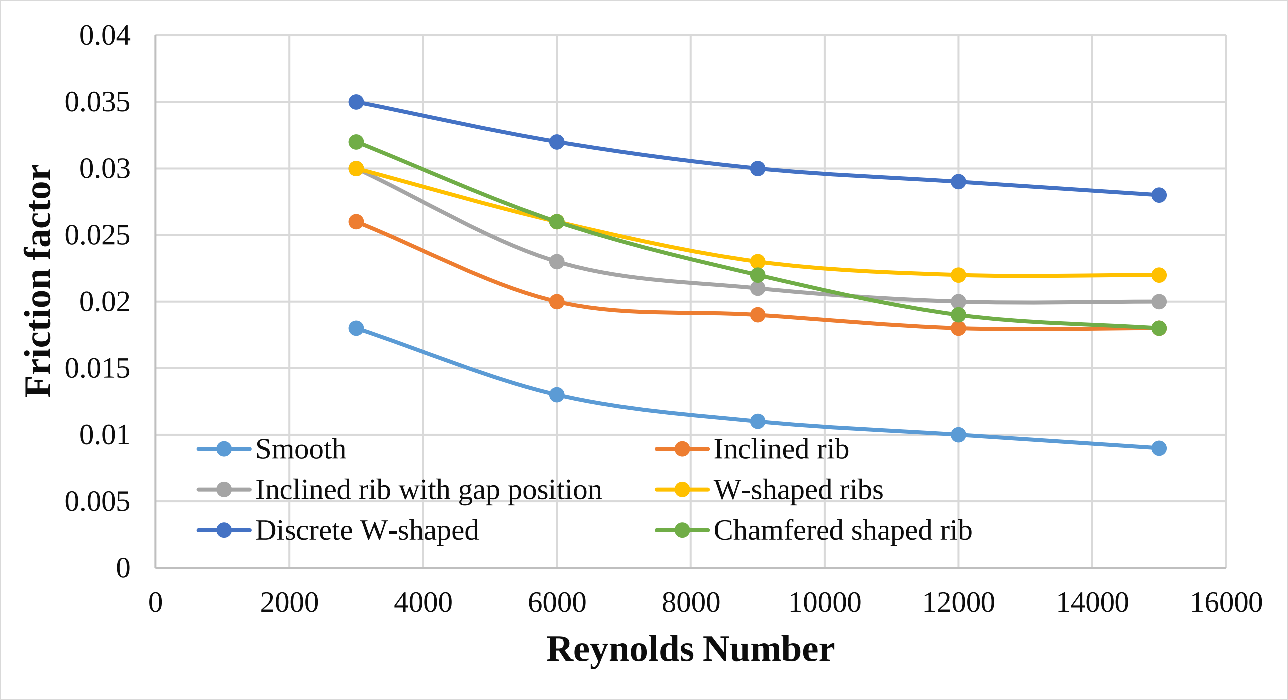

Fig. 5.19 Variation in Nusselt Number for Different Types of Roughnesses

It is also found that for small values of Reynolds number friction for chamfered shaped ribs is much higher as compare to other types of ribs like inclined ribs, continuous W-shaped ribs but value of Nusselt number is less.

5.6 Correlation for Nusselt Number and Friction Factor

Correlation can be used to predict thermo-hydraulic performance or to determine optimum geometric parameters for a particular application. Statistical correlations are presented all combinations of geometric and flow parameters within the range that the Nusselt number and friction factor are strong functions of system and operating parameters of roughened duct, namely the Reynolds number (Re), relative roughness height (e/Dh) and angle of attack of flow (a). The functional relationships for Nusselt number can be written as

$$\mathbf{Nu = 0.05 + 0.0056\,\alpha + 0.004477\,Re + 893\,e/D_h} \qquad \mathbf{5.1}$$

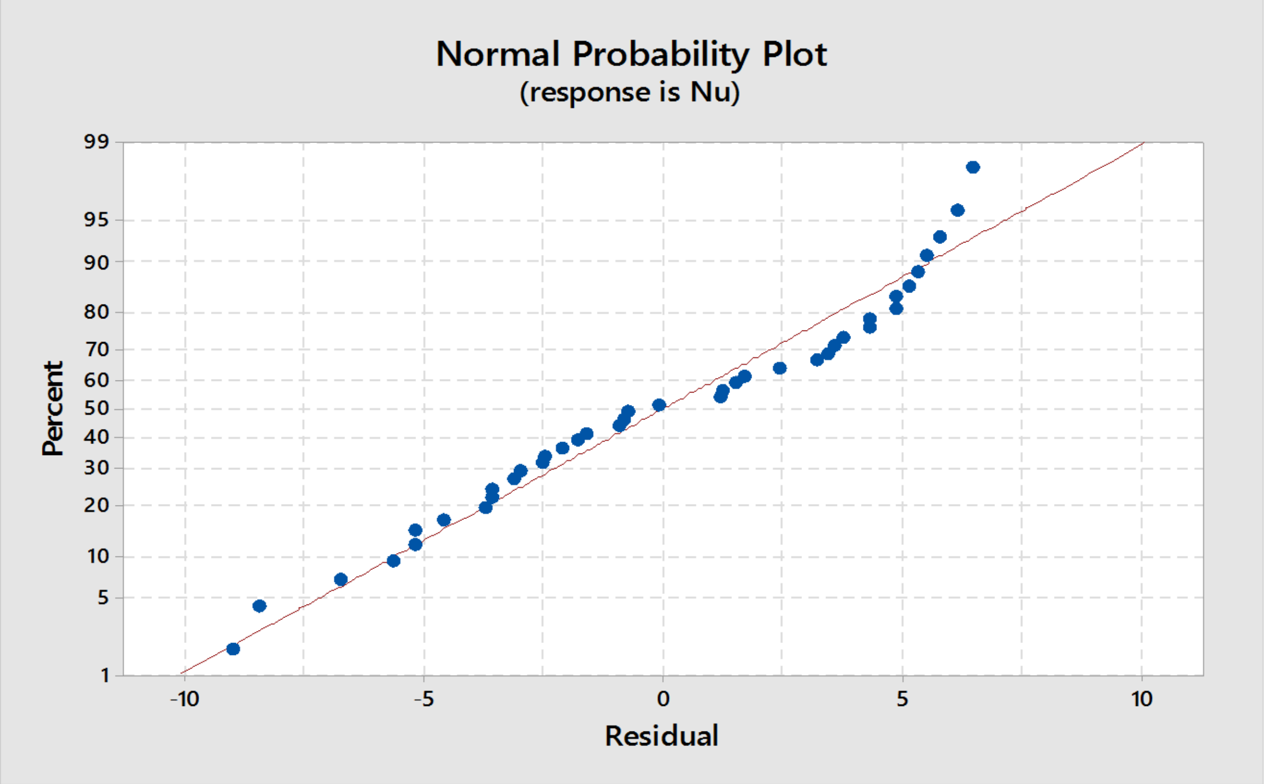

Fig. 5.20 Normal Probability Plot for Nusselt Number

Fig.5.20 shows the plot of simulated values and the values predicted using Eq. 5.1. It can be seen that all 40 data points lie within the deviation line ±10%. This graph implies that 10-90% values of Nu comes under residual -5 to 5. Residual means the error between simulated value and obtained value through Eq. 5.1.

The functional relationships for friction factor can be written as

$$\mathbf{f = 0.00220 + 0.000269\,\alpha - 0.000001\,Re + 0.5254\,e/D} \qquad 5.2$$

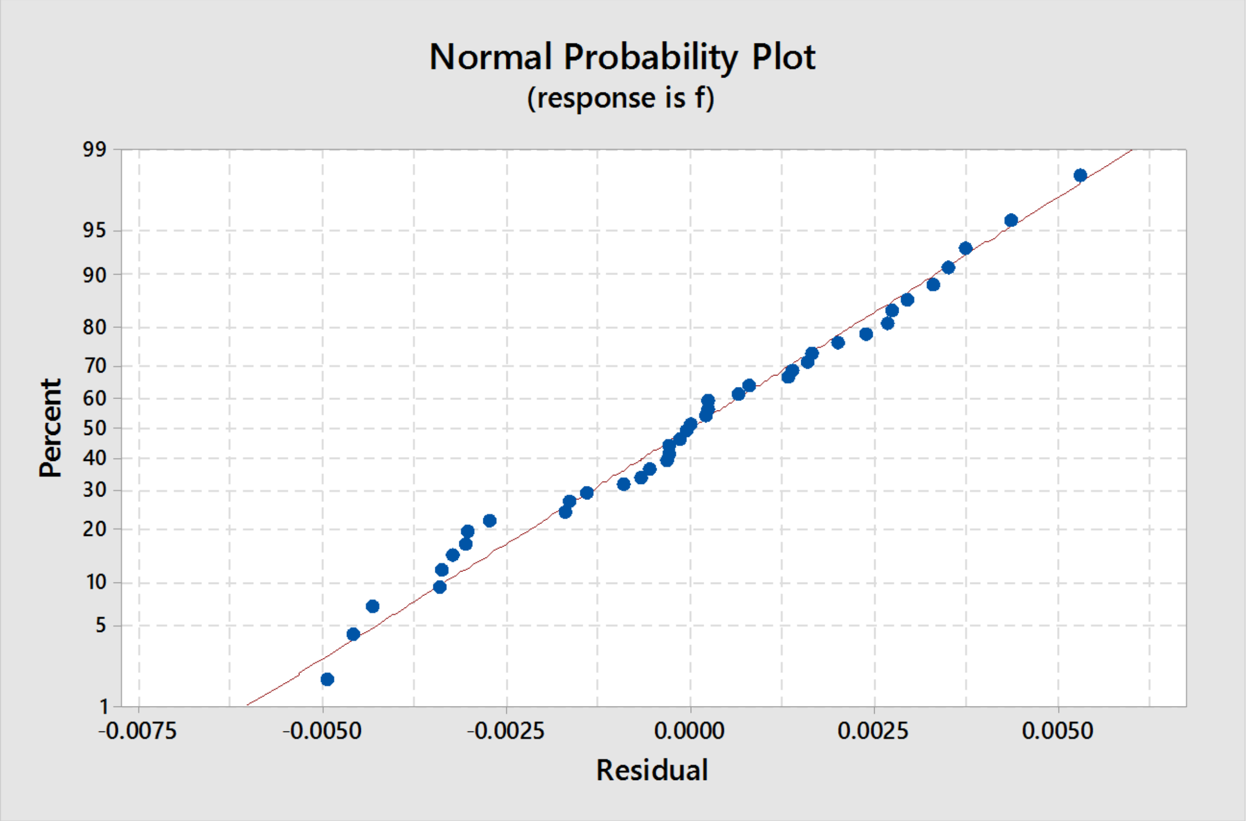

Fig. 5.21 Normal Probability Plot for friction factor

Fig.5.21 shows the plot of simulated values and the values predicted using Eq. 5.2. It can be seen that all 40 data points lie within the deviation line ±10%. This graph implies that 10-90% values of friction factor comes under residual -5 to 5. Residual means the error between simulated value and obtained value through Eq. 5.2. Fig. 5.22 and fig. 5.23 show the comparison between correlation results and Dittus Boetler Equation and Modified Blasius Equation respectively. It is found that correlation results of Nusselt number and friction factor show the variation of 4.48% and 15.62% respectively as compare to simulated results

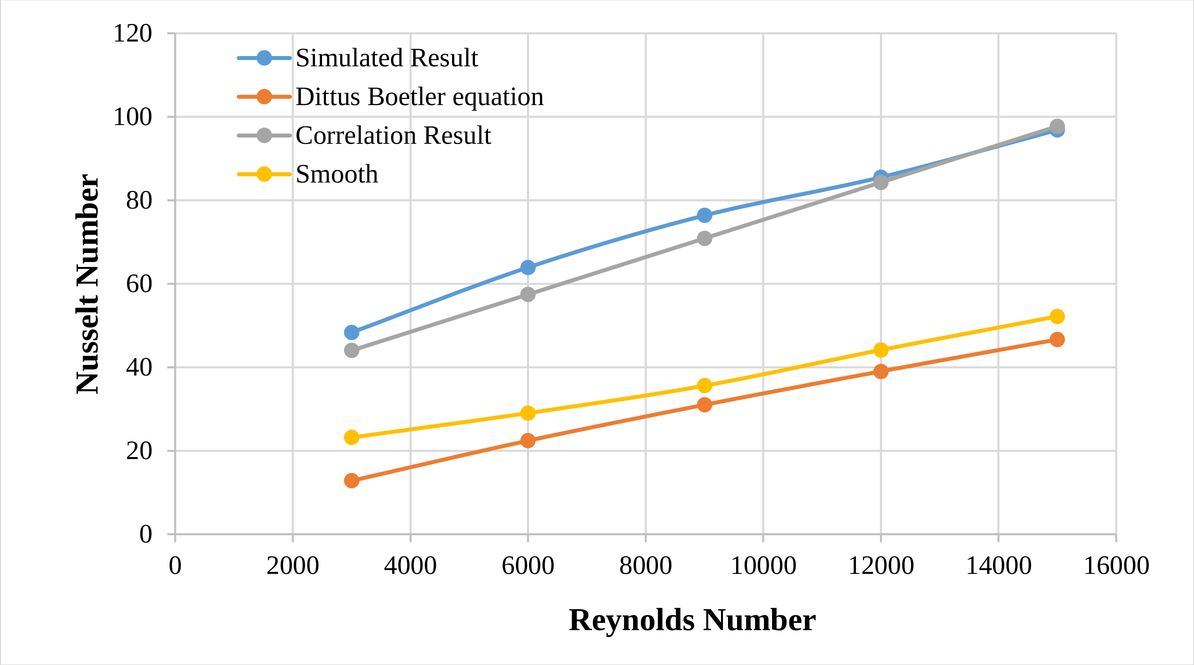

Fig. 5.22 Comparison between correlation result and Dittus Boetler Equation

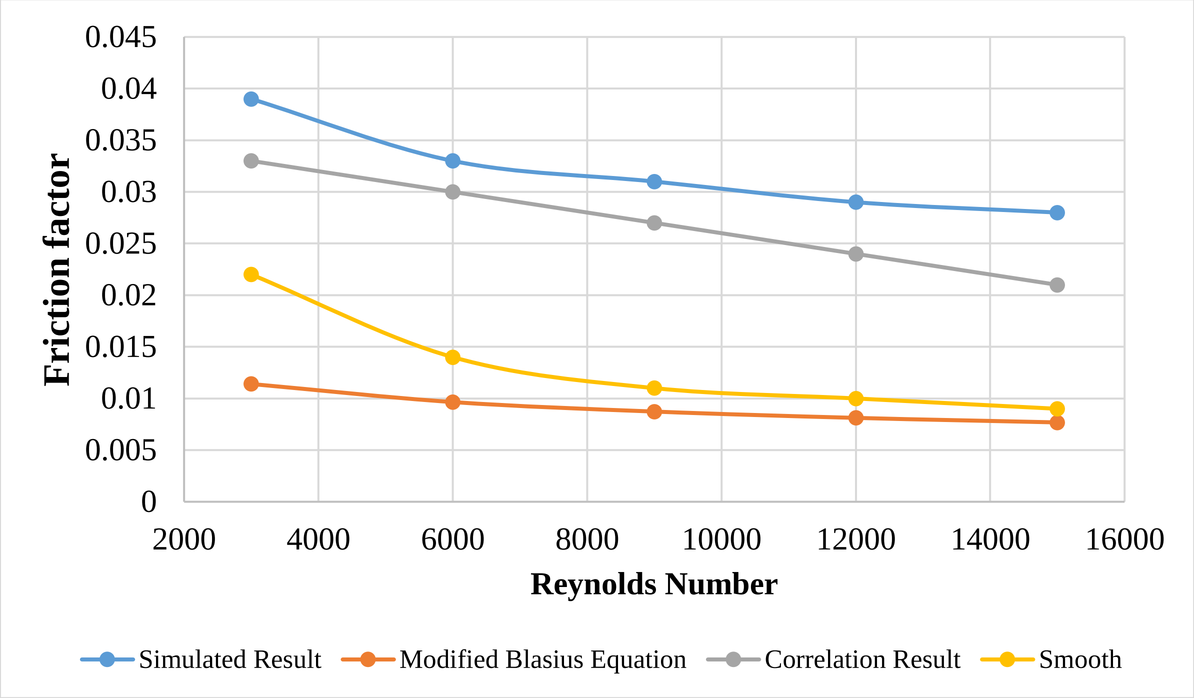

Fig. 5.23 Comparison between correlation result and Modified Blasius Equation

5.7 Thermo-Hydraulic Performance Parameter

A parameter that facilitates the simultaneous consideration of thermal and hydraulic performance is given by as **$(Nu/Nu_s)/(f/f_s)^{1/3}$.** Fig. 5.17 shows the variation of thermo-hydraulic performance parameter with relative roughness height.

Table 5.5 Different cases considered for Thermo-Hydraulic Performance Parameter

Plate	**α(˚)**	**e/D**	**p/e**
P1	30	0.0338	10
P2	45	0.0338	10
P3	60	0.0338	10
P4	75	0.0338	10
P5	60	0.0281	10
P6	60	0.0258	10
P7	60	0.0225	10
P8	60	0.0168	10

It can be concluded from the observations that as the roughness height increases, Nusselt number and friction factor both increases. But the greater proportionate increase in Nusselt number leads to the increase in thermo-hydraulic performance parameter up to relative roughness height of 0.0338 after which the friction losses overcomes the heat transfer enhancement resulting in a slight decrement of thermo-hydraulic performance parameter.

It can be further concluded that as relative roughness height increases, roughness geometry protrude more into flow, acting as a fin, causing more turbulence and results in higher value of friction factor and Nusselt number. Therefore, the proportionate increase in heat transfer enhancement is less than the proportionate increase in friction factor as the relative roughness height is increased at all values of Reynolds number. Therefore, it is desirable to choose the relative roughness height such that the heat transfer is maximized while keeping the pumping losses at the least possible value. It is also found that at lower velocity 60˚ angled rib gives optimum result but at higher velocity (Re>6000) 30˚ angled rib gives optimum result.

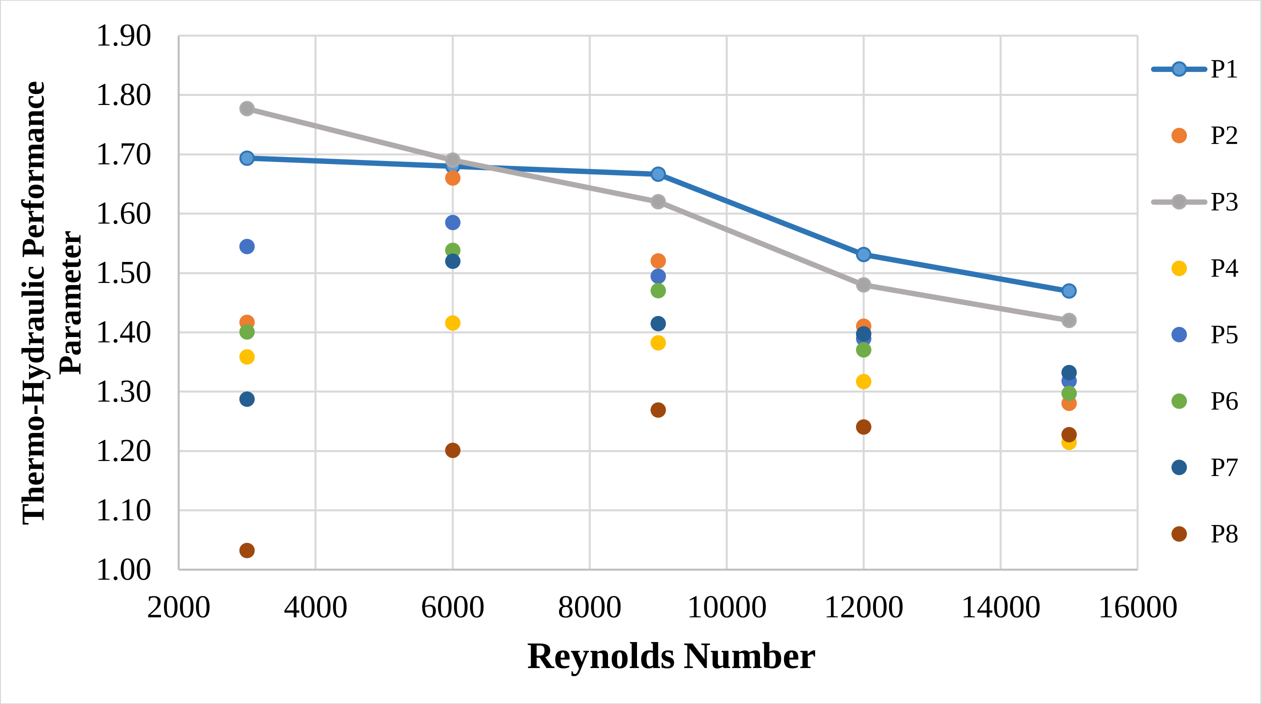

Fig. 5.24 Thermo-Hydraulic Performance Parameter Vs Relative Roughness Height

Chapter 6

Conclusion

In the present study, a rigorous simulation run has been carried out to investigate performance of SAH with artificial roughness. The geometric 3-dimensional modelling and meshing of forty different cases of roughened plates having discrete W-shaped ribs below absorber plate, roughened plates having configuration like angle of attack 30°, 45°, 60° and 75°, relative roughness height 0.0168, 0.0225, 0.0258, 0.0281 and 0.0338, has been performed using ANSYS 15.0.7 and detailed computational fluid dynamic (CFD) analysis has been carried out using FLUENT for all the forty cases for flow Reynolds number ranging from 3000 to 18000 while duct aspect ratio 8 and relative roughness pitch 10 remains constant. For this purpose a 3-D, steady-state model for air flow through the rectangular duct of SAH system has been developed by employing the Realizable k-ε turbulence model and analyzed.

In CFD simulation study the effect of discretization of the ribs on the friction factor and heat transfer coefficient of SAH system has been investigated for flow Reynolds number ranging from 3000 to 15000. Different types of roughnesses (chamfered shaped ribs, inclined ribs, inclined ribs with gap position, W-shaped ribs, discrete W-shaped ribs) are compared for the standard duct for flow Reynolds number ranging from 3000 to 15000. In order to optimize roughness and flow parameters to achieve maximum enhancement in heat transfer with minimum friction power penalty, thermo-hydraulic performance parameter based on constant pumping power is also investigated.

Based on the present study using discrete W-shaped artificial roughness on one broad wall of solar air collector the following conclusions have been drawn.

[1]. Nusselt number increases with an increase of Reynolds number. The maximum enhancement of Nusselt number was found to be 1.89, 1.82, 2.085 and 1.82 times that for smooth duct for angles of attack of 30˚, 45˚, 60˚ and 75˚ respectively for relative roughness height of 0.0338.

[2]. Friction factor decreases with an increase of Reynolds number. For relative roughness height of 0.0338, the maximum enhancement in friction factor was found to be 1.25, 1.24, 1.625 and 1.458 times that of smooth duct for angles of attack of 30˚, 45˚, 60˚ and 75˚ respectively.

The values of Nusselt number and friction factor are substantially higher as compared to those obtained for smooth absorber plates. This is due to distinct change in the friction characteristics as a result of roughness that causes flow separations, reattachments and the generation of secondary flows.

[3]. The effect of discretization was investigated which showed 1.31 times increment in Nusselt Number corresponding to parameters $\alpha=60°$, $e/D_h=0.0338$, $p/e=10$ and $W/H=8$ for discrete W-shaped ribs as compared to continuous W-shaped ribs, because of increase in the number of heat transfer regions.

[4]. Different types of artificial roughnesses (Chamfered type, inclined ribs, inclined rib with gap position, continuous W-shaped ribs, discrete W-shaped ribs) are compared for the standard duct in which discrete W-shaped ribs gives the best result.

[5]. Thermo-hydraulic performance parameter has been adopted for the optimization of roughness and flow parameters to achieve maximum enhancement in heat transfer with minimum friction power penalty. Thermo-hydraulic performance parameter is optimum at 60˚ angled rib for lower velocity but at higher velocity (Re>6000) 30˚ angled rib gives optimum value of thermo-hydraulic performance.

[6]. The comparison of simulated values of Nusselt number and friction factor and those predicted by the correlation shows that all 40 data points lie within the deviation range of ±10%. It can therefore be concluded that the correlations are reasonably satisfactory for the prediction of Nusselt number and friction factor for the roughened duct.

In the present study finally it is concluded that use of artificial roughness in solar air heater duct improves heat transfer is, in general, accompanied with friction power penalty due to a corresponding increase in the friction factor. Therefore, roughness and flow parameters must be optimized to achieve maximum enhancement in heat transfer with minimum friction power penalty.

6.1 Scope for Future Work

Based on the present research scope for future work is indicated below:

- Experimental setup can be fabricated for this analysis and results may be compared with CFD simulated results.
- Same study should be done with radiation model and compare with present study.
- Actual solar condition and varying solar intensity simulation may be used for detailed studies of the SAH system for winter as well as summer seasons.
- For the SAH system having arced shaped rib or dimpled shaped as artificial roughness effect of relative roughness pitch on performance may be analyzed.
- Energy and exergy analysis can be done for roughened SAH system.

References

[1] Karwa Rajendra, Chitoshiya Girish, 2013 “Performance study of solar air heater having v-down discrete ribs on absorber plate” Energy. Xxx, 1-17.

[2] Hans V.S., Saini R.P., Saini J.S., 2010 “Heat transfer and friction factor correlations for a solar air heater duct roughened artificially with multiple v-ribs”, Solar Energy. 84 ,898–911.

[3]Patnaik Amar, Varun, Saini R.P., Singal S.K., Siddhartha, 2009 “Performance prediction of solar air heater having roughened duct provided with transverse and inclined ribs as artificial roughness, Renewable Energy. 34, 2914–2922 .

[4] Bopche S.B., Tandale M.S., 2009 “Experimental investigations on heat transfer and frictional characteristics of a turbulator roughened solar air heater duct”, International Journal of Heat and Mass Transfer. 52 , 2834–2848.

[5]. Aharwal K.R., Gandhi Bhupendra K., Saini J.S., 2009. “Heat transfer and friction characteristics of solar air heater ducts having integral inclined discrete ribs on absorber plate”. International Journal of Heat and Mass Transfer. 52, 5970-5977.

[6]. Saini R.P., Verma Jitendra, 2008. “Heat transfer and friction factor correlations for a duct having dimple-shape artificial roughness for solar air heaters”.Energy. 33, 1277-1287.

[7]Aharwal K.R., Gandhi B.K., Saini J.S.2008 “Experimental investigation on heat-transfer enhancement due to a gap in an inclined continuous rib arrangement in a rectangular duct of solar air heater” Renewable Energy 33. 585–596.

[8]. Sahu M.M.,Bhagoria J.L.,2005. “Augmentation of heat transfer coefficient by using 90˚ broken tranverse ribs on absorber plate of solar air heater”.Renewable Energy. 30, 2057-2073.

[9]. Layek Apurba, Saini J.S., Solanki S.C., 2009. “Effect of chamfering on heat transfer and friction characteristics of solar air heater having absorber plate roughened with compound turbulators” Renewable energy.32, 1292-1298.

[10]. Kumar Arvind, Bhagoria J.L., Sarviya R.M., 2009. “Heat transfer and friction correlations for artificially roughened solar air heater duct with discrete W-shaped ribs”. Energy Conversion and Management. 50, 2106-2117

[11] Yadav A.K., Bhagoria J.L. 2014 “A numerical investigation of square sectioned transverse rib roughened solar air heater” International Journal of Thermal Sciences 79, 111-131

[12] Kumar Anil, 2014 “Analysis of heat transfer and fluid flow in different shaped roughness elements on the absorber plate solar air heater duct” Energy Procedia 57, 2102 – 2111

[13].Boulemtafes-Boukadoum A.,Benzaoui A.,2014. “CFD Based analysis of heat transfer enhancement in solar air heater provided with transverse rectangular ribs”. Energy Procedia. 50, 761-772.

[14]. R.T. Karupaaraj, Y.R. Sekhar, G. Edison, B.S. Praneeth, T. Elango,2014 “heat transfer and fluid flow analysis of flat surface with artificially roughened square transverse wire rib for application in solar air heater” ARPN Journal of Engineering and Applied Sciences. ISSN 1819-6608 Vol. 9

[15]. Mathur Anuj, Agarwal G.D., 2015.”Thermal performance investigation and optimization of fin type solar air heater-a CFD approach”. Progress in computational fluid dynamics, Vol. X, No Y,200x

[16] Chaube Alok, Sahoo P.K., Solanki S.C., 2009. “Analysis of heat transfer augmentation and flow characteristics due to rib roughness over absorber plate of a solar air heater” Renewable Energy 31, 317–331

[17] Ong K.S. 1995 “Thermal Performance of Solar Air Heaters: Mathematical Model and Solution Procedure.” Solar Energy 55, 93–109

[18] Garg H P. 1984 “Some Studies on the Flow Passage Dimension for Solar Air Heating Collectors.” Energy Convers 24 , 181–84

[19] Saxena, Abhishek, and Goel Varun. 2013 “Solar Air Heaters with Thermal Heat Storages” Chinese Journal of Engineering.

[20] Singh K.D.P., Sharma S.P. 2009 “Analytical Investigations on Thermal Performance of Artificially Roughened Double Flow Solar Air Heater.” ARISER Vol. 5, 1-7

[21]. Varun, Saini R.P., Singal S.K., 2007.”A review on roughness geometry used in solar air heater”. Solar energy.81, 1340-1350.

[22]. El-Sebaii A.A., Al-Snani H. “Effect of selective coating on thermal performance of flat plate solar air heaters”. Energy. 35, 1820-1828.

[23].Tyagi V.V., Panwar N.L., Rahim N.A. , Kothari Richa,2012. “Review on solar heating system with and without thermal energy storage system”. Renewable and Sustainable Energy Reviews”. 16, 2289-2303.

[24].Ozgen Filiz, Esen Mehmet, Esen Hikmet, 2009.”Experimental investigation of thermal performance of a double-flow solar air heater having aluminium cans”. Renewable Energy. 34, 2391-2398.

[25] Momin Abdul-Malik Ebrahim, Saini J.S., Solanki S.C., 2002. “Heat transfer and friction in solar air heater duct with V-shaped rib roughness on absorber plate” International Journal of Heat and Mass Transfer. 45, 3383–3396

[26] Akpinar Ebru Kavak, Kocyigit Fatih, 2010 “Experimental investigation of thermal performance of solar air heater having different obstacles on absorber plates” International Communications in Heat and Mass Transfer. 37, 416-421.

[27] Pawar S. S., Hindolia D.A., Bhagoria J.L. 2013 “Experimental study of Nusselt number and Friction factor in solar air heater duct with Diamond shaped rib roughness on absorber plate” American Journal of Engineering Research. ISSN: 2320-0936, Volume-02, 60-68

[28] http://en.wikipedia.org/wiki/Solar_air_heat

[29] http://www.irena.org

Publicatons

1. Mitesh Varshney and G.D. Agrawal. "Techniques for performance enhancement of Solar Air Heater: A Review" International Journal of Science Technology & Engineering. Vol. 3, Issue 04, October 2016.
2. Mitesh Varshney and G.D. Agrawal. "CFD Simulation and Analysis of Chamfered Ribs Roughened Solar Air Heater" National Conference on Renewable Energy Sources & Sustainable Development, RESSD-2016, October 7-8, India

APPENDIX A.1

Turbulence Models

The equations of motion are averaged with respect to time and these turbulent transport models predict the effect of turbulence on the time averaged mean motion. Since all of the terms currently in the equations of motion are instantaneous values, they are replaced with the sum of a time-mean quantity and a fluctuating quantity, with $T =$ the sum of a time-mean quantity and a fluctuating quantity. A new set of equations of motion with the same form are obtained with the addition of these quantities.

Energy

$$\frac{\partial}{\partial t}(\rho c_p \overline{T}) + \frac{\partial}{\partial x}(\rho \overline{u} c_p \overline{T}) + \frac{\partial}{\partial y}(\rho \overline{v} c_p \overline{T}) + \frac{\partial}{\partial z}(\rho \overline{w} c_p \overline{T})$$

$$= K\left(\frac{\partial^2 \overline{T}}{\partial x^2} + \frac{\partial^2 \overline{T}}{\partial y^2} + \frac{\partial^2 \overline{T}}{\partial z^2}\right) - \frac{\partial}{\partial x_i}\left(\rho c_p \overline{T' u_i'}\right) + q''' \qquad (1.1)$$

Momentum in x-direction

$$\frac{\partial}{\partial t}(\rho\overline{u}) + \frac{\partial}{\partial x}(\rho\overline{u}\,\overline{u}) + \frac{\partial}{\partial y}(\rho\overline{v}\,\overline{u}) + \frac{\partial}{\partial z}(\rho\overline{w}\,\overline{u}) = -\frac{\partial\overline{P}}{\partial x} + \mu\left(\frac{\partial^2\overline{u}}{\partial x^2} + \frac{\partial^2\overline{u}}{\partial y^2} + \frac{\partial^2\overline{u}}{\partial z^2}\right) - \frac{\partial}{\partial x_i}\left(\rho\overline{u' u_i'}\right) \qquad (1.2)$$

Momentum in y-direction

$$\frac{\partial}{\partial t}(\rho\overline{v}) + \frac{\partial}{\partial x}(\rho\overline{u\,v}) + \frac{\partial}{\partial y}(\rho\overline{v\,v}) + \frac{\partial}{\partial z}(\rho\overline{w}\,\overline{v}) \qquad (1.3)$$

$$= -\frac{\partial\overline{P}}{\partial y} + \mu\left(\frac{\partial^2\overline{v}}{\partial x^2} + \frac{\partial^2\overline{v}}{\partial y^2} + \frac{\partial^2\overline{v}}{\partial z^2}\right) - \frac{\partial}{\partial x_i}\left(\rho\overline{v' u_i'}\right) - \rho g\beta\left(\overline{T}_\infty - \overline{T}\right)$$

Momentum in z-direction

$$\frac{\partial}{\partial t}(\rho\overline{w}) + \frac{\partial}{\partial x}(\rho\overline{u}\,\overline{w}) + \frac{\partial}{\partial y}(\rho\overline{v}\,\overline{w}) + \frac{\partial}{\partial z}(\rho\overline{w}\,\overline{w}) = -\frac{\partial\overline{P}}{\partial z} + \mu\left(\frac{\partial^2\overline{w}}{\partial x^2} + \frac{\partial^2\overline{w}}{\partial y^2} + \frac{\partial^2\overline{w}}{\partial z^2}\right) - \frac{\partial}{\partial x_i}\left(\rho\overline{w' u_i'}\right) \qquad (1.4)$$

Continuity

$$\frac{\partial}{\partial x}(\rho u)+\frac{\partial}{\partial y}(\rho v)+\frac{\partial}{\partial z}(\rho w)=0 \tag{1.5}$$

The momentum equations have the term $-\partial/\partial x_i\left(\rho\overline{u'_j u'_i}\right)$ given in compact tensor notation. These terms represent the effect that turbulent motion has on the time-mean quantities known as Reynold's stresses which are high frequency fluctuating velocity components. The new terms in the energy equation $(-\partial/\partial x_i\left(\rho c_p\overline{T'u'_i}\right))$ represent the turbulent heat fluxes which are the fluctuating components of the temperature and velocity.

The eddy-viscosity concept proposed by Boussinesq can then be applied to the motion equations. The additional turbulent stresses are assumed to be proportional to the mean-velocity gradients. The stresses in tensor notation can be related as follows.

$$\overline{u'_j u'_i}=\frac{\mu_t}{\rho}\left(\frac{\partial\overline{u}_j}{\partial x_i}+\frac{\partial\overline{u}_i}{\partial x_j}\right)-\frac{2}{3}k\delta_{ji} \tag{1.6}$$

where μ_t is the eddy viscosity, k is the kinetic energy and δ_{ji} is the Kronecker delta. This approach is used in both the k-epsilon and k-omega models. The advantage being that computational costs are relatively low because of the computational power needed to calculate the turbulent viscosity. Also, the turbulent heat fluxes are assumed to be proportional to the mean temperature gradients and are again expressed in tensor notation.

$$-\rho c_p\overline{T'u'_i}=c_p\Gamma\frac{\partial\overline{T}}{\partial x_j} \tag{1.7}$$

where Γ is the turbulent diffusivity of heat. Both the eddy viscosity and the turbulent diffusivity of heat are properties of the flow, not the fluid. In order to relate these two quantities together, the turbulent Prandtl number is introduced. It can be assumed constant as experiments have shown that this ratio does not vary in flows or between flows even though μ_t and Γ do.

$$\sigma_t = \frac{\mu_t}{\Gamma} \tag{1.8}$$

By substituting equations 1.6, 1.7 and 1.8 into the equations of motion (equations 1.1 to 1.5) the fluctuating quantities are removed as eddy viscosity and mean quantity gradients describe the turbulent diffusion and the equations of motion are represented as follows.

Energy

$$\frac{\partial}{\partial t}(\rho c_p \overline{T}) + \frac{\partial}{\partial x}(\rho \overline{u} c_p \overline{T}) + \frac{\partial}{\partial y}(\rho \overline{v} c_p \overline{T}) + \frac{\partial}{\partial z}(\rho \overline{w} c_p \overline{T}) \tag{1.9}$$

$$= K\left(\frac{\partial^2 \overline{T}}{\partial x^2} + \frac{\partial^2 \overline{T}}{\partial y^2} + \frac{\partial^2 \overline{T}}{\partial z^2}\right) + \frac{\partial}{\partial x_i}\left(\frac{\partial \overline{T}}{\partial x_i}\frac{c_p \mu_t}{\sigma_t}\right) + q'''$$

Momentum in x-direction

$$\frac{\partial}{\partial t}(\rho \overline{u}) + \frac{\partial}{\partial x}(\rho \overline{u}\overline{u}) + \frac{\partial}{\partial y}(\rho \overline{v}\overline{u}) + \frac{\partial}{\partial z}(\rho \overline{w}\overline{u}) = -\frac{\partial \overline{P}}{\partial x} + (\mu + \mu_t)\left(\frac{\partial^2 \overline{u}}{\partial x^2} + \frac{\partial^2 \overline{u}}{\partial y^2} + \frac{\partial^2 \overline{u}}{\partial z^2}\right) \tag{1.10}$$

Momentum in y-direction

$$\frac{\partial}{\partial t}(\rho \overline{v}) + \frac{\partial}{\partial x}(\rho \overline{u}\overline{v}) + \frac{\partial}{\partial y}(\rho \overline{v}\overline{v}) + \frac{\partial}{\partial z}(\rho \overline{w}\overline{v}) \tag{1.11}$$

$$= -\frac{\partial \overline{P}}{\partial y} + (\mu + \mu_t)\left(\frac{\partial^2 \overline{v}}{\partial x^2} + \frac{\partial^2 \overline{v}}{\partial y^2} + \frac{\partial^2 \overline{v}}{\partial z^2}\right) - \rho g \beta\left(\overline{T}_\infty - \overline{T}\right)$$

Momentum in z-direction

$$\frac{\partial}{\partial t}(\rho\overline{w})+\frac{\partial}{\partial x}(\rho\overline{u}\overline{w})+\frac{\partial}{\partial y}(\rho\overline{v}\overline{w})+\frac{\partial}{\partial z}(\rho\overline{w}\overline{w})=-\frac{\partial\overline{P}}{\partial z}+(\mu+\mu_t)\left(\frac{\partial^2\overline{w}}{\partial x^2}+\frac{\partial^2\overline{w}}{\partial y^2}+\frac{\partial^2\overline{w}}{\partial z^2}\right) \quad (1.12)$$

Continuity

$$\frac{\partial}{\partial x}(\rho\overline{u})+\frac{\partial}{\partial y}(\rho\overline{v})+\frac{\partial}{\partial z}(\rho\overline{w})=0 \quad (1.13)$$

This form of the equations differs from the original instantaneous equations due only to the momentum and heat diffusion coefficients. The new terms in the momentum and energy equations represent the influence of turbulence on the time-mean quantities. The following sections describe the turbulence models that will be tested in order to determine which model gives the best results for large atrium flow, specifically the case described at the beginning of this section.

A.1.1 k-ε Turbulence Model

The k-ε model has become one of the most widely used turbulence models as it provides robustness, economy and reasonable accuracy for a wide range of turbulent flows [Malalasekera]. Improvements have been made to the standard model which improves its performance and two variants are available in Fluent; the RNG (renormalization group) model and the realizable model. The standard, RNG, and realizable models have similar form with transport equations for k and ε. The two transport equations independently solve for the turbulent velocity and length scales. The main differences between the three models are as follows;

- The turbulent Prandtl Numbers governing the turbulent diffusion of *k* and ε
- The generation and destruction terms in the equation for ε
- The method of calculating turbulent viscosity

A.1.1.1 Standard k-Epsilon Turbulence Model

Fluent User's manual [ ] reveals that this model was initially proposed by Launder and Spalding (1972). As mentioned in Fluent User's manual [ ], for this model the transport equation for *k* is derived from the exact equation, but the transport for ε was obtained using physical reasoning and is, therefore, similar to the mathematically derived transport equation of *k*, but is not exact. The turbulent kinetic energy *k*, and its rate of dissipation ε, for this model are obtained by the following equations.

$$\frac{\partial}{\partial t}(\rho k)+\frac{\partial}{\partial x_i}(\rho k u_i)=\frac{\partial}{\partial x_j}\left[\left(\mu+\frac{\mu_t}{\sigma_k}\right)\frac{\partial k}{\partial x_j}\right]+G_k+G_b-\rho\varepsilon-Y_M+S_K \qquad (1.14)$$

$$\frac{\partial}{\partial t}(\rho\varepsilon)+\frac{\partial}{\partial x_i}(\rho\varepsilon u_i)=\frac{\partial}{\partial x_j}\left[\left(\mu+\frac{\mu_t}{\sigma_\varepsilon}\right)\frac{\partial \varepsilon}{\partial x_j}\right]+C_{1\varepsilon}\frac{\varepsilon}{k}\left(G_k+C_{3\varepsilon}G_b\right)-C_{2\varepsilon}\rho\frac{\varepsilon^2}{k}+S_\varepsilon \qquad (1.15)$$

where G_k represents the generation of turbulent kinetic energy that arises due to mean velocity gradients, G_b is the generation of turbulent kinetic energy that arises due to buoyancy, and Y_M represents the fluctuating dilation in compressible turbulence that contributes to the overall dissipation rate. S_ε and S_k are source terms defined by the user. $C_{1\varepsilon}$, $C_{2\varepsilon}$ and C_μ are constants that have been determined experimentally and are taken to have the following values;

$$C_{1\varepsilon}=1.44,\ C_{2\varepsilon}=1.92 \text{ and } C_\mu=0.09$$

σ_k and σ_s are turbulent Prandtl numbers for the turbulent kinetic energy and its dissipation rate. These have also been derived experimentally and are defined as follows.

$$\sigma_k=1.0,\ \ \sigma_s=1.3$$

The turbulent (or eddy) viscosity at each point is related to the local values of turbulent kinetic energy and its dissipation rate by;

$$\mu_t = \rho C_\mu \frac{k^2}{\varepsilon} \tag{1.16}$$

where C_μ is constant and defined above. The term for the production of turbulent kinetic energy G_k is common in many of the turbulence models studied and is defined as

$$G_k = -\rho \overline{u_i' u_j'} \frac{\partial u_j}{\partial x_i} \tag{1.17}$$

The modulus of mean rate-of-strain tensor, S is defined as

$$S = \sqrt{2 S_{ij} S_{ij}} \tag{1.18}$$

The generation of turbulent kinetic energy that arises due to buoyancy, G_b is defined as follows

$$G_b = \beta g_i \frac{\mu_t}{\mathrm{Pr}_t} \frac{\partial T}{\partial x_i} \tag{1.19}$$

As the present study uses relatively low velocities, the dilation dissipation term, Y_M which accounts for turbulence from compressibility effects is defined as

$$Y_M = 2\rho\varepsilon M_t^2 \tag{1.20}$$

A.1.1.2 RNG k-Epsilon Turbulence Model

Similar to the standard k-epsilon model, the RNG model was derived from the instantaneous Navier Stokes equations, except it uses a technique called renormalization group theory described by Yakhot and Orszag (1986) as mentioned in Fluent User's manual [ ]. This derivation produces a model with different constants to those used in the standard k-epsilon model and also adds new terms to the transport equations for the turbulent kinetic energy and its dissipation. The effect of swirl is also accounted for in the RNG model enhancing the accuracy of swirling flows. An analytical formula for turbulent Prandtl numbers is provided in this model while the standard model relies on user-specific constant values. Finally, assuming appropriate treatment of the near wall region, the RNG model uses an analytically derived differential formula for the effective turbulent viscosity which accounts for low Reynolds number flows. The RNG k-Epsilon model is therefore more accurate and more reliable than the standard k-Epsilon model for a wider range of flows. As a result from these differences, the transport equations appear as follows.

$$\frac{\partial}{\partial t}(\rho k)+\frac{\partial}{\partial x_i}(\rho k u_i)=\frac{\partial}{\partial x_j}\left[\alpha_k \mu_{eff}\frac{\partial k}{\partial x_j}\right]+G_k+G_b-\rho\varepsilon-Y_M+S_K \tag{1.21}$$

where G_k represents the generation of turbulent kinetic energy that arises due to mean velocity gradients, G_b is generation of turbulent kinetic energy that arises due to buoyancy, and Y_M represents the fluctuating dilation in compressible turbulence that contributes to the overall dissipation rate. S_ε and S_k are source terms defined by the user. α_k and α_ε are inverse effective Prandtl numbers for the turbulent kinetic energy and its dissipation. The RNG theory uses a scale elimination procedure that defines the effective viscosity given in the following equation.

$$d\left(\frac{\rho^2 k}{\sqrt{\varepsilon\mu}}\right)=1.72\frac{\hat{v}}{\sqrt{\hat{v}^3-1+C_v}}d\hat{v} \tag{1.22}$$

where $\hat{v}=\mu_{eff}/\mu$ and C_v is a constant equal approximately to 100. This equation incorporates the ability to accurately define how the effective turbulent transport varies with effective Reynolds number to obtain more accurate results for low-Re flows and near-wall flows. For high Reynolds numbers, the effective viscosity is defined by the following ratio;

$$\mu_t=\rho C_\mu\frac{k^2}{\varepsilon} \tag{1.23}$$

Although this is similar to the turbulent viscosity of the standard model, the constant C_μ is derived using the RNG theory and found to be 0.0845 which is very close to the value used in the standard model (i.e., 0.09). $C_{1\varepsilon}$ and $C_{2\varepsilon}$ are constants that have been derived analytically by the RNG theory and are defined as follows.

$$C_{1\varepsilon} = 1.42,\ C_{2\varepsilon} = 1.68$$

A.1.1.3 Realizable k-Epsilon Turbulence Model

The Realizable model by Shih (1995) is the most recently developed of the three k-Epsilon variations and features two main differences from the standard k-Epsilon model. Fluent User's manual [ ] reveals that this model uses a new equation for the turbulent viscosity and the dissipation rate transport equation has been derived from the equation for the transport of the mean-square vorticity fluctuation. The form of the eddy viscosity (turbulent) equations is based on the realizability constraints; the positivity of normal Reynolds stresses and Schwarz' inequality for turbulent shear stresses (i.e., certain mathematical constraints on the normal stresses are satisfied). This is not satisfied by either the standard or the RNG k-epsilon models which makes the realizable model more precise than both models at predicting flows such as separated flows and flows with complex secondary flow features.

The term "realizable" means that the model satisfies certain mathematical constraints on the Reynolds stresses, consistent with the physics of turbulent flows. Neither the standard k-ε model nor the RNG k-ε model is realizable.

An immediate benefit of the realizable k-ε model is that it more accurately predicts the spreading rate of both planar and round jets. It is also likely to provide superior performance for flows involving rotation, boundary layers under strong adverse pressure gradients, separation and recirculation.

In terms of the improved changes by Shih (1995), the transport equations become:

$$\frac{\partial}{\partial t}(\rho k) + \frac{\partial}{\partial x_j}(\rho k u_j) = \frac{\partial}{\partial x_j}\left[\left(\mu + \frac{\mu_t}{\sigma_k}\right)\frac{\partial k}{\partial x_j}\right] + G_k + G_b - \rho\varepsilon - Y_M + S_K \qquad (1.24)$$

$$\frac{\partial}{\partial t}(\rho\varepsilon)+\frac{\partial}{\partial x_j}(\rho\varepsilon u_j) \tag{1.25}$$

$$=\frac{\partial}{\partial x_j}\left[\left(\mu+\frac{\mu_t}{\sigma_\varepsilon}\right)\frac{\partial\varepsilon}{\partial x_j}\right]+\rho C_1 S\varepsilon-\rho C_2\frac{\varepsilon^2}{k+\sqrt{\nu\varepsilon}}+C_{1\varepsilon}\frac{\varepsilon}{k}C_{3\varepsilon}G_b+S_\varepsilon$$

where G_k represents the generation of turbulent kinetic energy that arises due to mean velocity gradients, G_b is generation of turbulent kinetic energy that arises due to buoyancy, and Y_M represents the fluctuating dilation in compressible turbulence that contributes to the overall dissipation rate. S_ε and S_k are source terms defined by the user. α_k a and α_ε are the turbulent Prandtl numbers for the turbulent kinetic energy and its dissipation.

$$\mu_t=\rho C_\mu\frac{k^2}{\varepsilon} \tag{1.26}$$

where C_μ is computed from

$$C_\mu=\frac{1}{A_0+A_S\dfrac{kU^*}{\varepsilon}} \tag{1.27}$$

where

$$U^*=\sqrt{S_{ij}S_{ij}+\tilde{\Omega}_{ij}\tilde{\Omega}_{ij}} \qquad \text{and} \qquad \tilde{\Omega}_{ij}=\overline{\Omega_{ij}}-\varepsilon_{ijk}\omega_k-2\varepsilon_{ijk}\omega_k$$

In the above equation, $\overline{\Omega_{ij}}$ is the mean rate of rotation tensor viewed in a rotating reference frame with angular velocity ω_k. The constants A_0 and A_S are defined as;

$$A_0=4.04,\quad A_S=\sqrt{6}\cos\phi$$

where

$$\phi=\frac{1}{3}\cos^{-1}\left(\sqrt{6}\frac{S_{ij}S_{jk}S_{ki}}{\tilde{S}^3}\right),\quad \tilde{S}=\sqrt{S_{ij}S_{ij}},\quad S_{ij}=\frac{1}{2}\left(\frac{\partial u_j}{\partial x_i}+\frac{\partial u_i}{\partial x_j}\right)$$

It has been shown that C_μ is a function of the mean strain and rotational rates, the angular velocity of the rotating system, and the turbulent kinetic energy and its dissipation rate. The standard value of $C_\mu = 0.09$ is found to be the solution of equation 1.27 for an inertial sub layer in the equilibrium boundary layer. The constants $C_{1\varepsilon}$, C_2, σ_k and σ_ε have been determined by Shih (1995) and are defined as follows.

$$C_{1\varepsilon} = 1.44,\ C_2 = 1.9,\ \sigma_k = 1.0,\ \sigma_\varepsilon = 1.2$$

APPENDIX A.2

Nusselt number and friction factor values

Table A.2.1 Nusselt number values for different turbulence models

Reynolds Number	Dittus Boetler equation	Realizable K-epsilon	RNG K-epsilon	SST K-omega	Standard K-epsilon	Standard K-omega
3000	12.8	12.54	12.6	14.4	12.67	14.7
6000	22.4	20.65	20.56	24.12	20.85	24.136
9000	30.99	27.83	27.82	32.167	28.125	32.43
12000	39.01	34.45	34.43	41.828	34.79	41.82
15000	46.64	40.67	41.13	48.19	41.18	48.14

Table A.2.2 Variation of Nusselt number with angle of attack

Angle of attack	Re=3000	Re=6000	Re=9000	Re=12000	Re=15000
α=30°	42.24	60.49	72.23	82.04	94.59
α=45°	38.94	57.27	70.06	80.09	92.48
α=60°	48.32	63.91	76.36	85.51	96.83
α=75°	35.65	53.96	68.48	79.58	92.17

Table A.2.3 Variation of friction factor with angle of attack

Angle of attack	Re=3000	Re=6000	Re=9000	Re=12000	Re=15000
α=30°	0.03	0.023	0.02	0.018	0.017
α=45°	0.029	0.023	0.02	0.018	0.017
α=60°	0.039	0.033	0.031	0.029	0.028
α=75°	0.035	0.032	0.03	0.029	0.028

Table A.2.4 Variation of Nusselt number with relative roughness height

Relative roughness height(e/D)	Re=3000	Re=6000	Re=9000	Re=12000	Re=15000
0.0168	24.24	38.54	52.12	63.91	75.81
0.0225	31.38	52.68	64.20	80	91.93
0.0258	36.05	55.43	68.59	80.74	92.26
0.0281	40.14	58.5	70.62	82.96	95.08
0.0338	48.32	63.91	76.36	85.51	96.83
0.0371	49.32	64.86	77.83	90.75	103.14
0.0405	51.45	65.6	79.59	92.79	105.80

Table A.2.5 Variation of friction factor with relative roughness height

Relative roughness height(e/D)	Re=3000	Re=6000	Re=9000	Re=12000	Re=15000
e/D=0.0168	0.025	0.019	0.017	0.016	0.015
e/D=0.0225	0.028	0.024	0.023	0.022	0.021
e/D=0.0258	0.033	0.027	0.025	0.024	0.023
e/D=0.0281	0.034	0.029	0.026	0.025	0.024
e/D=0.0338	0.035	0.032	0.03	0.029	0.028
e/D=0.0371	0.042	0.035	0.033	0.032	0.031
e/D=0.0405	0.045	0.038	0.035	0.034	0.033

Table A.2.6 Variation of Nusselt Number with discretization

Types of discretization	3000	6000	9000	12000	15000
Smooth	19.27	27.11	36.36	45.13	53.59
Continuous W-shaped ribs	36.76	51.79	62.78	73.68	87.31

Discrete W-shaped ribs	**48.32**	**63.91**	**76.36**	**83.51**	**96.83**
Multiple discrete W-shaped rib	**51.19**	**66.11**	**80.03**	**91.69**	**104.82**

Table A.2.7 Variation of friction factor with discretization

Types of discretization	**3000**	**6000**	**9000**	**12000**	**15000**
Smooth	**0.018**	**0.013**	**0.011**	**0.01**	**0.009**
Continuous W-shaped ribs	**0.03**	**0.026**	**0.023**	**0.022**	**0.022**
Discrete W-shaped ribs	**0.035**	**0.032**	**0.03**	**0.029**	**0.028**
Multiple discrete W-shaped ribs	**0.046**	**0.039**	**0.036**	**0.032**	**0.031**

Table A.2.8 Variation of Nusselt Number with type of roughness

Types of roughness	**3000**	**6000**	**9000**	**12000**	**15000**
Smooth	**19.27**	**27.11**	**36.36**	**45.13**	**53.59**
Inclined rib	**24.11**	**33.39**	**43.02**	**56.12**	**66.48**
Inclined rib with gap position	**31.56**	**46.88**	**59.03**	**70.88**	**80.94**
W-shaped ribs	**36.76**	**51.79**	**62.78**	**73.68**	**87.31**
Discrete W-shaped	**48.32**	**63.91**	**76.36**	**81.51**	**96.83**
Chamfered shaped rib	**27.59**	**40.78**	**52.1**	**61.24**	**69.04**

Table A.2.9 Variation of friction factor with type of roughness

Types of roughness	**3000**	**6000**	**9000**	**12000**	**15000**
Smooth	**0.018**	**0.013**	**0.011**	**0.01**	**0.009**
Inclined rib	**0.026**	**0.02**	**0.019**	**0.018**	**0.018**
Inclined rib with gap position	**0.03**	**0.023**	**0.021**	**0.02**	**0.02**

W-shaped ribs	**0.03**	**0.026**	**0.023**	**0.022**	**0.022**
Discrete W-shaped	**0.035**	**0.032**	**0.03**	**0.029**	**0.028**
Chamfered shaped rib	**0.032**	**0.026**	**0.022**	**0.019**	**0.018**

APPENDIX A.3 Thermo-hydraulic Performance

Table A.3 Variation of thermo-hydraulic performance parameter for different plates investigated

Plate	**Re-3000**	**Re-6000**	**Re-9000**	**Re-12000**	**Re-15000**
P-1	**1.69**	**1.68**	**1.67**	**1.53**	**1.47**
P-2	**1.42**	**1.66**	**1.52**	**1.41**	**1.28**
P-3	**1.78**	**1.69**	**1.62**	**1.48**	**1.42**
P-4	**1.36**	**1.42**	**1.38**	**1.32**	**1.21**
P-5	**1.54**	**1.59**	**1.49**	**1.39**	**1.32**
P-6	**1.40**	**1.54**	**1.47**	**1.37**	**1.30**
P-7	**1.29**	**1.52**	**1.41**	**1.40**	**1.33**
P-8	**1.03**	**1.20**	**1.27**	**1.24**	**1.23**